UNIVERSITY OF CALIFORNIA

Santa Barbara

High Performance MOCVD Grown QD Laser on GaAs and Si

A dissertation submitted in partial satisfaction of the

requirements for the degree

Doctor of Philosophy

In

Electrical and Computer Engineering

by

Lei Wang

Committee in charge:

Professor Jonathan Klamkin, Chair

Professor Steven Denbaars

Professor Jon Schuller

Professor Larry Coldren

March 2023

The dissertation of Lei Wang is approved.

_____

Professor Steven Denbaars

_____

Professor Jon Schuller

_____

Professor Larry Coldren

_____

Professor Jonathan Klamkin, Committee Chair

March 2023

High Performance MOCVD Grown QD Laser on GaAs and Si

by

Lei Wang

Dedicate to my beloved wife: Ke Fang

ACKNOWLEDGEMENTS

It is with great pleasure that I reflect upon my five years at the beautiful University of California, Santa Barbara. Despite the challenges of pursuing a Ph.D., I am proud of what I have accomplished and the knowledge I have gained. My time here has been nothing short of wonderful, and I will always treasure the memories I have made.

I owe a debt of gratitude to my advisor, Professor Jonathan Klamkin, for his guidance and support throughout my Ph.D. journey no matter in research and life. His insight and expertise were invaluable in shaping my research, and I am deeply grateful for the opportunities he provided me to grow form a student to a mature researcher.

I would also like to extend my thanks to the members of my Ph.D. committee, including Professor Jon Schuller, Professor Steven Denbaars, and Professor Larry Coldren who provided me with constructive feedback and support throughout my studies. Your insights and encouragement helped me stay on track, and I am grateful for the time and effort you invested in my success.

I would be remiss if I did not acknowledge the members of my research group, Thomas, Paul, Michael, Sergio, Fengqiao, Simone, Ludovico, Diya, Bei, Si, Hongwei, Joseph, Fabrizio, etc. Your camaraderie and collaboration enriched my time at UCSB. Thank you for your contributions to my work, and for the many stimulating discussions that we shared.

Finally, I would like to express my deepest appreciation to my wife for her unwavering support and love throughout the last five years. Your presence in my life has been a constant source of strength and joy, and I am so grateful for the sacrifices you made to help me achieve

my goals. I would also like to thank my parents (Chunzhen Wang and Jingfang Xu) and parents-in-law (Chengwu Fang and Yanhua Zhang) for their steadfast support and encouragement throughout my whole life. Your belief in me has meant more than words can express.

To all of the individuals who have supported me along the way, thank you from the bottom of my heart. I could not have done this without you.

Curriculum Vitae

Lei Wang
March 2023

Educations

Ph.D.	University of California, Santa Barbara Electronic & Photonic, 2023 Dissertation: High Performance MOCVD Grown QD Laser on GaAs and Si Advisor: Prof. Jonathan Klamkin
Bachelor	Shandong University Physics, 2014

Publications

[1] M. Nickerson, P. Verrinder, **L. Wang**, B. Song, and J. Klamkin, in *Optica Advanced Photonics Congress 2022* (Optica Publishing Group, Maastricht,Limburg, 2022), p. IW4B.4.

[2] M. Nickerson, B. Song, **L. Wang**, P. Verrinder, J. Brookhyser, G. Erwin, J. Kleinert, and J. Klamkin, in *Conference on Lasers and Electro-Optics* (Optica Publishing Group, San Jose, California, 2022), p. SS1D.4.

[3] **L. Wang**, E. Hughes, C. Zhang, J. Bowers, and J. Klamkin, in *Optica Advanced Photonics Congress 2022* (Optica Publishing Group, Maastricht,Limburg, 2022), p. IW2B.1.

[4] P. Verrinder, **L. Wang**, F. Sang, V. Rosborough, G. Yang, M. Stephen, L. Coldren, and J. Klamkin, in *2022 Optical Fiber Communications Conference and Exhibition (OFC)* (2022), pp. 1–3.

[5] T. Meissner, S. Zhu, S.Š. Brunelli, A. Carter, A. Young, C. Zhang, **L. Wang**, G.G. Meena, R. Moreira, L. Coldren, and J. Klamkin, in *Conference on Lasers and Electro-Optics* (Optica Publishing Group, San Jose, California, 2022), p. ATu5M.6.

[6] J. Klamkin, S. Zhu, B. Shi, **L. Wang**, and B. Song, in *Proc.SPIE* (2022), p. 1202107.

[7] P. Verrinder, **L. Wang**, F. Sang, J. Fridlander, V. Rosborough, M. Nickerson, G. Yang, M. Stephen, L. Coldren, and J. Klamkin, in *2021 27th International Semiconductor Laser Conference (ISLC)* (2021), pp. 1–2.

[8] P.A. Verrinder, **L. Wang**, J. Fridlander, F. Sang, V. Rosborough, M. Nickerson, G. Yang, M. Stephen, L. Coldren, and J. Klamkin, IEEE Journal of Selected Topics in Quantum Electronics **28**, 1 (2022).

[9] B. Shi, H. Zhao, **L. Wang**, S.T.Š. Bruneiii, B. Song, and J. Klamkin, in *2019 Asia Communications and Photonics Conference (ACP)* (2019), pp. 1–3.

[10] **L. Wang**, H. Zhao, B. Shi, S. Pinna, S.S. Brunelli, F. Sang, B. Song, and J. Klamkin, in *Optical Fiber Communication Conference (OFC) 2020* (Optica Publishing Group, San Diego, California, 2020), p. T4H.2.

[11] B. Shi, H. Zhao, **L. Wang**, B. Song, S.T. Suran Brunelli, and J. Klamkin, Optica **6**, 1507 (2019).
[12] **L. Wang**, B. Shi, H. Zhao, S.S. Brunelli, B. Song, D.C. Oakley, and J. Klamkin, in *Conference on Lasers and Electro-Optics* (Optica Publishing Group, San Jose, California, 2019), p. JTu2A.82.
[13] B. Shi, L. Wang, A.A. Taylor, S. Suran Brunelli, H. Zhao, B. Song, and J. Klamkin, Appl Phys Lett **114**, 172102 (2019).
[14] **L. Wang**, B. Shi, H. Zhao, S.S. Brunelli, B. Song, D.C. Oakley, and J. Klamkin, in *Conference on Lasers and Electro-Optics* (Optica Publishing Group, San Jose, California, 2019), p. JTu2A.82.

ABSTRACT

High Performance MOCVD Grown QD Laser on GaAs and Si

by

Lei Wang

The MOCVD growth mechanism of InAs QD was first explored. By optimizing the InAs QD growth parameters, including growth temperature, V/III, growth rate, and capping process, highly uniform QDs have been achieved with a dot density of about 5.5E10cm-2. Room temperature PL characterization on the QDs shows a 50 nm FWHM for the ground state. A high-quality InGaP thick layer under low temperatures was also developed as the cladding layer for the laser structure. High-performance FP cavity QD laser on GaAs substrate was first demonstrated with state-of-the-art performance. The broad-area laser without facet coating shows a single facet power of 200 mW; the short narrow-ridge laser without facet coating shows a high wall-plug efficiency of about 30%. To enable a QD laser on Si, the GoVS template was developed. Combining the technology of aspect ratio trap, thermal cycle annealing, and strain layer superlattice, the GoVS sample has achieved a low threading dislocation density (4E6cm-2) and a surface roughness of 2.7 nm. The full laser structure was grown on the GoVS sample with AlGaAs as the lower cladding layer and low-temperature InGaP as the upper cladding layer. The laser on Si has shown a decent device performance at room temperature and continuous-wave operation.

Contents

Chapter 1

Introduction

1.1 Silicon photonics

Photonic integrated circuits is a technology to integrate multiple photonic components with different functions on a single chip to achieve a compact optical system for various applications. The traditional platform of photonic integrated circuits includes silica, lithium niobate, or compound semiconductors such as GaAs or InP [1–7]. Si photonics is an emerging technology to leverage the high maturity, high volume, and low-cost silicon fabrication technology initially developed for electronic foundries to manufacture low-cost and high-performance photonic integrated circuits on the Si platform. The development of Si Photonics was initially driven for high bandwidth and low-cost transceivers to meet the requirements of the rapid growth of data centers [8–12] and then extended to other various emerging applications such as LiDAR [13–17], microwave photonics [18–20].

1.2 Semiconductor lasers

Semiconductor lasers are those whose gain medium and optical resonant are made of semiconductor material. For example, two cleaved laser facets can be the resonator mirror to form a Fabry-Perot (FP) cavity, which is the structure of standard FP semiconductor lasers. The most common gain medium of semiconductor lasers is the semiconductor quantum well (QW) structure, which has been developed for more than forty years [21] and is still the most common active medium in commercial semiconductor lasers. The commonly mature QW-based

semiconductor laser material system, for example, contains InGaP or InGaAsP QW on GaAs substrate for red light laser or near-infrared lasers (wavelength from 630 nm to 1060 nm) [22,23], InGaAsP QW on InP substrate for telecom applications (such as 1310 nm, 1550 nm) [24], InGaN QW on GaN substrate for visible light lasers [25].

1.3 Quantum dot lasers

Compared with the QW structure, where the carriers are confined in a plane or there is a one-dimension (1D) carrier confinement, the Quantum dot (QD) is a small volume of semiconductor material with a nanometer feature size where there is a three-dimension (3D) confinement for the carrier. The concept of the QD laser was first brought up in 1982 [26]. After that, the QD laser

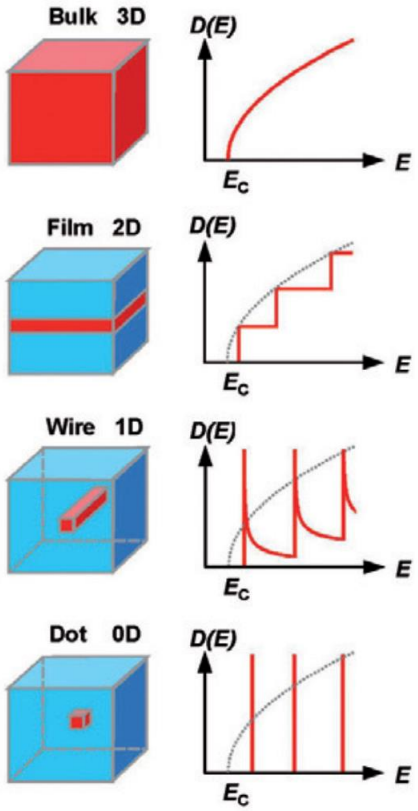

Figure 1.1. The density of states for different quantum confinement structure, including (a) bulk semiconductor, (b) quantum well, (c) quantum line, and (d) quantum dot [133].

has experienced rapid growth and demonstrated many unique properties compared to its QW counterpart, including high wall-plug efficiency [27], low threshold current density [28,29], high characteristic temperature [30–32], and high defense against defects in hetero-epitaxy [33], etc.

The unique properties of QD laser mainly come from the distinctive density of state distribution. QD structure has a 3D carrier confinement, resulting in a discrete line shape of the density of states distribution, shown in the following figure about the density of states for different quantum structures in Fig. 1.1. This means a significant density of states in a narrow energy range, leading to a high material gain. Because of the high material gain, the threshold current density can be significantly reduced correspondingly. QD laser has demonstrated ultralow threshold current density in recent decades more than QW lasers. Fig. 1.2 well shows the roadmap of the low threshold current density of QD laser and the comparison with traditional active medium including QW structure or double heterostructure.

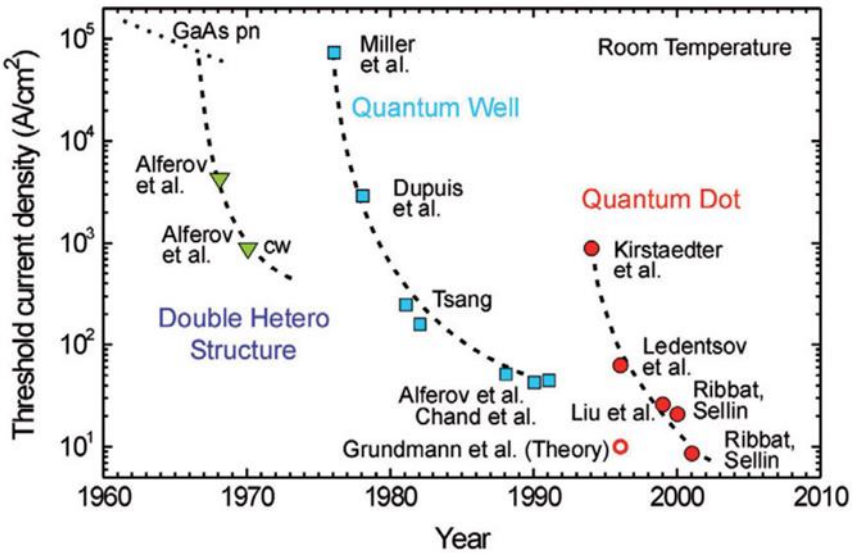

Figure 1.2. Roadmap of development of threshold current density for different active medium including double hetero stucrue, qutanum well and quantum dot [133].

1.4 Quantum dot lasers on Si

A monolithically integrated laser source on Si is highly desired to achieve photonic integrated circuits with complete kinds of functional components. This makes the direct epitaxy of III-V semiconductor laser material on Si significant. However, due to the high lattice

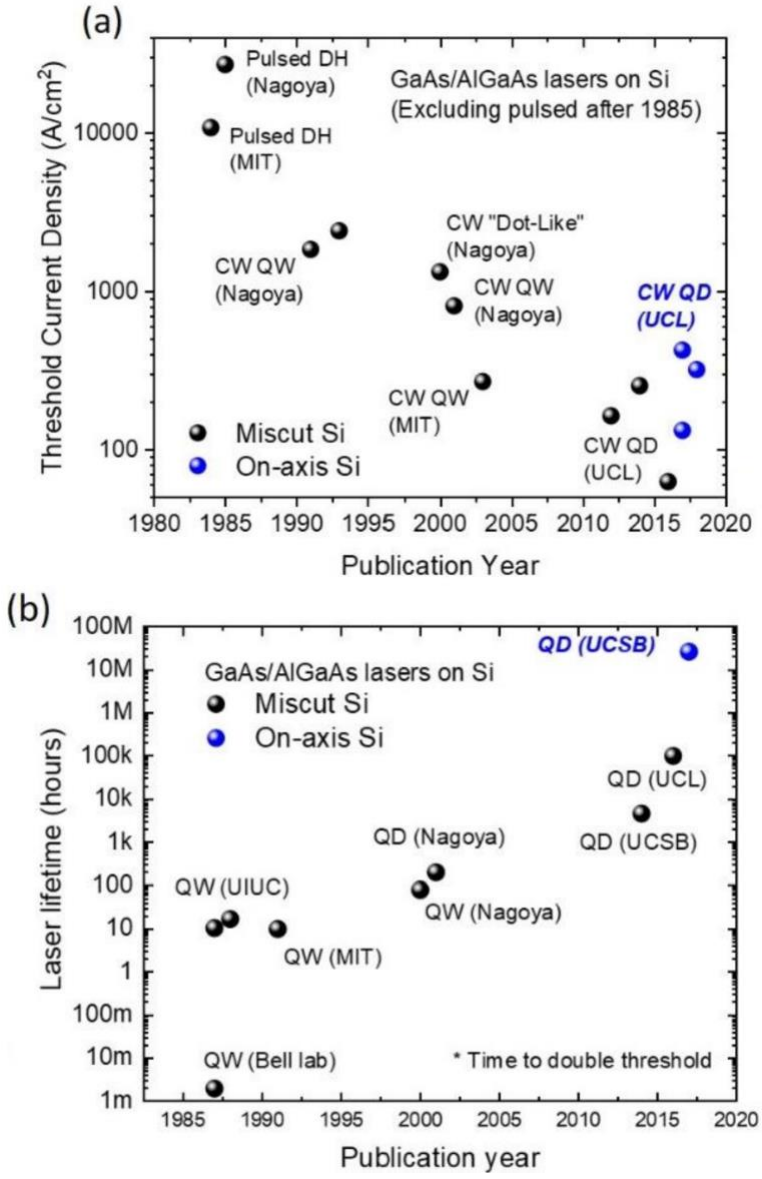

Figure 1.3. Reduction in threshold current density and increasing in laser lifetime for direct grwowht of laser on Si, enabled by development of QD laser on Si [131].

mismatch and thermal expansion coefficient mismatch between typical III-V material (such as InP and GaAs) and Si, defects will be formed in the grown III-V layer on Si, including threshold dislocations, cracks, and antiphase domains. As for the QW laser grown on Si, the active region suffers increased non-radiative recombination. However, QD lasers on Si have shown great defense against defects, significantly improving laser performance on Si, illustrated in Fig. 1.3.

1.5 Outline of the thesis

The thesis summarizes the work on the performance of high-performance MOCVD-grown QD laser on native GaAs substrate, QD laser on Si for a monolithic light source for Si photonics, and the outlook of more advanced devices or applications based on QD technology. The thesis is outlined as follows. The second chapter will introduce the fundamental physics of QD lasers and the development of QD material grown by metal-organic chemical vapor deposition (MOCVD). In the third chapter, we will review the whole laser growth of the QD laser, fabrication, and metrology results. The fourth chapter is related to QD laser on Si, which contains two parts. The first is GaAs on Si template development, and the second is the QD laser growth on the GaAs on Si template, device fabrication, and testing. The final part explores more advanced devices or applications based on QD technology.

Chapter 2

Development of MOCVD-grown QDs

2.1 Fundamental physics of QDs

The three-dimension carrier confinement of QDs is formed by the nanometer feature size of the dot material and the bandgap offset between the QD and surrounding material. This three-dimension carried confinement forms a standing wave of the wave function in all three dimensions. As a result, it forms full discretization of energy states for the carriers in the QDs and the delta-function shape of the density of states distribution [34,35], shown in Fig. 2.1. This

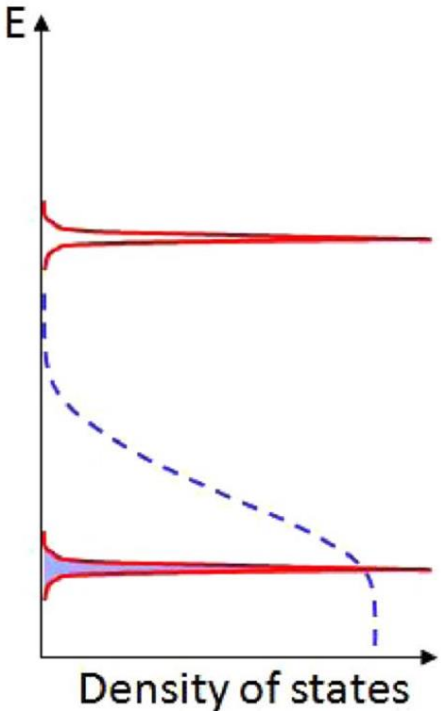

Figure 2.1. Density of states and carriers of quantum dot shows a delta function profile [35].

means significant numbers of carriers distribute in an ultra-narrow energy interval. According to Fermi's golden rule, the delta distribution of the density of states and carriers enables QD material to have a much higher gain than QW-based active medium.

The delta function shape of the density of states is just for individual QD emitters. In the real world, the QD active medium in QD lasers contains a large number of individual QDs. These individual QDs typically have an inhomogeneous dot size distribution [36–39]. The carrier energy level in QD is a function of the dot size due to the carrier confinement effect, and therefore these QDs have different energy levels. As a result, the whole QD gain medium has a broad gain spectrum than the QW gain medium. For example, our MOCVD-grown QD material shows broad photoluminescence (PL) spectrum, as shown in Fig. 2.2. However, despite the broader gain spectra, a significantly high gain has been demonstrated for QD material [40–43].

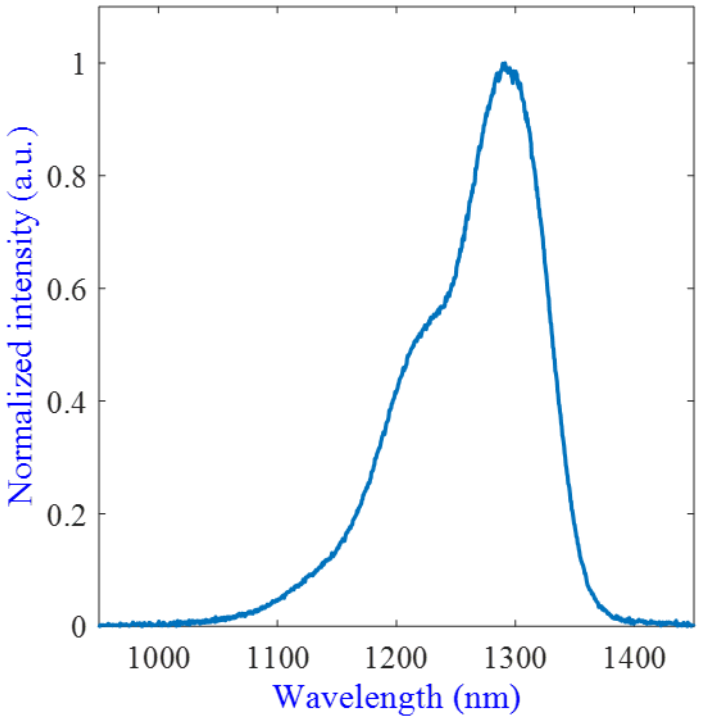

Figure 2.2. One typical PL spectrum of a QD gain medium that shows a broad peak, indicating the broad gain spectra due to inhomogeneous size of individual QD.

2.2 QD material and dots-in-a-well structure

The most mature and common QD material for semiconductor laser application is the InAs QD on GaAs substrate. The emission wavelength of InAs/GaAs QD can range from 1μm to 1.4 μm. The emission wavelength is mainly depended on the size of the dot and the strain in the dot. The dot size can influence the confinement of the carriers to influence the energy level or wave function of the energy state of the carrier; the strain can influence the lattice constant of the material and then change the wave function of the energy state of the carrier. The growth condition, such as growth temperature, V/III, growth rate, etc., influence the size of QDs. By optimizing the aforementioned growth parameters, MOCVD-grown QDs have been developed to

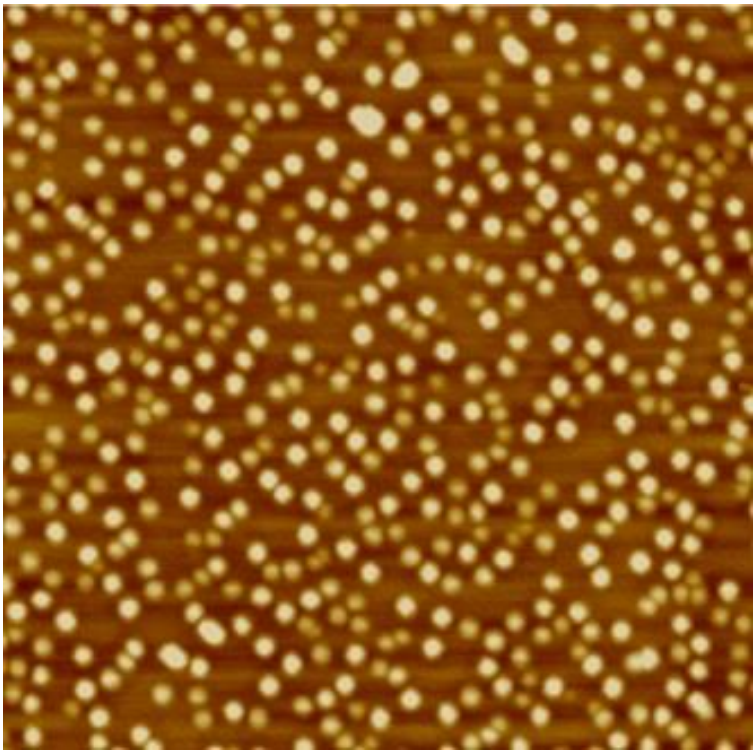

Figure 2.3. AFM images with 1 μm × 1 μm scanning shows QD with excellent dot uniformity.

demonstrate excellent dot size uniformity, shown in the atomic force microscope (AFM) image of 1 μm × 1 μm scanning in Fig. 2.3.

The most typical QD emission at 1.3 μm is InAs QDs embedded in an InGaAs QW layer, called a dots-in-a-well (DWELL) structure [44]. The emission wavelength can be well controlled by the indium composition in the InGaAs QW; therefore, the size of QD can be optimized to obtain high uniformity and density to achieve high gain. The InGaAs QW can also increase the carrier confinement, improving the injection efficiency, material gain, and characteristic temperature. The whole active region of QD lasers can contain many layers of DWELL structure, and GaAs spacer layers separate adjacent DWELL layers, illustrated in Fig. 2.4.

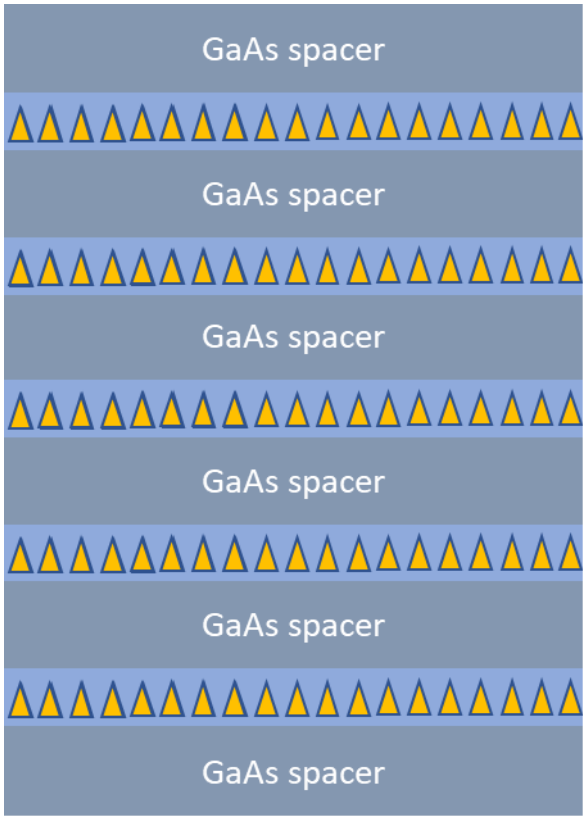

Figure 2.4. Illustrate one typical QD active medium, containing five layers of DWELL separated by GaAs spacer layers.

2.3 Unique properties of QD lasers

InAs/GaAs QD lasers based on the DELLL active region structure have demonstrated unique properties to their QW counterpart, thanks to the different energy level structures of QD lasers.

2.3.1 Low threshold current and high characteristic temperature

For semiconductor lasers, the threshold condition is that the total cavity loss, including mirror loss and cavity loss, is equal to the modal gain of the active medium. The optical confinement factor and the material gain determine modal gain. QD has a delta function profile of the density of states, and this results in a significant density of states. According to Femi's Golden role, the material gain is proportional to the density of states. Therefore, the QD lasers have a significant material gain. The gain is proportional to the material gain and current injection level. If the material gain is high, the current injection can be low to achieve the threshold gain. As a result, the QD laser has a low threshold current.

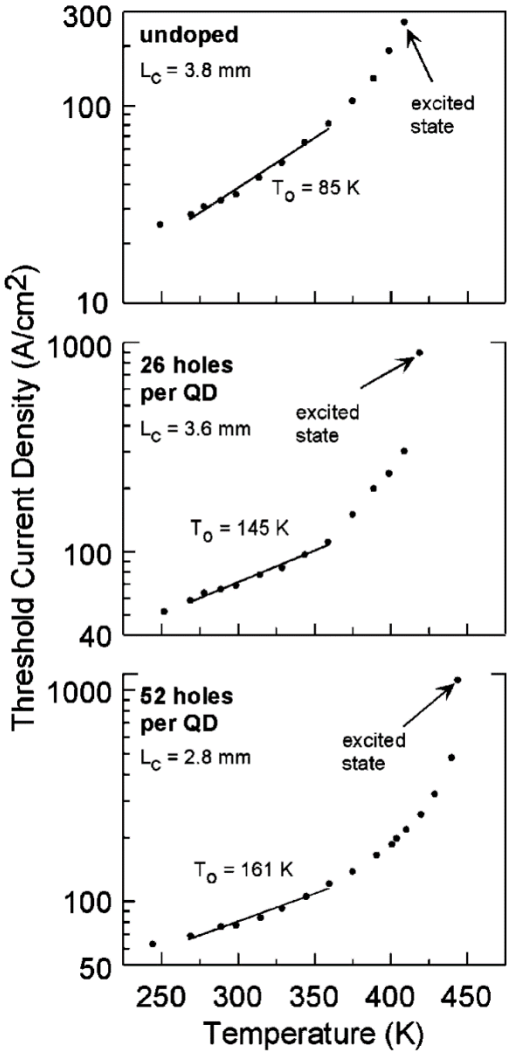

Figure 2.5. Influence of p-doping in QD active region on Characterization temperature [134].

QD laser can bring high thermal stability (high characteristic temperature) because the delta function distribution of the density of states enables the carrier population to be less sensitive to thermal redistributing. However, two critical requirements exist to achieve the high characteristic temperature in real devices. The first one is the uniformity of QDs, which determines the linewidth of the ground state, and the separation between the ground state and the first excited state. A ground state with a full width at half maximum (FWHM) of about 24

mev and an 80 mev separation between the ground state and the first excited state has resulted in a 170 K characteristic temperature[45]. The other critical requirement for high characteristic temperature is the p-doing in the QD active region. For QD laser, one thing that needs to be realized is that the separation of sub-level for holes is much smaller than that of electrons. The holes at ground states can be depleted due to thermal escape to excited states, which results in the characteristic temperature of the QD laser being limited by the thermal escape of holes rather than electrons. To overcome the problem of thermal escape of holes, additional holes are essential, which can be implemented by doping the spacer layer between two DWELL structures. Fig. 2.5 shows the influence of p doping in the QD for the characteristic temperature of QD lasers. However, because additional p doping is located at the active region that overlaps with the optical mode profile, the high free carrier plasma effect of holes can increase the absorption loss, and the absolute value of threshold current will also increase. Therefore, there is also a trade-off between the characteristic temperature and threshold current density. This can be an essential rule for QD laser full-layer stack design.

2.3.2 linewidth enhancement factor

QD laser material has highly different linewidth enhancement factors than its QW part. The linewidth enhancement factor, α, quantifies the ratio of change of the real (n) and imaginary parts (n_i) of the refractive index as the carrier density (N) changes. The imaginary parts of the refractive index can be written into the wavelength (λ) and gain (g) as follows [46].

$$\alpha = \frac{\frac{dn}{dN}}{\frac{dn_i}{dN}} = -\frac{4\pi}{\lambda}\frac{\frac{dn}{dN}}{\frac{dg}{dN}} \quad (1)$$

The linewidth enhancement factor, α, is a fundamental parameter to determine the linewidth of semiconductor lasers, which is proportional to $(1+\alpha^2)$. QD lasers have demonstrated an ultra-small linewidth enhancement factor [47–50]. QD laser has a symmetrical distribution of density of states. Therefore, the gain spectrum and the differential gain also have symmetrical gain spectra. According to the Kramer-Kronig relationship, the differential refractive index will be zero at the gain peak. As a result, the linewidth enhancement factor will also be zero at the gain peak. In the actual case, due to the inhomogeneous size of the QDs, the linewidth of the gain spectra will be broadened to a gaussian shape rather than a delta-function. There are two critical requirements to achieve an ultra-small or zero linewidth enhancement factor. The first one is the uniformity of QDs. Due to the inhomogeneous dot size, the density of states of the whole QD active medium will be broadened. Ultra-low linewidth enhancement factor has been achieved experimentally with a minimal inhomogeneous distribution of dot size [51], and recently calculation results show that zero linewidth enhancement factor can be achieved if the FWHM of the ground state is below 16 meV [52]. Second, hole depletion is a problem for QD laser due to the closer subband separation than the electron. P-doped for the QD active medium can compensate for the hole depletion to increase the differential gain and therefore be essential for a small linewidth enhancement factor [47].

The small linewidth enhancement factor enables QD to be promising for narrow linewidth laser output, which is critically important to many applications such as coherent communication, microwave photonics, and frequency-modulated continuous wave (FMCW) Lidar.

Thanks to the small linewidth enhancement factor, another promising application of QD laser is to develop a single-mode laser with low sensitivity of back reflection. The optical feedback must be controlled below at least -30 dB for traditional QW laser to maintain single-mode operation. As a result, there has to be a large isolator between the laser source and the rest of the optical components. The isolator might be larger than the semiconductor laser itself. The defense of semiconductor laser to optical feedback can be quantified by the item critical level f_{crit}, which scale as

$$f_{crit} \propto \frac{1+\alpha^2}{\alpha^4}. \quad (2)$$

From equation (2), we can learn that a small linewidth enhancement factor can bring a high critical level to optical feedback. Experiments also demonstrate that QD has low sensitivity to optical feedback [53,54].

2.3.3 Application in high-speed optical interconnect

QD laser has a discrete subband energy diagram, and the gain of individual emitters is decoupled in the active region, enabling QD to have ultra-high gain recovery speed [55–57]. The carrier relaxation time to ground state can be in the femtosecond scale, while the QW laser typically has a carrier relaxation time in a range of picoseconds and nanoseconds. This high gain recovery time should enable the QD laser to have a higher modulation speed than the QW laser. However, the current high-speed modulation record is still dominated by QW semiconductor lasers. One hypothesis is that the phonon bottleneck is the key artifact to de-efficient the carrier capture to the ground state due to the much larger separation energy of the sub-level than the phonon energy [58]. However, new research reveals that the highly efficient Auger in the QD active medium can suppress this phonon bottleneck effect which allows a fast gain recovery process [59]. It should be reasonable to assume that the reason for

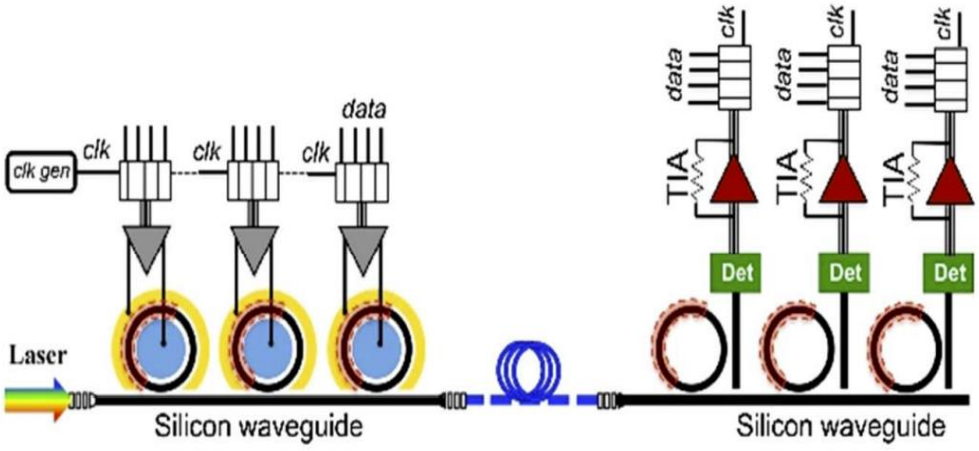

Figure 2.6. One proposed photonic link architecture, including a multi-wavelength comb source, a cascade micro-ring modulator, micro-ring add-drop filter and detectors [61].

not demonstrating the QD laser with a modulation speed as high as the QW laser is that the QD laser has not been fully engineered for high-speed modulation applications.

Nevertheless, the ultra-high gain recovery process enables the QD laser to demonstrate a mode-locked laser with a very ultrashort optical pulse than what has been demonstrated for QW lasers [60]. Moreover, due to the ultralow linewidth enhancement factor and the decoupled gain in the individual emitters in the QD active region, the QD laser has demonstrated an ultra-low mode partition noise. As a result, QD mode-locked laser can have very low relative intensity noise (RIN). This means that QD mode-locked laser can become a comb light source with constant mode spacing and low-intensity noise, which is highly

desirable for the next-generation low-cost, low power consumption, small footprint, and high-speed transceiver applications.

As shown in Fig. 2.6, one proposed optical communication architecture contains a comb laser source, which can be a QD mode-locked laser, a single-mode waveguide on silicon photonics or fiber, a cascade micro-ring modulator, a cascade micro-ring add-drop filters, and detectors [61].

2.3.4 Reduced sensitivity to dislocations

Monolithically growth of QD laser on Si has been a highlighted topic in the past decade thanks to the merit of QD laser of low sensitivity to the threading dislocation in the epitaxy laser by heterogeneous growth of III-V material on Si [62–65]. The influence of threading dislocation is the non-radiative recombination of carriers due to the deep energy formed in the dislocation position. For QW active region, there is only carrier confinement in the direction perpendicular to the epitaxy layer, and the carrier can be freely diffused in the plane of the epitaxy layer. During the operation of QW lasers, the diffusion length of electronics is

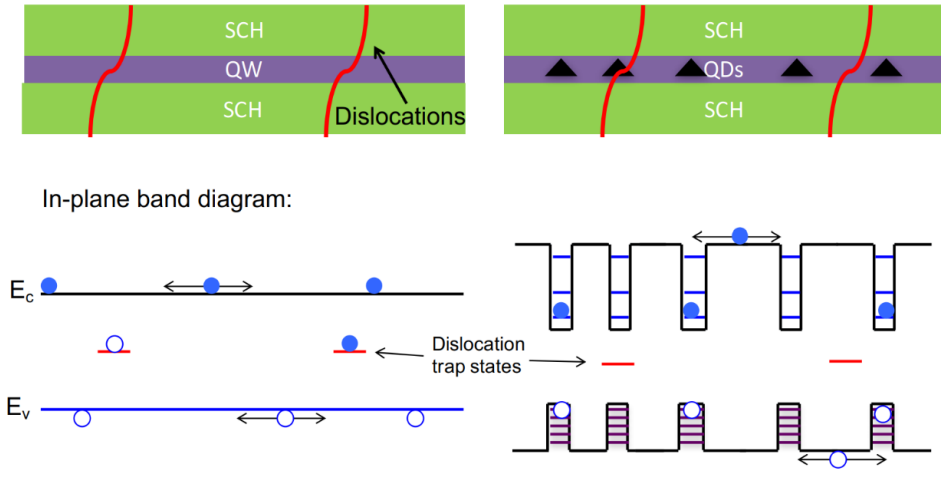

Figure 2.7. This diagram shows the physics of less sensitivity of QD laser to threading dislocation [135].

in the order of microns. However, the typical distance of threading dislocation of III-V grown on Si is also in the order of microns. Therefore, the performance of QW laser directly grown on Si suffers significantly from the non-radiative recombination due to the threading dislocations. Nevertheless, the carrier diffusion length is in the order of hundreds of nanometers in the QD active medium due to the three-dimensional carrier confinement, shown in Fig. 2.7. This means that the carrier is mainly localized within or nearby the QDs. If the QD density is significantly high than the threading dislocation density, the performance of the QD laser can be less influenced by the threading dislocations.

Because of the low carrier diffusion length in the lateral direction, the QD laser on Si has demonstrated increased output power and reduced threshold density than the QW laser on Si. Moreover, the lifetime of QD lasers on Si can also increase significantly more than QW on Si. One threshold dislocation will influence a QD only if the threshold dislocation crosses the QD or is close to the QD. For self-assembled growth QD, a strain field surrounding the QD can push the thresholding dislocation away during the growth. Besides, as for the QW laser, when it is aging, the threading dislocations can climb and merge to form giant defects, which can significantly degenerate the laser performance. Therefore, QW laser on Si has a very short lifetime. For the QD laser, as aforementioned above, the stain of the QD can push away the threading dislocation during growth. It can do the same thing when the QD laser is aging, decreasing the climbing distance of the threading dislocation to avoid forming giant defects such as in QW active medium. Therefore, the lifetime of the QD laser on Si can significantly increase. QD laser grown on Si with a long lifetime suitable for practical application has been demonstrated [62]. Even though there is still a gap between the current state-of-the-art reality

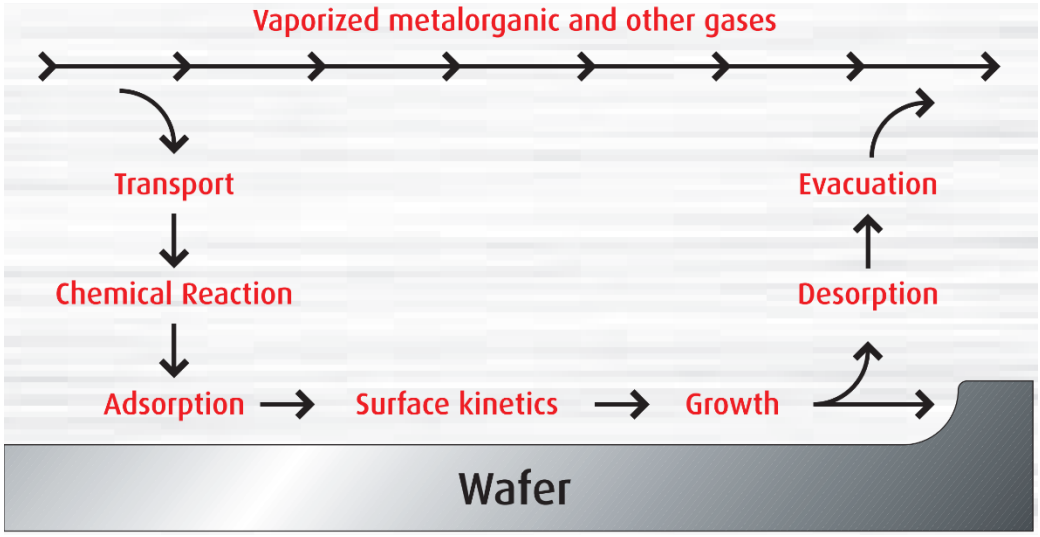

Figure 2.8. The mechanism of MOCVD growth process (acquired from Osram website).

of QD laser on Si and the requirement for the communication application, the gap is no longer out of reach.

2.4 Introduction of MOCVD growth technology

MOCVD, whose full name is Metal-Organic Chemical Vapor Deposition (MOCVD), is a technique for growing semiconductor thin films on a substrate. Using MOCVD technology, many nanolayers can be deposited with great precision, each with a controlled thickness, to form materials with specific optical and electrical properties. In the current industry, MOCVD is a key process technology for optoelectronic devices such as semiconductor lasers and light-emitting diodes (LED).

In the MOCVD growth process, the reaction precursors, such as group III metal-organic compounds and hydrides of group V elements, are first transferred into the reaction chamber. A part of the mixed gas flows over the heated wafer surface and undergoes thermal decomposition. The decomposed precursors will first be adsorbed on the wafer surface and transported along the

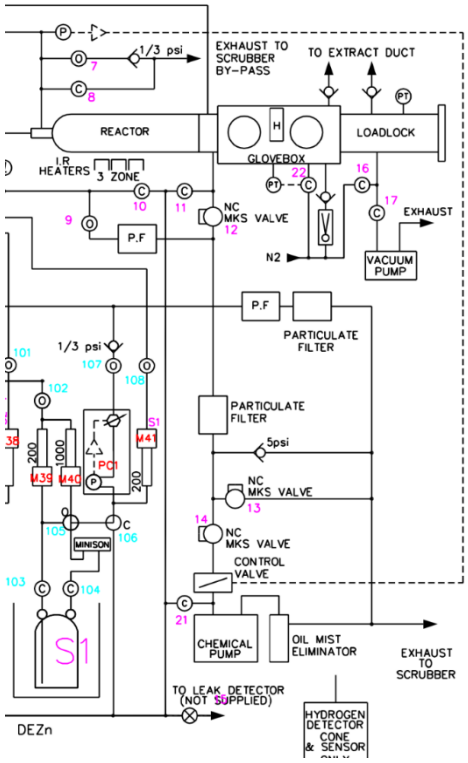

Figure 2.9. The MOCVD gas circuit diagram showing the different parts of the MOCVD system.

wafer surface with some surface kinetic process. Some adsorbed atoms will be incorporated into the crystal structure of the wafer, and the others will escape from the wafer surface and finally go to the exhaust gas. Fig. 2.8 shows the diagram of the MOCVD growth mechanism.

The MOCVD system can be briefly divided into four parts: gas operating system, the reaction chamber, the heating system, and the exhaust gas treatment system, illustrated in Fig. 2.9. The gas operating system includes all the valves, pumps, and various equipment and pipelines used to control the gas stream of the Group III metal organic source and the Group V hydride source and their mixtures. The most important part is the precise control of the amount of raw materials that are fed into the reaction chamber for reaction. The main components are the

mass flow control meter (MFC) for flow control, the pressure controller (PC) for pressure control, and the water bath for temperature control of the metal-organic source bubbler.

The reaction chamber is the core component of the MOCVD growth system, and the design of the chamber has a crucial impact on the growth effect. The design of the reaction chamber varies from one MOCVD equipment manufacturer to another. The basic design rule is to avoid turbulence in the reaction chamber and to ensure that only laminar flow exists to achieve uniform distribution of airflow and temperature in the reaction chamber, which is conducive to large-area uniform growth. In the experiment in this thesis, the reactor is a horizontal structure. A long taper structure ensures that the mixed flow maintains laminar flow before reaching the wafer holder area. The ceiling of the reactor has a tilted angle to ensure a uniform boundary layer thickness along the wafer holder area to ensure uniform thickness growth.

Compared with other epitaxial growth techniques, MOCVD technology has the following advantages. First, the source used to grow compound semiconductor materials are passed into the reaction chamber in a gaseous state, so the epitaxial layer's composition, dopant concentration, and thickness can be controlled by precisely controlling the flow rate of the gas source. This merit can grow ultra-thin layer materials with high accuracy. Second, the gas flow rate in the reaction chamber is fast. Therefore, when it is necessary to change the composition and doping concentration to grow a multi-layer structure, the change can be made quickly, reducing the possibility of memory effects, which facilitates the acquisition of steep interfaces and is suitable for the growth of heterostructures and superlattice and quantum well materials. Third, crystal growth is carried out in a pyrolytic chemical reaction, which is a single temperature zone epitaxial growth. Therefore, the homogeneity of the epitaxial material can be guaranteed as long as the uniformity of the reaction source airflow and temperature distribution is well controlled.

As a result, it is suitable for the epitaxial growth of multiple pieces and large pieces, which is convenient for industrial mass production. Forth, the crystal growth rate is proportional to the flow rate of the group III source so that the growth rate can be adjusted in a wide range. The faster growth rate is suitable for high-volume production in the industry.

2.5 QDs growth by MOCVD

Since the concept of using three-dimensionally quantum confined structures in lasers was initially put up 30 years ago, InAs self-assembled quantum dot systems, have continuously developed from being a pure thought to commercialization [66]. Compared to their quantum well counterparts, they promise a lower threshold, more stable functioning at different temperatures, and a more comprehensive wavelength tunability range for semiconductor laser applications. The recent demonstration of InAs quantum dot (QD) lasers as viable light sources on silicon for silicon photonics applications is even more fascinating [62]. The InAs/GaAs system has received the majority of attention in the research on self-assembled QDs. It involves the growth of InAs self-assembled QDs in a GaAs or AlGaAs matrix. When developed, if adequately implemented, the emission wavelength from InAs QDs on GaAs can be increased into the telecom windows of 1.3 um. By using a high indium composition InGaAs capping layer, 1.5 m um can also be reached, which usually requires InGaAsP quaternary material grown on an InP substrate. GaAs substrates are preferable for future low-cost semiconductor laser solutions because they are generally of higher quality, less expensive, and have superior thermal conductivity than InP, making them an attractive choice.

Due to industrial needs, MOCVD technology has developed quickly to the point where it can currently compete with MBE in terms of material quality, with the latter being chosen by the industry due to its higher throughput and simpler maintenance requirements than MBE.

Nevertheless, MBE is now growing commercial quantum dots because they are of higher quality (see Innolume and QD Laser Inc). Therefore, achieving high-quality InAs QD growth and associated devices by MOCVD is desirable. MOCVD-grown QD lasers have been developed [67,68], but the performance is still not as excellent as that of MBE-grown QD lasers. Systematical research of MOCVD-grown lasers is essential to understand the improving space of MOCVD-grown QD lasers.

2.5.1 Stranski-Krastanov Growth mode of QDs by MOCVD

Stranski-Krastanov (SK) growth mode, in which initial 2D paedomorphic growth of an InAs "wetting layer" transforms to three-dimensional growth once a certain thickness is reached, gives rise to the formation of InAs self-assembled QDs through strain relaxation [69]. This critical thickness is typically on the order of monolayers, and beyond this point, only a very narrow window of defect-free dot growth is possible (up to around 3 MLs for InAs on GaAs), after which additional deposition results in the production of dislocations. Self-assembled QDs and QD lasers were historically developed in MBE, and progress in MBE in this area typically came before advances in MOCVD [70]. Two years after the discovery of self-assembled QDs, PL emission at 1.3 m was accomplished [71]. Soon after, ground-state lasing was accomplished, and it took MOCVD ten years to achieve ground-state lasing at 1.3 m [72]. Early MBE growth is significantly more precise than MOCVD due to the ease with which the 2D to 3D growth mode shift may be observed using in situ characterization methods. In addition to lacking the monolayer precision control of MBE, the near atmospheric reactor pressure reduced mean free path, complicated chemical reactions, adduct formation, and small overlap of efficient precursor pyrolysis with the sensitive growth windows of InAs QDs were all contributing factors to the difficulty in MOCVD growth of self-assembled QD.

The dots should emit at the correct wavelength and be homogeneous, dense, coherent, and defect-free in to provide a large material gain for laser applications. These constraints impose several contradictory restrictions. For instance, the surface adatoms' lengthy diffusion lengths are required for size uniformity throughout the dot ensemble, but this comes at the cost of fewer nucleation sites and a lower density. Larger dots must be developed to attain longer emission wavelengths, but if too much indium is added, the larger dots begin to plastically relax, reducing their optical performance. Aluminum-containing cladding layers are frequently used in GaAs-based lasers to promote optical and electrical confinement. However, Al-containing layers demand relatively high growth temperatures in both MBE and MOCVD, which could result in In-Ga interdiffusion and reduce the optical quality of the dots. The effort of optimization of MOCVD growth of self-assembled QD by the work of this thesis will be covered in the following sections.

2.5.2 Precursor Selection

At our MOCVD system, available metal-organic sources include trimethyl gallium (TMGa), triethyl gallium (TEGa), trimethyl aluminum (TMAl), trimethyl indium (TMIn), tributyl phosphate (TBP) and tributyl arsine (TBA) as precursors. The doping precursors contain disilane, carbon tetrabromide (CBr_4), and dimethylzinc (DMZn). TBP and TBA are utilized as group V sources because of safe consideration and also their availability for ultra-low decomposed temperatures, which enables low-temperature growth to pursue better material quality. As for gallium sources, there are two options, TMGa and TEGa. TMG is a low-cost solution suitable for nearly most of the requirements of material growth. TEG has a lower decomposition temperature than TEGa, bringing several advantages to TMG. Low decomposition temperature enables GaAs or InGaAs material growth at low temperatures,

essential for InAs/GaAs QD growth. The InAs QD is regularly grown around 500 °C. After InAs QD growth, the dot must be covered by InGaAs capping layer and the GaAs spacer layer. The InGaAs capping layer and GaAs spacer layer should not be grown at higher temperatures to avoid serious annealing of dots, resulting in dot size being out of shape. For GaAs grown by TMGa, the temperature is generally above 550 °C. However, TEGa can enable GaAs growth under a very low temperature, for example, below 500 °C. This significantly benefits the protection of QDs. Besides, low temperature is also favorable for high p-doping material. In our experiments, we found out that a low temperature (below 525 °C) is essential for high p-doped GaAs (>1E20 cm^{-3}). In this case, GaAs grown by TEGa have a significant advantage in doping and material quality. Apart from that, GaAs grown by TEGa also has a lower carbon background doping level than those grown by TMGa because of reduced background carbon doping during growth.

Disilane is chosen for the n-type dopant source over silane because of safety considerations and low decomposition temperature. Si can work as an n dopant for various materials such as GaAs, InP, AlGaAs, InGaP, and InGaAsP. There are two options for p-type dopant sources, the CBr_4 and DMzn. Carbon can be the p-type doping for GaAs material, with a low diffusion length during material growth. Carbon-doped GaAs is also favorable for high p-type doping GaAs. DMZn is a more adaptable p-type doping source for various materials such as GaAs, InP, InGaP, and InGaAsP. The drawback of Zn for p-type doping is the long diffusion length during the material growth.

2.5.3 Temperature

In contrast to molecular-beam epitaxy (MBE), which relies on elemental sources, MOCVD precursors require enough thermal energy to pyrolyze the bonds in the carrier molecule. For this

reason, the growth temperature should be such that it provides good precursor decomposition efficiency and crystal quality. If one grows in the mass transport limited region, there will typically be considerable overlap between the growth and decomposition windows. To achieve the highest luminescence efficiency of InAs QDs, MBE initially optimizes the quantity of material deposited before iterating through other growth parameters. However, as was previously mentioned, the growth temperature for the quantum dot active region in MOCVD should be optimized first because the optimal coverage will vary with temperature. This is due to the fact that the growth rate is temperature dependent (via the thermal decomposition efficiency of the group III precursors).

In order to achieve appropriate decomposition of the precursors, growth temperatures for alloys containing indium in MOCVD are typically between 600 and 650 °C.

Due to the low density and massive size of the resultant dots, along with their high indium concentration, such high growth temperatures are unsuitable for the formation of self-assembled QDs for laser applications. Additionally, the significant strain associated with these dots will act as a powerful driving force for In-Ga interdiffusion during continued subsequent growth, making them likely to become faulty after being capped with the matrix material. InAs quantum dots must be produced at temperatures comparable to MBE (about 500 °C) to attain high material gain for laser applications.

Due to the inclusion of metal-organic precursor molecules at these relatively low growth temperatures, inadequate decomposition of the precursors will result in poor growth rates and a decrease in the quality of the material. This is one of the reasons why quantum dot lasers produced by MBE are often of higher quality than those produced by MOCVD. The material quality would be enhanced, and background carbon doping would be decreased by using

TBA precursors, which disintegrate at lower temperatures. However, triethyl indium (TEIn) is less stable than TMIn. Therefore, we must continue using TMIn as the precursor for InAs development, which restricts us to low-density quantum dots and rather sluggish growth rates.

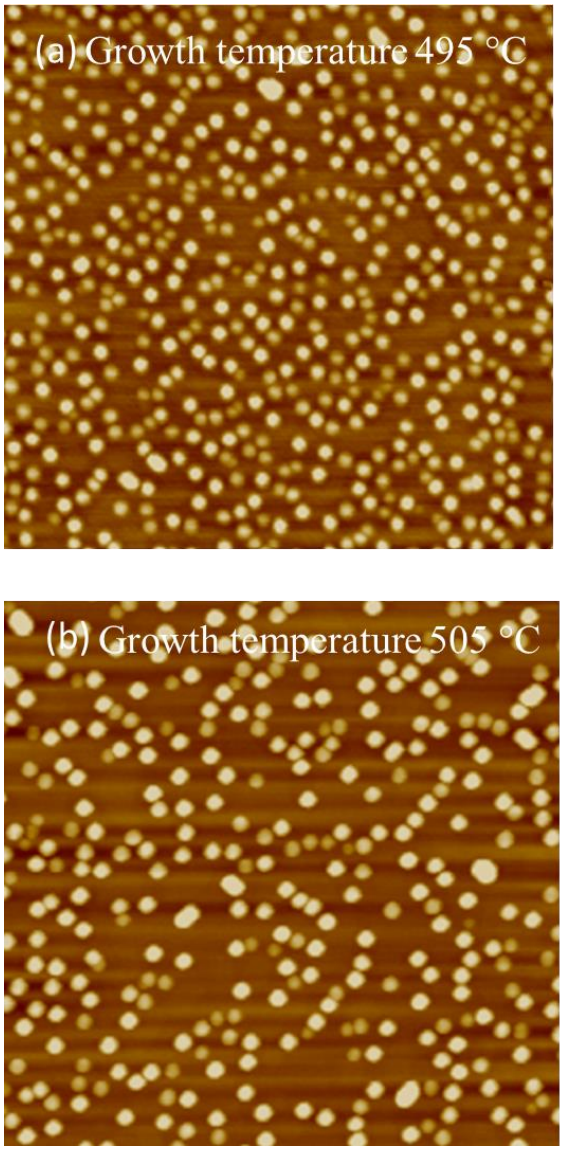

Figure 2.10. AFM images with 1 μm × 1 μm scanning shows QD surface morphology at (a) 495 °C and (b) 505 °C, indicating that the growth of QDs is highly susceptible to growth temperature.

According to the analysis mentioned above, the temperature for InAs QD growth is set from 485 °C to 505 °C. During this temperature range, the QD grown by MOCVD shows a similar

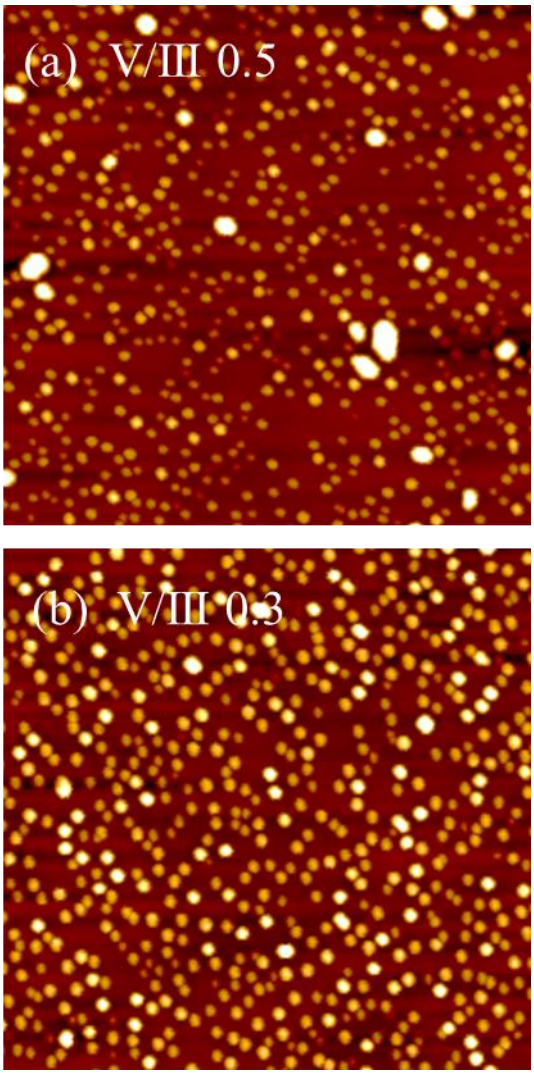

Figure 2.11. AFM images with 1 μm × 1 μm scanning shows surface morphology of QD grown at different V/III of (a) 0.5 and (b) 0.3.

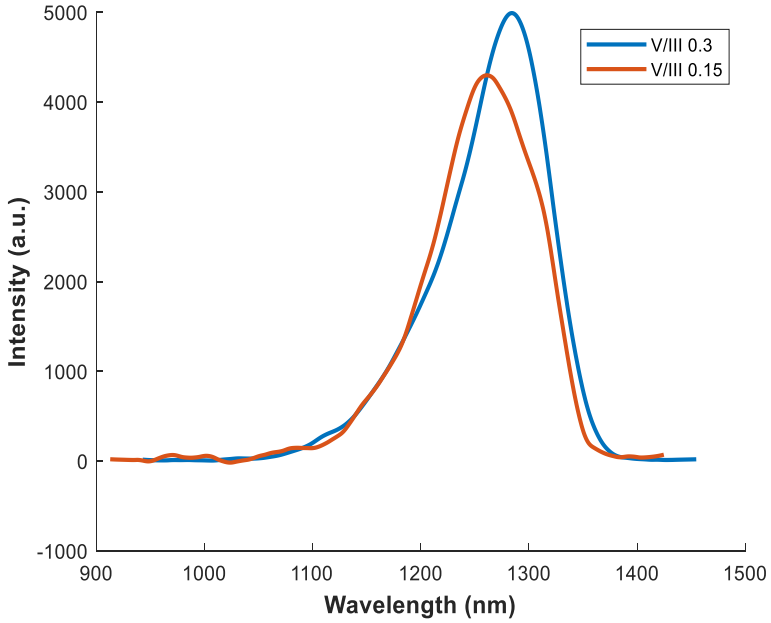

Figure 2.12. PL spectra of QDs grown under conditions with different V/III (a) 0.3 and (b) 0.15.

level of dot uniformity to MBE-grown QD with a decent dot density. QD growth is susceptible to growth temperature, as shown in Fig. 2.10. Even though the temperature variation range is just about 30 °C, we find the trade-off between the dot uniformity and dot density. High temperature can increase the indium atom surface mobility during QD growth to increase the dot uniformity. However, the high surface mobility also means fewer nucleation sites, resulting in low dot density.

2.5.4 V/III

The group V to group III flow rate ratio is known as the V/III ratio. In our experiment, the group V source for QD growth is TBA, and group III is TMIn. The V/III ratio significantly influences the QD nucleation process. V/III can also have an impact on the surface adatom kinetic process. A low V/III can enhance the adatom surface mobility, which is essential to form uniform QD size distribution in our MOCVD growth experiment (V/III is around 0.3 in our

optimized condition). A V/III above 0.5 will result in giant dots or clusters, which prevents stacking multi-layers. AFM image of QD grown under growth conditions with only difference in V/III has shown in Fig. 2.11.

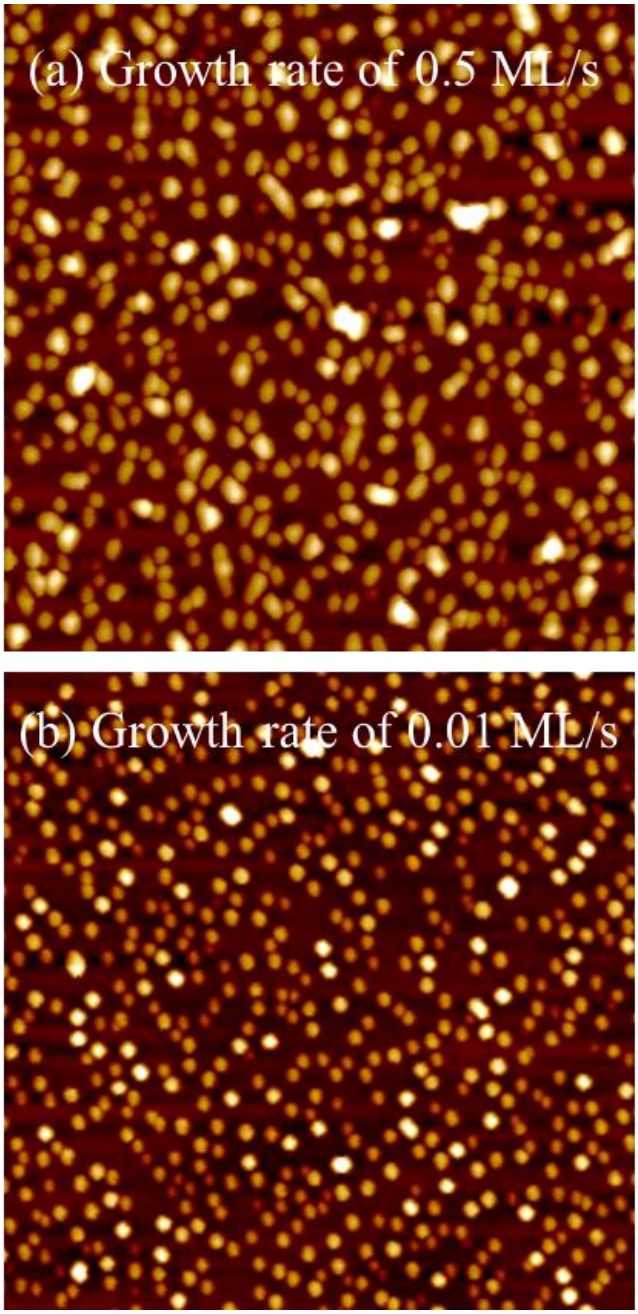

Figure 2.13. AFM images with 1 μm × 1 μm scanning shows surface morphology of QD growth at different growth rate of (a) 0.5 ML/s and (b) 0.01 ML/s.

Even though low V/III enhances surface mobility and increases the uniformity of dot size, low V/III also means low group V partial pressure, which is essential to prevent the surface of the material during growth. A low V/III can also result in a blueshift of the emission wavelength of QD, shown in Fig. 2.12 by the photoluminescence spectra (PL) of QDs growth conditions with only difference in V/III.

2.5.5 Growth rate

Growth rate plays a similar role with V/III in QD growth. The growth rate has an impact on the surface mobility of the group III atom, indium, during InAs QD growth. A high growth rate means high indium partial pressure, which can decrease the surface diffusion length during growth. As a result, giant dots or clusters can be formed. A low diffusion length can also significantly decrease the QD uniformity. We can achieve uniform QD without clusters only under a very low growth rate, about 0.01 monolayer per second (ML/s). Fig. 2.13 shows the surface morphology of QD growth at a different growth rate of (a) 0.5 ML/s and (b) 0.01 ML/s.

2.5.6 InAs coverage

InAs coverage amount has a significant influence on QD density and size. Since QD growth is by the Stranski-Krastanov Growth mode, this means QD only appears after the total InAs coverage is above the critical thickness. After that, QD density increases from 0 to the order of 1E10 cm^{-2}. The dot size and density will gradually increase after the InAs coverage increases. Figure 2.14 shows the dot density and size change as the InAs coverage increases.

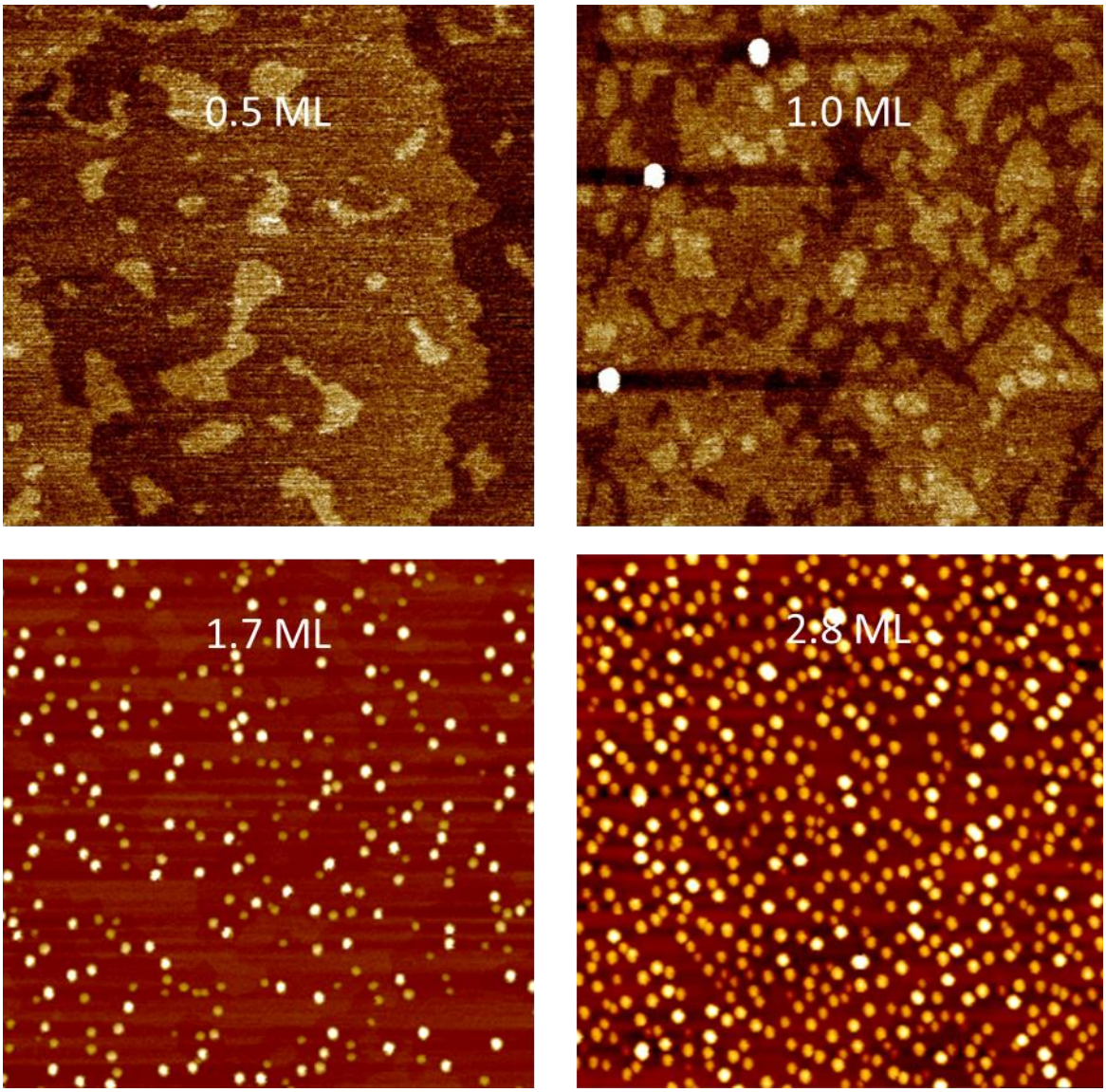

Figure 2.14. AFM images with 1 μm × 1 μm scanning shows surface morphology of QD growth at different growth rate of (a) 0.5 ML/s and (b) 0.01 ML/s.

Chapter 3

High-performance MOCVD-grown QD laser on GaAs substrate

This chapter discusses the fundamental basic theory of semiconductor lasers and the whole loop of development of InAs/GaAs QD lasers, including whole laser structure material growth, device fabrication, metrology, and lifetime validation.

3.1 Roadmap of semiconductor laser development history

In 1962, the first early demonstration of semiconduction lasers was based on homojunction diodes [73–75], in which the material of the waveguide core layer and the surrounding cladding layers are the same. This structure suffers from a meager index difference and zero bandgap offset between the core and cladding layer. This results in the semiconductor laser having ultra-low performance, such as low-temperature operation and high threshold currents. Single-heterojunction lasers were then demonstrated because of the development of the liquid phase epitaxy method. These lasers used n-type gallium arsenide layers produced on the substrate by LPE over p-type aluminum gallium arsenide injectors. Aluminum was added to the semiconductor crystal to replace gallium, which increased the bandgap of the p-type injector relative to the n-type layers below it. The bandgap offset and index difference improved the laser diode performance in the threshold current, but the laser can still work in low-temperature conditions.

Double-heterostructure (DH) semiconductor lasers enabled the first semiconductor laser to operate at room temperature [76,77]. Two layers of high bandgap material and one layer of low bandgap material make up DH lasers. Utilized material pairs include gallium arsenide (GaAs) and aluminum gallium arsenide. Because each intersection of different bandgap materials is

referred to as a heterostructure, the DH laser is given this name. A DH laser has the advantage of limiting the active zone, where free electrons and holes coexist simultaneously, to the thinnest layer of the intermediate layer. Because fewer electron-hole pairs are left in the active region, so more electron-hole pairs can contribute to stimulated emission. The heterojunction, where stimulated emission occurs, also confines light due to the index difference with surrounding layers.

The semiconductor laser performance was improved significantly after the first demonstration of QW lasers [78–84]. The transition from DH laser to QW laser is that the intermediate layer becomes sufficiently thin to function as a quantum well, which was enabled by the development of material epitaxy methods such as MBE or MOCVD technology. Because of the quantum well structure, the electron's wavefunction's vertical variation, and consequently a part of its energy, is quantized. Because of the sharp edge in the electron density of states functions in the quantum well system, which concentrates electrons in energy states that contribute to the material gain of the active region. This enables QW laser performance to improve scientifically than bulk lasers. The multi-QW laser that contains more than one QW in the active region was then invented to increase the overlap of the QW region with the optical waveguide mode, further improving the QW laser performance.

The next generation of the semiconductor laser is the Quantum dot laser, which was first hypothesized in 1982 [85]. Quantum dot has a three-dimension carrier confinement compared with the QW laser, where the carriers have quantum confinement in one dimension. As described in the second chapter, quantum dot lasers have exhibited several performance benefits over quantum well devices, including lower threshold currents, higher temperature operation, enhanced stability against optical feedback, decreased crystalline defect sensitivity, ultrafast gain

dynamics [55–59,86], and mode-locked lasers (MLL) [87–90]. These benefits result from the discrete state density and inhomogeneously expanded gain spectra.

3.2 The basic principle of Semiconductor lasers

The emission principle in the semiconductor laser is stimulated emission, which is different from the light-emitting diode (LED), whose emission is based on spontaneous emission. As for lasers, electron-hole recombination photons must be confined in a resonant cavity with feedback from mirrors or other grating structures that can produce reflections in semiconductor lasers [91]. The injected carriers (electrons and holes) are recombined in the quantum wells and emit photons. When the population of photons reaches a particular threshold, the created photons will compel more photons to be released owing to population inversion, and the stimulated emission becomes dominant.

Low index layers should sandwich the active region to confine the light to form a waveguide structure. Separated confining heterostructure (SCH) surrounding the active region is commonly used. There will always be a certain degree of optical loss because of the properties of the absorption loss (dopants, bandgaps) [92–95], scattering loss (sidewall roughness) [96]. The gain will exceed the loss as the current keeps rising and more carriers are pushed in. The threshold condition is the point at which gain exceeds loss. The cavity is absorbing and not transparent when the current density is below the threshold.

Some basic parameters about semiconductor lasers will be introduced in the following parts.

Optical internal loss, α_i, is the parameter to quantify the optical loss due to the laser material within the cavity. There are mainly two parts that contribute to the internal optical loss. The first is the absorption loss, which comes from the bandgap and free-carrier absorption due to the

doping in the cladding layers. Regularly, the p-type carrier absorption is much higher than the n-type carrier absorption [97,98].

Mirror loss, α_m, is the parameter to quantify the cavity loss due to photons escaping from the mirror. Mirror loss is a concept relative to the cavity quality factor, not an actual loss, because the parts of photons escaping from the cavity become the laser output. For typical Fabry-Perot (FP) cavity lasers, the mirror loss can be defined in the following equation [91]:

$$\alpha_m = \frac{1}{2L} Ln \frac{1}{R_1 R_2}. \quad 3.1$$

L is the cavity length; R_1 and R_2 are the reflectivities at the two mirrors. The laser threshold condition is that modal gain is equal to the total optical loss, which is described in the following equation:

$$\Gamma g_{th} = \alpha_i + \alpha_m. \quad 3.2$$

Here, Γ is called the optical confinement factor, which quantifies the overlap of the optical mode with the gain area in the active region. From this equation, we realize that decreasing the optical loss and increasing the optical confinement factor decreases the threshold current. As for the mirror loss, there is a trade-off relationship between the output power and the threshold current. For example, a shallow mirror loss can decrease the threshold current and sacrifice the total energy efficiency because most photons will be confined within the cavity.

The carrier and photon dynamics in the laser cavity can be described in the rate equation [91]:

$$\frac{dN}{dt} = \frac{\eta_i I}{qV} - \frac{N}{\tau} - V_g g N_p, \quad 3.3$$

$$\frac{dN_p}{dt} = \Gamma V_g g N_P + \Gamma \beta_{sp} R_{sp} - \frac{N_p}{\tau_p}. \quad 3.4$$

Eq. 3.3 is the rate equation for the carriers. N is the carrier density in the active region. η_i is the injection efficiency, representing the percentage of terminal current that produces carriers in the active region. It is crucial to understand that this definition encompasses all carriers injected into the active region, not simply those that generate radiative recombination. I is the injection current, and q is the charge of an individual electron. V is the volume of the active region. τ is the carrier lifetime, counting the impact of spontaneous emission, nonradiative recombination, and carrier leakage. V_g is the group velocity in the laser cavity. g is the gain rate of the active region. Eq. 3.4 is the rate equation for the photon density. N_p is the photon density in the active region. The percentage of the total spontaneous emission coupled into the lasing mode is known as the spontaneous emission factor, β_{sp}. τ_p is the photon lifetime, representing the rate of consumption of photons by the internal loss and the mirror loss for the cavity.

According to the rate equation of semiconductor lasers, the carrier density, photon density, and gain will collapse at their threshold value as long as the laser is lasing or operating above the threshold current. The steady-state gain of a laser operating above the threshold must coincide with the threshold value. If the gain were more than the threshold gain, which is impossible in the steady state, the field amplitude would continue to grow without bounds. Additionally, because of the monotonic relationship between the gain and carrier density, the carrier density must clamp at its threshold value. In practice, when the current is raised to a value above the threshold, and the photon density rises, the carrier density and gain first climb above their threshold levels (on a millisecond scale). A drop follows the increase in stimulated recombination in carrier density and gain, which continues until a new steady-state dynamic equilibrium is attained. In other words, the accelerated recombination term consumes every

additional carrier injection above the threshold. The feedback effect causes the carrier density to clamp, keeping the gain constant at the threshold value.

According to the rate equation, the output power verse injection current relationship can also be derived in terms of the following equation,

$$P_o = \eta_d \frac{h\nu}{q}(I - I_{th}), \qquad (I > I_{th}) \tag{3.5}$$

The differential efficiency η_d is defined by

$$\eta_d = \eta_i \frac{\alpha_m}{\alpha_m + \alpha_i}. \tag{3.6}$$

Below threshold current, the relationship is identical to LED, as shown in the following equation,

$$P_o = \eta_r \eta_i \frac{\alpha_m}{\alpha_m + \alpha_i} \frac{h\nu}{q} \beta_{sp} I. \tag{3.7}$$

The P-I curve is essential for laser characterization to extract the critical parameters of lasers, such as internal loss α_i and injection efficiency η_i. Two or more lasers of various lengths can be made from the same material and equipped with similar mirrors to measure these crucial internal properties. This is relatively simple for in-plane lasers because the length may change at the very end when cleaving. According to Eq. 3.1, Eq. 3.5 and Eq. 3.6.,

$$\eta_d = \frac{\eta_i \ln\left(\frac{1}{R_1 R_2}\right)}{2L\alpha_i + \ln\left(\frac{1}{R_1 R_2}\right)}, \tag{3.8}$$

and

$$\eta_d' = \frac{\eta_i \ln\left(\frac{1}{R_1 R_2}\right)}{2L'\alpha_i + \ln\left(\frac{1}{R_1 R_2}\right)}, \tag{3.9}$$

where we have two laser cavity lengths, L and L′. Thus, we can find

$$\alpha_i = \frac{\eta_d' - \eta_d}{2L\eta_d - 2L'\eta_d'} \ln\left(\frac{1}{R_1 R_2}\right), \tag{3.10}$$

And

$$\eta_i = \eta_d \eta_d' \frac{L - L'}{L\eta_d - L'\eta_d'}. \tag{3.11}$$

These two equations will provide the appropriate internal parameters if it is possible to create two identical lasers other than in terms of length. However, the value of these statements is generally constrained by the degree of uncertainty in experimental data. Plotting multiple data points on a graph and identifying the unknowns by fitting a curve to the data often results in higher dependability. Plotting the reciprocal of the measured differential efficiencies versus laser length L is the most practical option, as shown in the following equation,

$$\frac{1}{\eta_d} = \frac{2\alpha_i}{\eta_i \ln\left(\frac{1}{R_1 R_2}\right)} L + \frac{1}{\eta_i}. \tag{3.12}$$

As a result, the injection efficiency can be extracted from the intercept of the curve, and then the internal loss can be calculated according to the slope of the curve.

Another important metric for semiconductor lasers is the characteristic temperature, representing the changing threshold current with the temperature. Since most critical physic process determining the threshold current, such as gain, absorption loss, current leakage, and auger recombination, has exponential temperature dependence, the threshold current also can be approximately expressed in exponential temperature dependence in the following equation,

$$I_{th} = I_0 e^{T/T_0}. \tag{3.13}$$

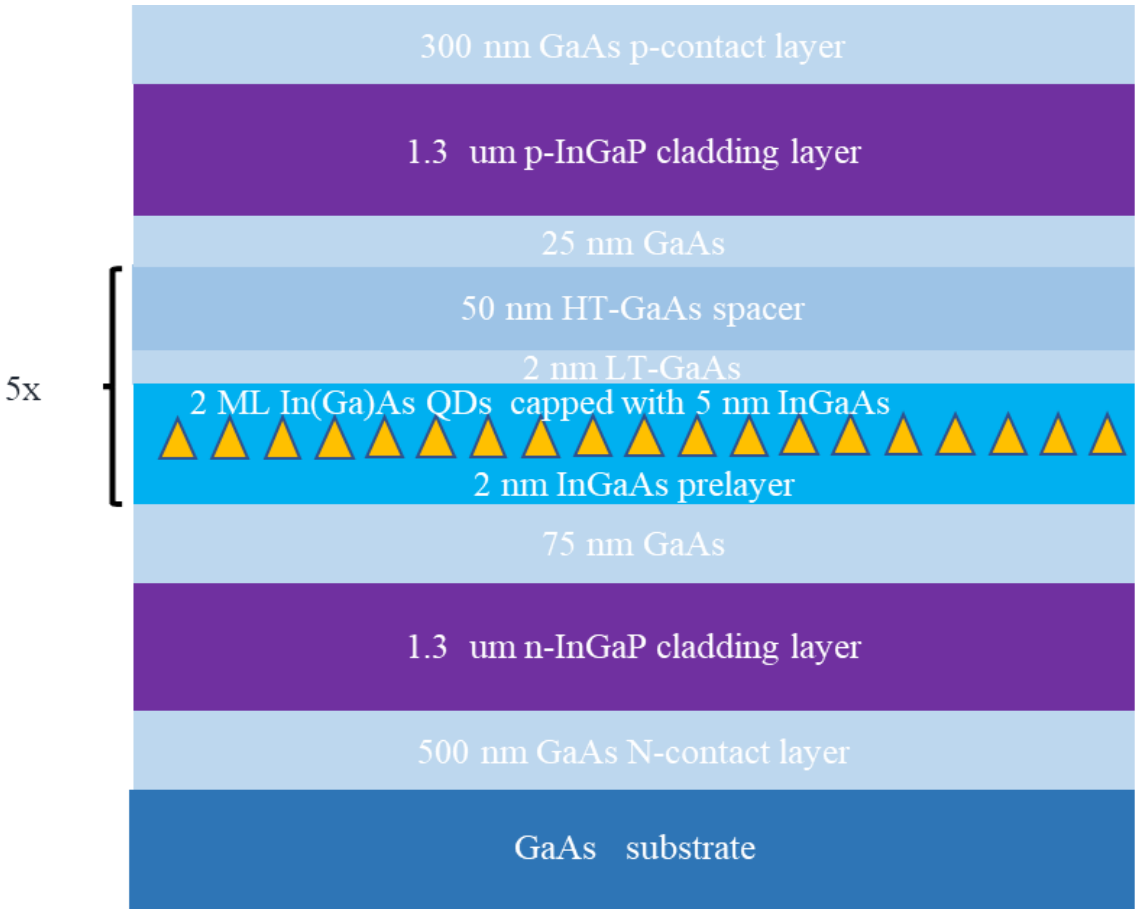

Figure 3.1. Material structure of full laser growth.

Here, I_{th} is the threshold current; T is the temperature; T_0 is the characteristic temperature.

3.3 Quantum dot laser structure layer stack design

Quantum dot laser has QD as the gain medium in the active region, as described in the previous chapter. The complete laser layer stack is shown in Fig. 3.1. The complete QD laser material is grown by a horizontal reactor MOCVD system on a (001) semi-insulating GaAs wafer. The active region contains five layers of undoped dots-in-a-well (DWELL) structure. Two 75-nm-GaAs layers surrounding the active region are the separate confinement heterostructure layers. The cladding layer is chosen InGaP, and the thickness of the InGaP cladding layer is 1.3

μm for both the top cladding layer and the bottom cladding layer. The 1.3 μm thickness is chosen to ensure enough separation between the QD active region and the GaAs top contact and bottom contact. Therefore, this ensures enough optical confinement factor for the active region.

Compared with the most reported QD laser structure, the most distinguished character is the InGaP material for the cladding layers, rather than AlGaAs, which is widely used as the cladding layer for MBE-grown QD laser. Nevertheless, AlGaAs usually requires high growth temperature (typically well above 700 °C) by MOCVD [99–101], and such a high growth temperature will result in a strong blueshift of QD emission [102]. Conversely, GaAs lattice matched InGaP, with a suitable refractive index and bandgap, can be grown by MOCVD below 580 °C to replace AlGaAs as the cladding layer [103]. Besides, InGaP/GaAs material system also has the advantage over the AlGaAs/GaAs by avoiding aluminum oxidation during fabrication so that regrowth is applicable to form buried gratings for DFB lasers or more advanced photonic integrated circuit structures, which would boost the application of QD lasers in data communication.

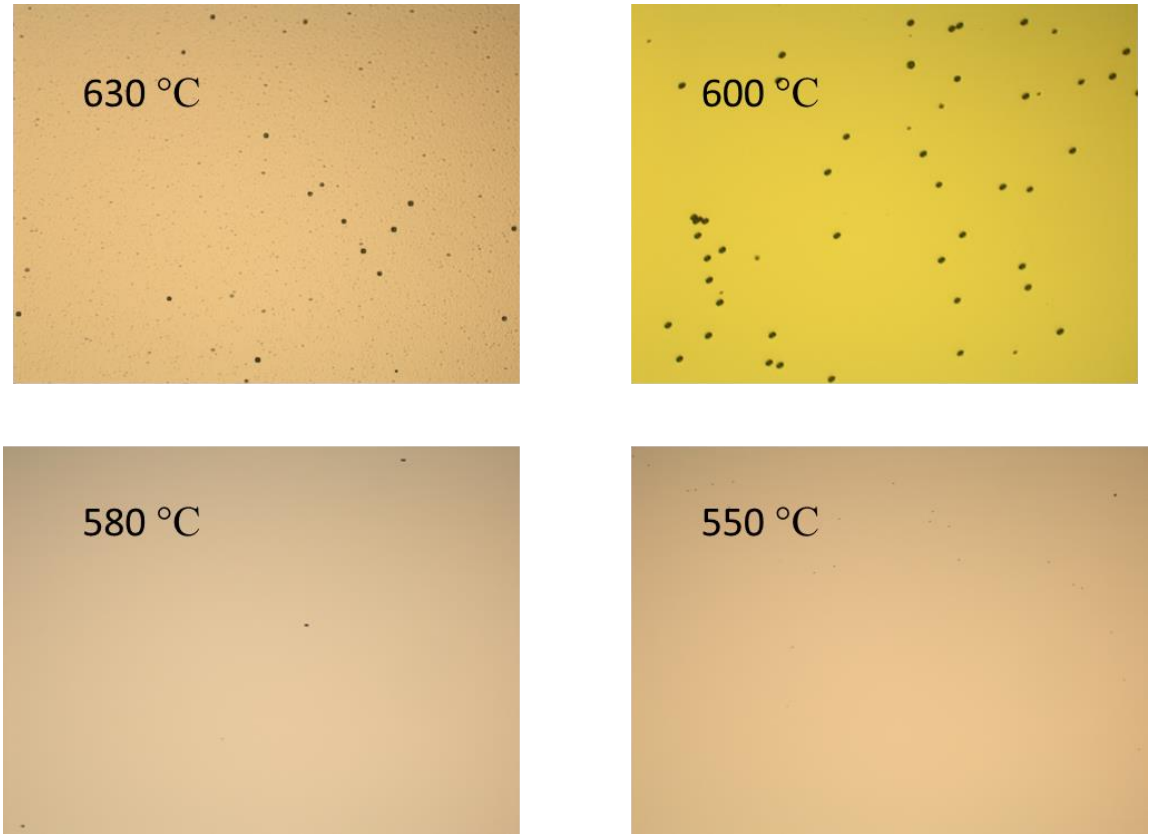

Figure 3.2. Optical microscope shown the influence of temperature on the surface quality of 1 μm thick InGaP grown on GaAs wafer by MOCVD.

3.4 MOCVD growth of InGaP cladding layer

Avoiding the phase separation phenomenon for MOCVD growth of thick InGaP is not trivial [104–106]. This results in composition fluctuation and clusters at the surface, increasing surface roughness. Following systematic calibration growths, we have found that the growth temperature is critical for avoiding phase separation, as shown in Fig. 3.2. We found that the high quality of the thick InGaP layer is only favored at low temperature (below 580 °C). At high temperatures

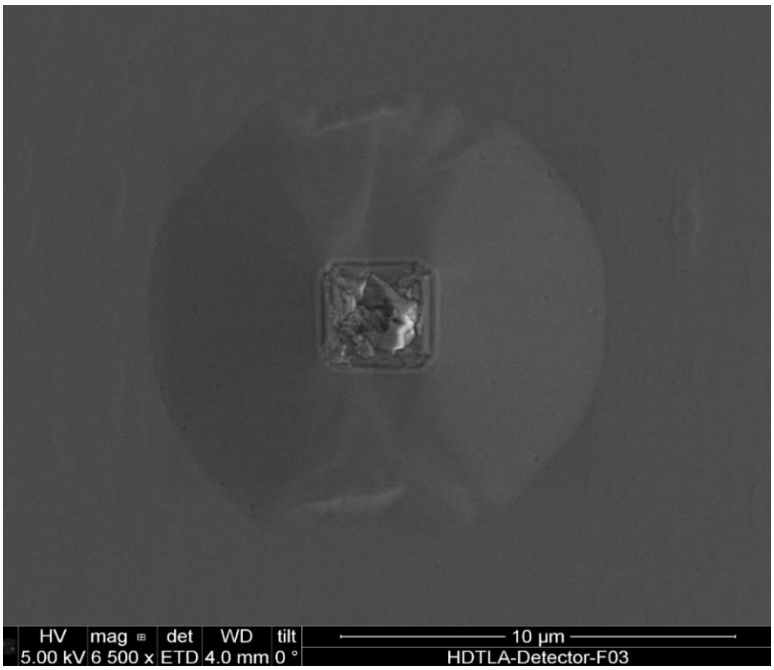

Figure 3.3. TEM top view of the surface morphology of the defects caused by InGaP phase separation.

above 600 °C, we find many optical defects on the surface due to phase separation in the InGaP.

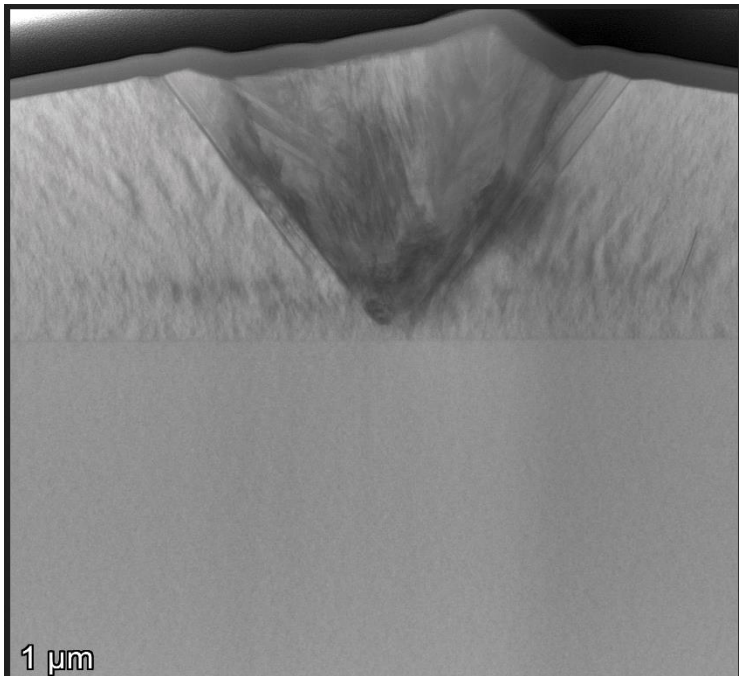

Figure 3.4. TEM cross section of the defects caused by InGaP phase separation.

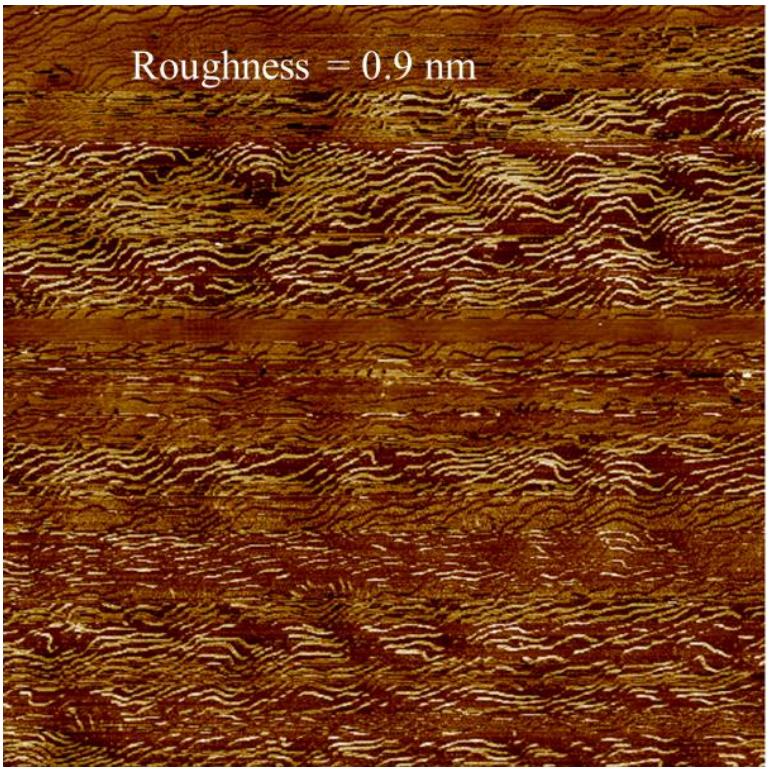

Figure 3.5 AFM image of surface of 1.3 μm InGaP grown on GaAs wafer under 580 °C. The low roughness and the clear atomic step layer indicate high material quality.

Transmission electron microscopy (TEM) image shows the surface defects morphology caused by phase separation in InGaP in Fig. 3.3. The cross-section of the InGaP phase separation is shown in Fig. 3.4, in which the contrast of the image shows apparent indium composition variation.

High quality of thick InGaP grown on GaAs wafers has been demonstrated under low temperatures. The clear atomic layer step in the AFM image indicates the high quality of material growth, and the surface roughness is just 0.9 nm for 1.3 μm InGaP grown under 580 °C.

3.5 Suppression of InGaP phase separation due to V-shaped defects in QD

In the previous section, InGaP phase separation phenomena is mainly researched on the influence of the growth temperature. The experiment results reveal that a low growth temperature is critical in suppressing phase separation. However, in developing the complete laser material growth structure, we found that severe InGaP phase separation can occur for the top cladding layer even under growth conditions that could well suppress the phase separation in InGaP on GaAs calibration growth. The V-shape defects generated in the QD active region can result in InGaP phase separation, as shown in the following TEM image. From this TEM image,

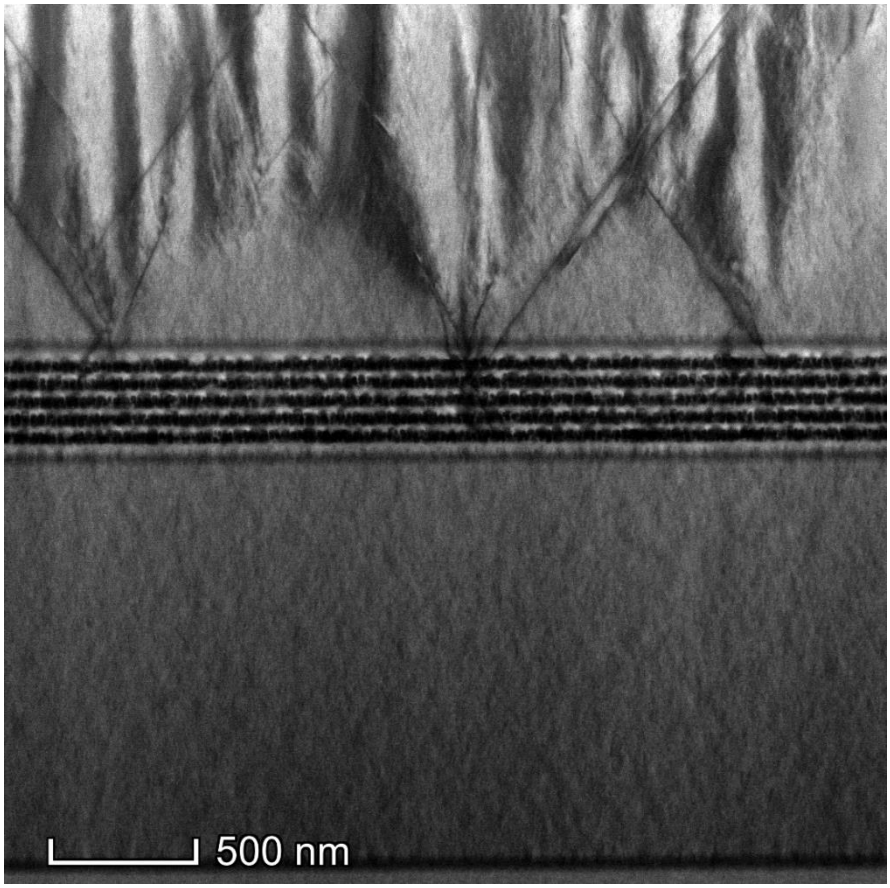

Figure 3.6. TEM cross-section image shows InGaP phase separation caused by V-shape generated in the QD active region.

the distance between two V-shape defects is just several hundred nanometers, indicating a high density of defects. The surface of this sample after upper InGaP cladding layer growth shows a highly rough surface and a significant number of large surface defects. Suppressing the V-shape defects in the QD active region is essential to obtain high epitaxial layer quality for laser material growth.

V-shape defects are a type of crystalline defects that can occur during the growth of InAs QDs. These defects have a "V" shape and can significantly impact the electronic and optical properties of the QDs, such as altering their absorption and emission spectra, reducing their quantum efficiency, and perturbing the electron energy level structure. The formation of V-shape defects in InAs QDs can be attributed to the excessive strain induced by InAs QDs [107]. A cross-section TEM of the V-shape defect is shown in Fig. 3.7. This QD active region contains five layers of QDs, and the V-shape defect typically generates in the third or latter layer. The V-

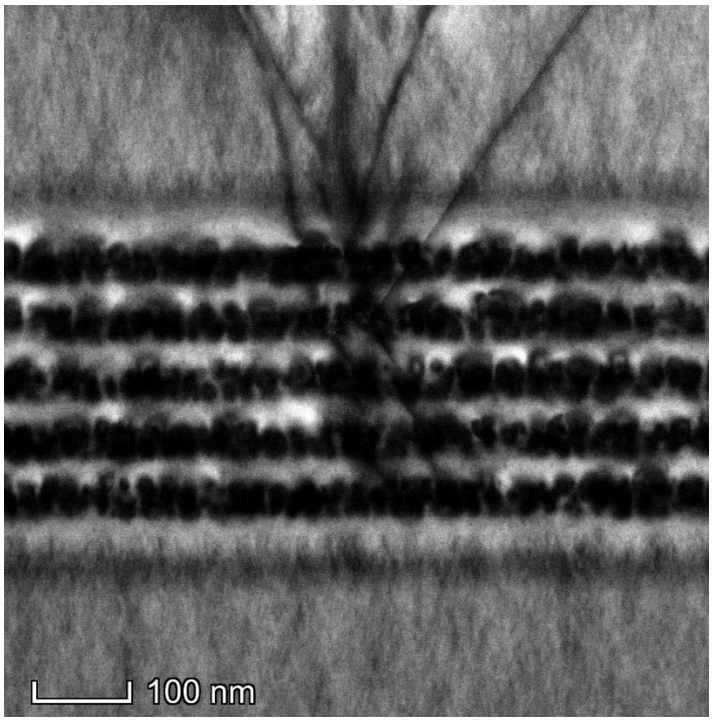

Figure 3.7. Cross-section TEM of the V-shape defects in the QD active region.

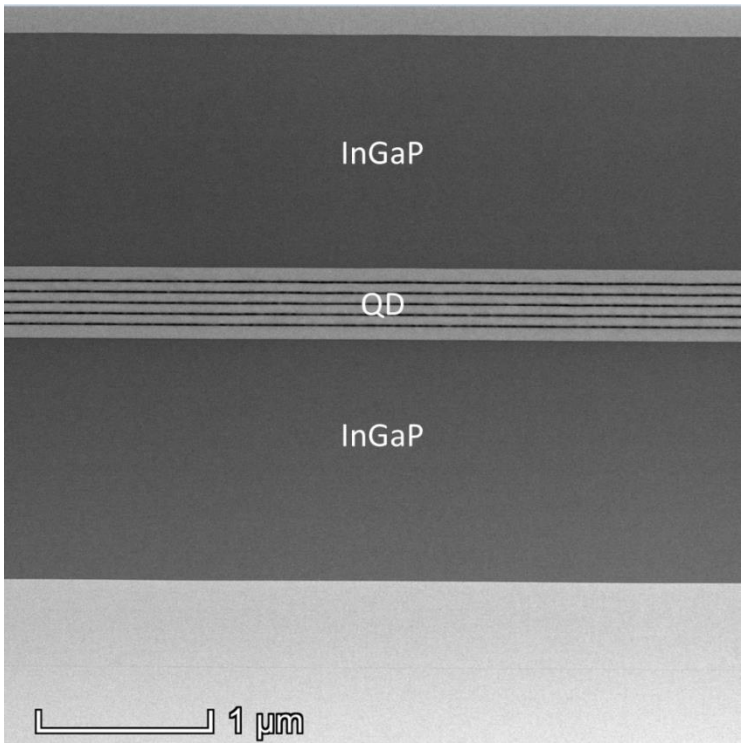

Figure 3.8. TEM shows that the V-shaped defects generation and InGaP phase separation is suppressed.

shape defect compromises several stacking faults and threading dislocations. The contrast in the TEM image indicates that the strain is much more muscular in the region near the V-shape defect. All these indicate the generation of V-shape defects resulting from a high strain accumulation due to QD, especially after stacking three layers. According to these, decreasing the strain induced by the QD is essential to minimize the generation of V-shaped defects. As a result, we decrease the coverage of the InAs QD deposition amount from 3 ML to 2.6 ML, and the generation of V-shape defects is significantly suppressed.

3.6 Whole laser structure growth and material characterization

Another point of consideration for whole laser structure growth is the temperature for the upper cladding layers. The InGaP is optimized at 580 °C and has demonstrated low surface

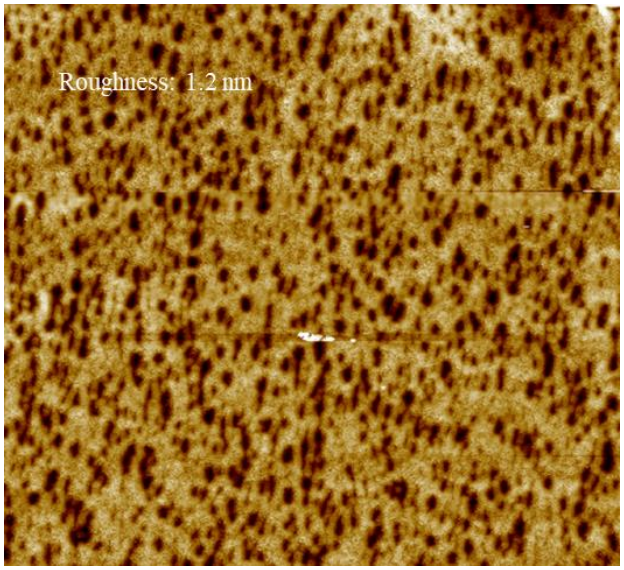

Figure 3.9. A 1 μm × 1 μm AFM scanning of the surface of 1.3 μm thick InGaP grown on GaAs under 550 °C.

roughness. However, such a high-growth temperature cannot apply to the upper cladding layer

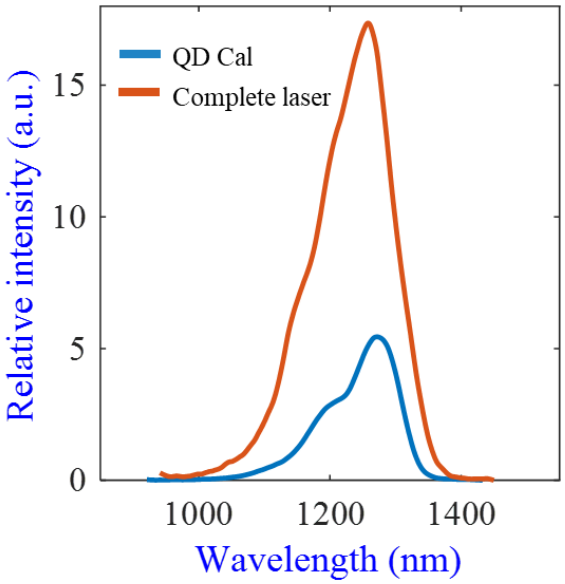

Figure 3.10. PL characterization of the whole laser structure material and a QD calibration structure.

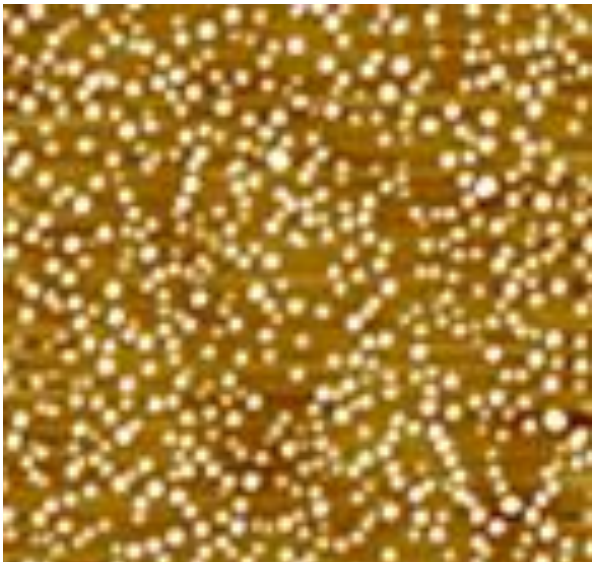

Figure 3.11. A 1 μm × 1 μm AFM scanning of the single-layer QD calibration growth.

because it will anneal the QDs during the growth of the upper cladding layer. As a result, the QDs in the active region will transform, and the emission wavelength will show an apparent blue shift. Low temperature (below 580 °C) growth upper cladding layer is essential for high QD laser performance. 1.3 μm thick InGaP calibration growth under 550 °has been conducted, and a

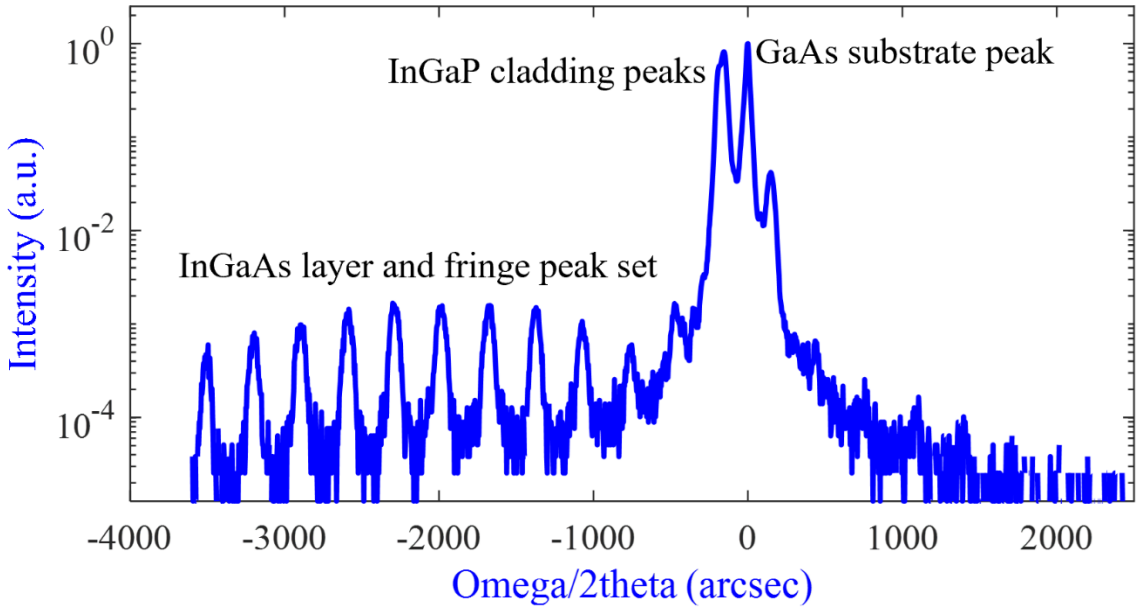

Figure 3.12. XRD characterization of the whole laser structure.

1 μm × 1 μm AFM scanning was performed to show a surface roughness of about 1.2 nm, illustrated in Fig. 3.9. The roughness is slightly higher than InGaP grown under 580 °C but is still low enough for the following GaAs contact growth and fabrication.

The whole laser stack structure is shown in Fig. 3.1. Room temperature PL spectra are performed to characterize the laser material as shown in Fig. 3.10. The active region contains five layers of QDs. The intensity of the peak of the whole laser material is about three times that of a single QD layer calibration structure. The peak wavelength of the whole laser structure also has a slight blue shift due to the additional inhomogeneity of QD size from the stacking of multi-layer of QDs. The QD growth condition in the whole laser material structure is the same as the single-layer QD calibration structure, which shows highly uniform QDs from the AFM image in Fig. 3.11, and the density of QD is about 5.5E10 cm^{-2}. XRD was conducted to characterize the whole laser structure, illustrated in Fig. 3.12. Clear InGaP peaks and the set of InGaAs/GaAs multi-layer peaks confirm excellent material quality.

3.7 Fabrication of QD lasers

The MOCVD-grown QD laser material was fabricated into Fabry-Perot (FP) cavity lasers with deep-etched ridge structures. Co-planar n- and p- contact structure was chosen for the convenience of metrology. The whole process flow is shown in Fig. 3.13.

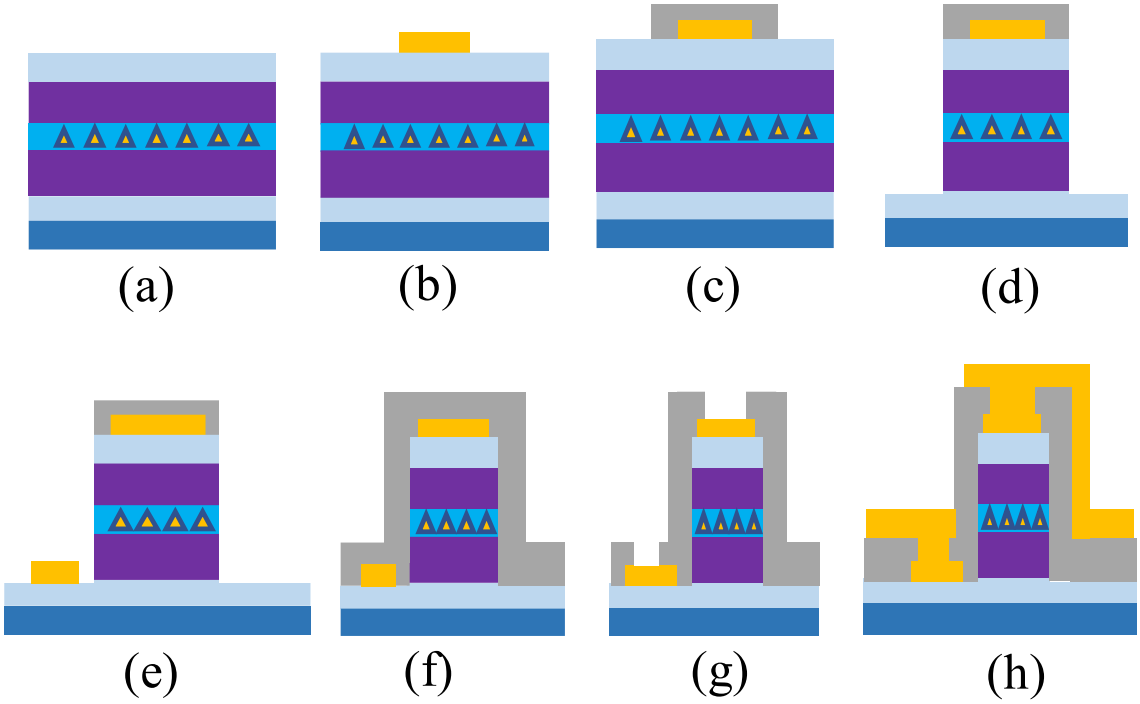

Figure 3.13 Fabrication process flow for the FP cavity laser diodes.

A metal layer stack of Ti/Pt/Au was first deposited on the top by the lift-off process to form strips by Electron Beam Evaporation as the p- contact metal. Fig. 3.14 shows the sample surface

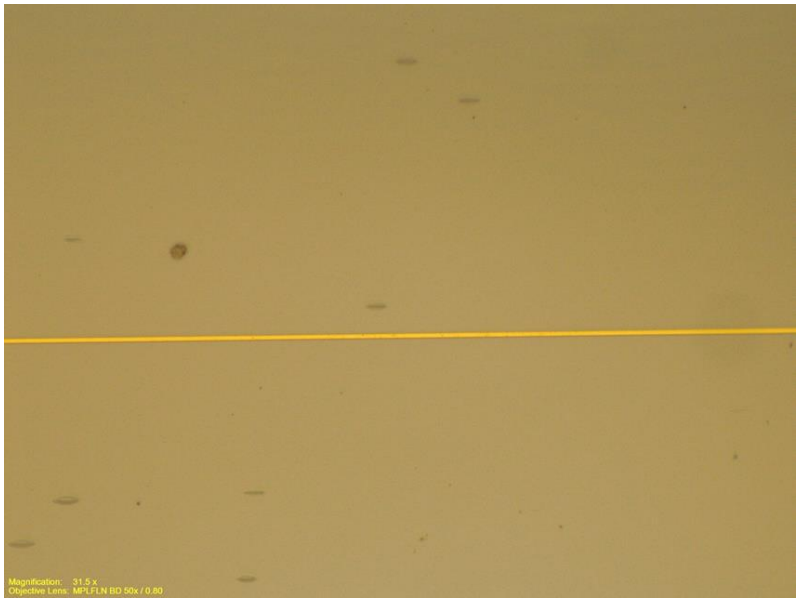

Figure 3.14 Optical microscope of the sample after p-contact metal lift-off process.

with the p-contact metal strip. Then, the surface was passivated by silicon nitride (SiN) and silicon dioxide (SiO_2) dielectric layer stack. SiN was first deposited because of its excellent adhesion properties, and the SiO_2 is utilized as the hard mask for the following dry etching step. The hard mask was patterned by optical lithography and Inductively Coupled Plasma (ICP) etching with the etchants of CF_4 and CHF_3. The hard mask should be in a strip structure and broader than the p-contact metal to ensure the metal is fully covered. This is critical since any exposed metal will be sputtered and cause rough semiconductor etching in the dry etching step of the ridge.

After the hard mask definition, the sample was put into an ICP chamber for ridge etch. The etchants of ICP dry etching of semiconductor material contain Cl_2, H_2, and Ar. The Cl_2 can have both chemical and physical interaction with the semiconductor, and the Ar can provide additional

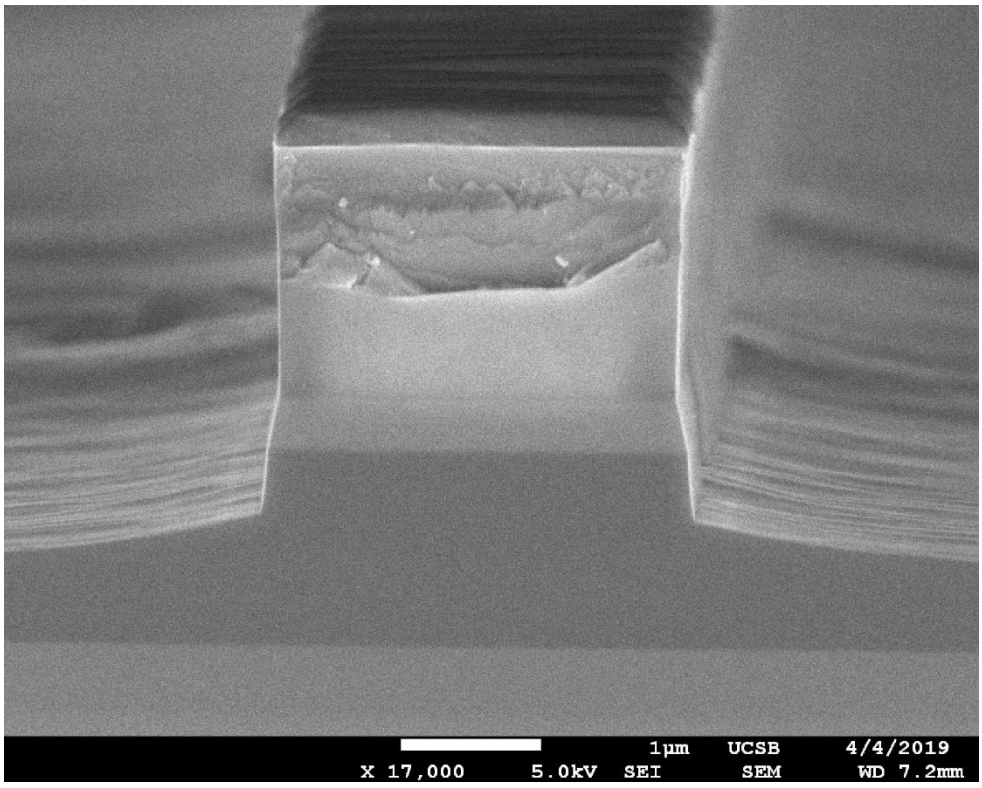

Figure 3.15 The cross-section SEM image of the ridge after ICP etching.

physical etching to balance the total chemical and physical etching effect to generate a smooth etching field and sidewall. The effect of H_2 is the passivation gas, which can ensure a vertical sidewall after etching. A critical parameter of this etching is the temperature. The cladding layer of this laser structure is InGaP, and the product of the etching of InGaP by Cl_2 (Indium Chloride) is in a solid state at room temperature, which can significantly increase the roughness of the field and the sidewall roughness. Therefore, the etching has to be conducted under a high temperature (200 °C) in our experiment. Fig. 3.15 shows a smooth sidewall of the ridge after the ICP etching.

(a) Before HCl wet etching

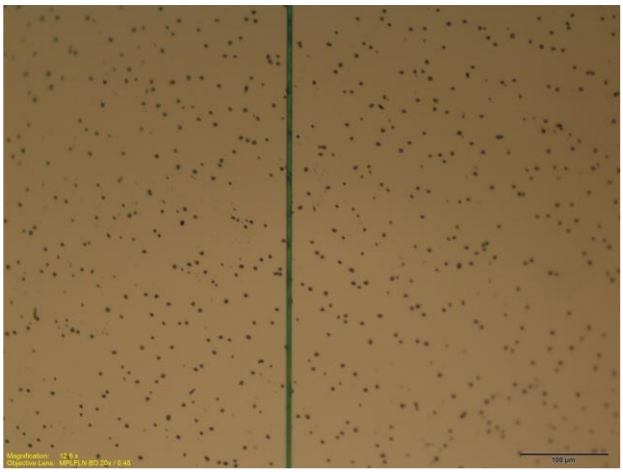

(b) After HCl wet etching

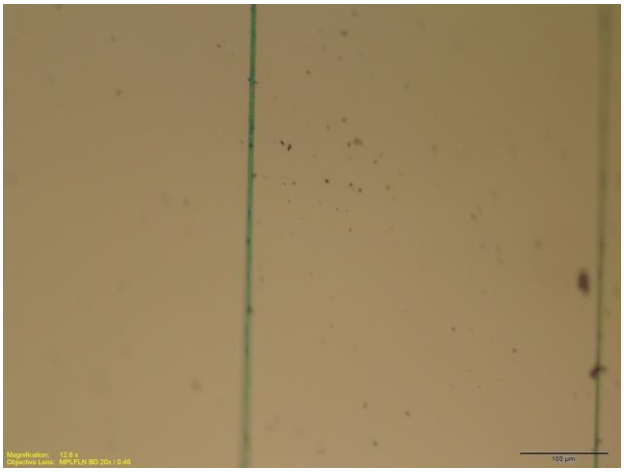

Figure 3.16 Sample Field surface before (a) and after (b) HCl wet etching.

The kink at the interface between the InGaP cladding layer and the QD active region is due to the different chemical etching properties between InGaP and GaAs. After the ICP dry etching, selective wet etching is required to etch the residual InGaP further and ensure termination at the surface-GaAs contact layer. Hydrochloric acid was chosen as the etchant because of its high etching selectivity on InGaP over GaAs. Prior to the wet etching, a photoresist was defined to cover the ridge by a lithography process to protect the ridge sidewall. The selective wet etching brings the additional benefit of polishing the field surface, which favors ohmic contact formation for the n-contact. Fig. 3.16 shows the sample surface before and after HCl wet etching. The bumps induced by surface defects after etching were effectively removed.

Then the n-contact metal was deposited with the Ni/AuGe/Ni/Au layer stack by electron beam evaporation. A rapid thermal annealing process was performed to form an ohmic contact. After that, the surface is passivated by multi-dielectric layers. 4 nm thick Al_2O_3 and 20 nm SiO_2 were first deposited in atomic layer deposition (ALD). The reason for utilizing ALD is to ensure

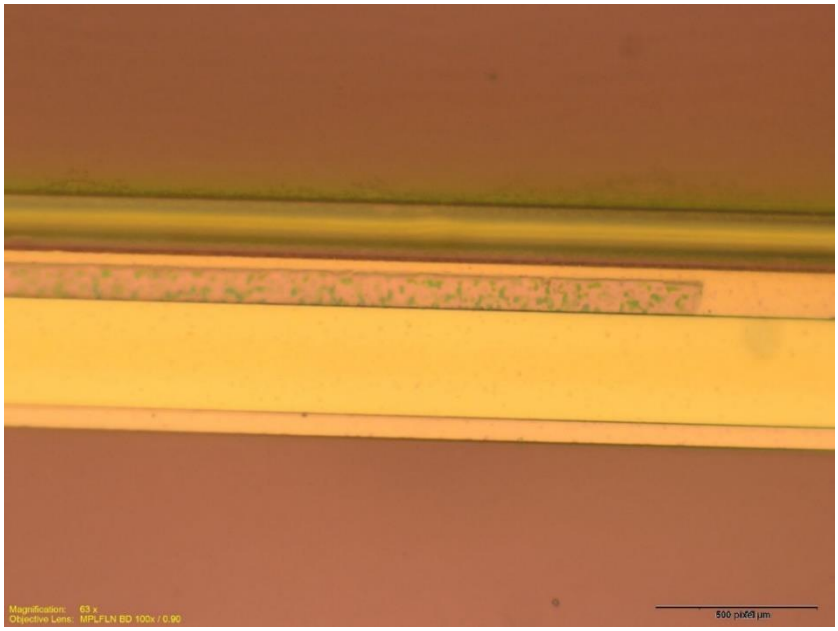

Figure 3.17. Current injection via opened on the n-contact metal and ridge.

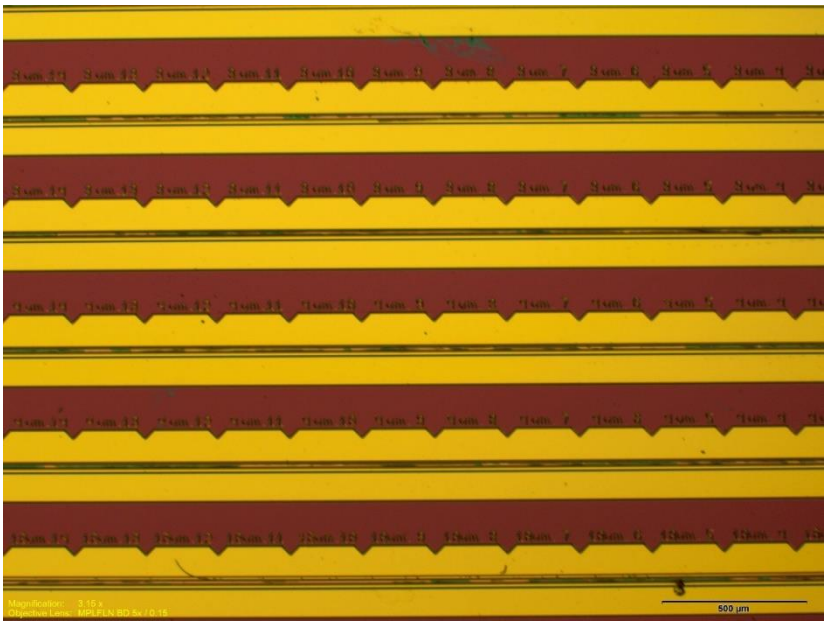

Figure 3.18. Probe metal pad formed on the sample surface.

excellent sidewall coverage. Then, alternative silicon nitride and silicon oxide layer stacks were deposited with a total thickness of 400 nm. The alternative dielectric layer structure is for stress compensation to avoid cracking. After the surface passivation, the current injection window was opened to expose the n- and p- contact metal, as shown in Fig. 3.17. Then, a thick Ti/Au layer stack was deposited by a lift-off process to form the probe pad, illustrated in Fig. 3.18. Then the

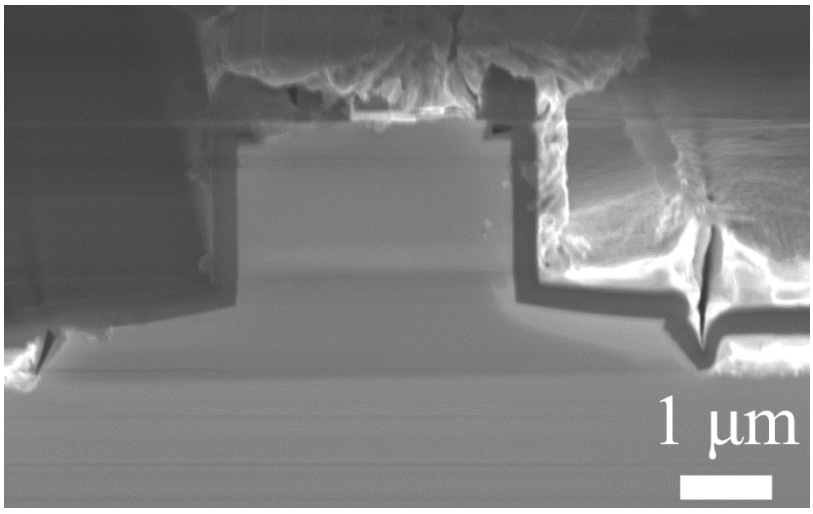

Figure 3.19. Cross-section of the SEM image of laser facet after cleaving.

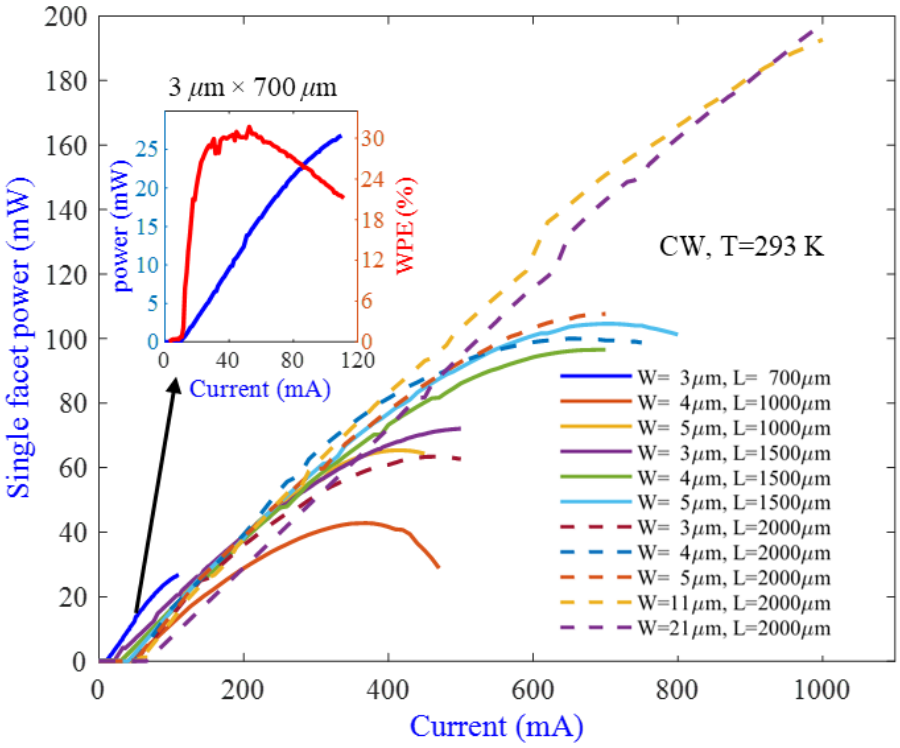

Figure 3.20. LIV curve of Fabry-Perot lasers with various widths and lengths

sample was thinned down to 100 μm. The sample was finally cleaved into different lengths of laser bars. Fig. 3.19 shows an SEM cross-section of the laser facet.

3.8 QD laser device performance

Continuous wave (CW) operation and room temperature characterization were conducted by mounting the laser bars on ceramic (AlN) carriers. The light-current-voltage (LIV) curves were measured for different dimensions for Fabry-Perot (FP) lasers. There is no facet coating applied to the FP lasers. The broad-area lasers (11 μm or 21 μm wide) show a high output power of about 200 mW. The maximum power can be higher because the maximum injection current is just 1 A for the current source. The threshold current of the 21 μm × 2 mm laser is about 67 mA, indicating a threshold current density of 160 A/cm^{-2}. Besides, the short narrow-ridge laser with a

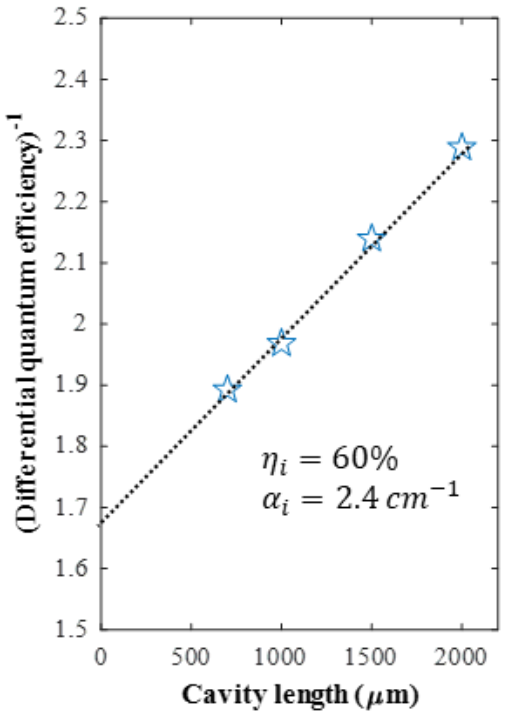

Figure 3.21. Reciprocal of measured differential efficiency versus cavity length.

dimension of 3 μm × 700 μm shows an excellent wall-plug efficiency (WPE) with the LIV in the

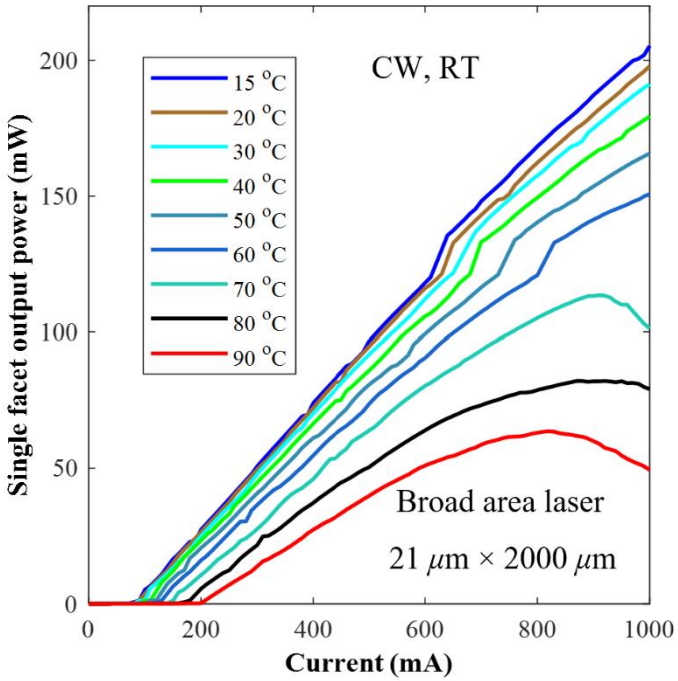

Figure 3.22. LIV curve of the broad area laser at different temperatures.

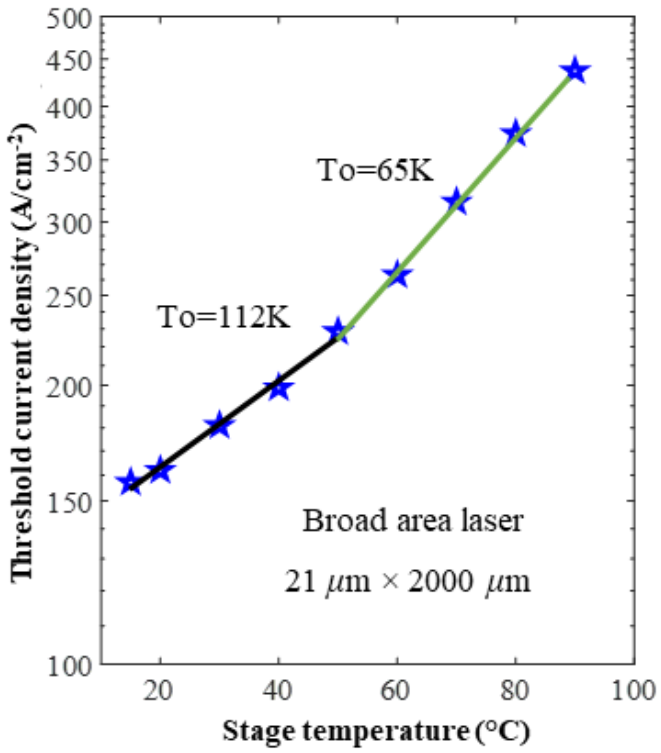

Figure 3.23. The threshold current density of the broad area laser measured under different stage temperature.

inset of Fig. 3.20. This narrow-ridge laser shows a low threshold current, just eight mA, and a high maximum WPE about 30%.

QD lasers with different cavity lengths were made (the ridge width is 3 μm) and measured the differential efficiency. According to Eq. 3.12, the injection efficiency and the internal optical loss are about 60% and 2.4 cm^{-1}, respectively, in Fig. 3.21.

The thermal performance of the broad area laser with a dimension of 21 μm × 2000 μm was characterized. The LIV curves were measured at different temperatures from 20 °C to 90 °C. The QD laser still performs well with an output power of about 50 mW at 90 °C, where the setup limits the maximum measurement temperature. The threshold current at different temperatures is

shown in Fig. 3.23. The characteristic temperature is about 112 K from room temperature to 50 °C and is about 65 K from 50 °C to 90 °C.

3.9 The lifetime of QD laser

Lifetime is a critical metric to justify practical applications for QD lasers. Here we performed an aging test for two QD lasers in the same dimension of 3 μm × 2000 μm under 30 °C and 60 °C, respectively. The threshold current was monitored every fifty hours, and the total aging time was 1600 hours. One widely accepted definition of semiconductor lasers is the length of time

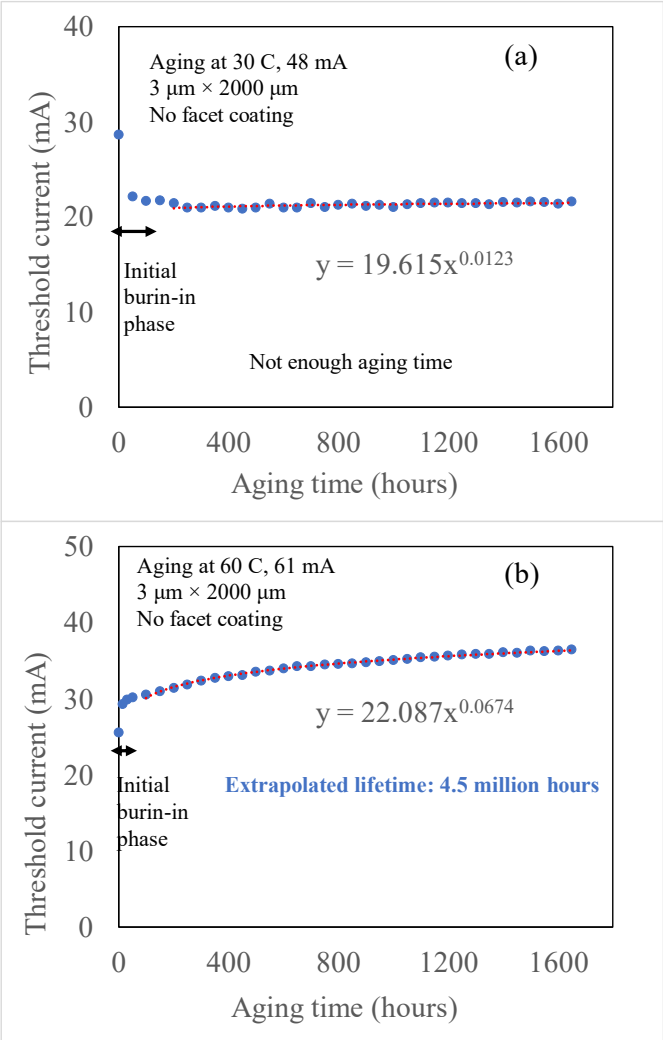

Figure 3.24. Aging test of the two QD lasers under two different temperatures.

that the threshold current doubles. The relationship between threshold current and the aging time follows the power law formula. The threshold current of the device aging at 30 °C decreases at the initial burn-in phase and becomes stable over the whole aging time of 1600 hours. This indicates a significantly high lifetime, which cannot be extracted from the current data by the power-law formula; The device aging at 60 °C shows a dramatic increase in the threshold current, and then the threshold current follows a power-law formula relationship with the aging time. The extracted lifetime at 60 °C is about 4.5 million hours.

In this thesis, the QD laser on GaAs has demonstrated high wall-plug efficiency of about 30%, which is compatible with the state-of-the-art QD laser performance for uncoated Fabry-Perot cavity laser [108,109]. Applying facet coating should bring higher wall-plug efficiency and lower threshold current density. The injection efficiency is relatively low (60%), and the reason might be that the carrier confinement (especially for the hole) is not enough for the InGaP cladding layer because of the relatively small bandgap offset between InGaP and GaAs for the valence band. What should be highlighted is that this is the first report of a high lifetime of MOCVD-grown QD laser at a high temperature.

Chapter 4

MOCVD-grown QD laser on Si for laser integration

4.1 Review of laser integration on Si

Silicon photonics is to integrate different functional optical components on the Si platform to manipulate light to transmit information at high speeds and over long distances. However, due to the indirect band structure of Si, it is not a suitable platform for forming light sources such as lasers [110,111]. Integrating lasers with silicon photonics allows for a more compact, efficient, and cost-effective solution for optical communications [112–114], sensing [115–118], and other applications [119]. There are generally four categories of laser integration for silicon photonics: discrete laser device integration, hybrid laser integration, heterogenous laser integration, and direct hetero-epitaxy.

Discrete laser integration involves assembling discrete laser diodes and silicon photonic chips, which are mounted on separate platforms before assembling them [120], as shown in Fig. 4.1. The achievement of high coupling efficiency relies on alignment controlling. It requires specific coupler designs on the silicon photonic chip, such as edge couplers or surface grating couplers [121]. Besides, other optical components such as collimation lenses and isolators could also be added between the laser diodes and si photonic chips. Discrete laser integration is the most straightforward method and has the advantage of pre-validation of the laser device to achieve high yield and performance. However, the disadvantage of discrete laser integration is the expensive and time-consuming process of assembling, which prevents the scaling up of Si photonics manufacturing and weaken the cost advantage of Si photonics.

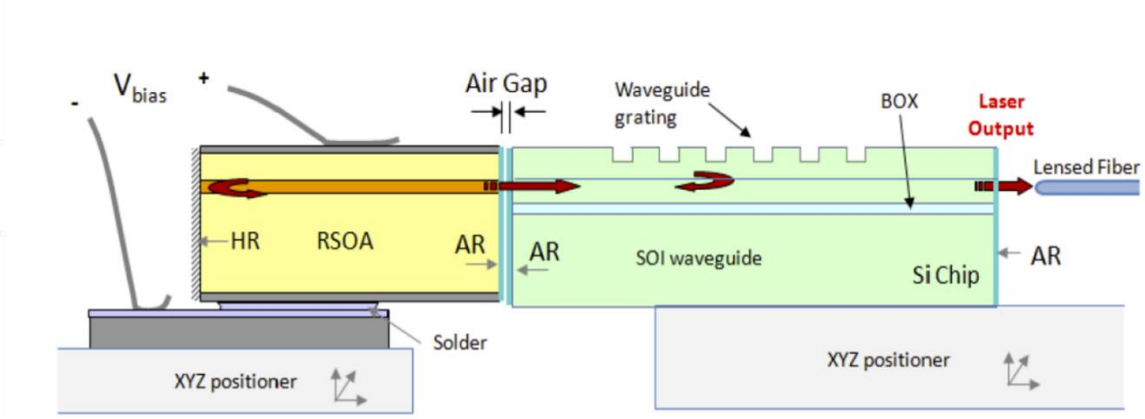

Figure 4.1. The diagram of discrete laser integration, where the semiconductor lasers and the photonic integrated circuits are mounted on different submout [120].

Hybrid integration can integrate fully processed III-V devices, such as laser chips, into silicon and silicon nitride PICs [121–125]. The processed laser diode chips can be placed either adjacent to the PIC or directly on the surface of the PIC. The benefit of using this integration technique is the ability to test and describe the device before beginning the integration process, just as discrete integration. This boosts yield and makes it possible to tighten performance management by enabling the selection of the best-performing devices and the discarding of non-functional components. Because the photonic components that must be integrated into the photonic circuit can be chosen individually, hybrid integration is also particularly appealing for small-scale production and custom circuits. The assembly for the hybrid integration approach is often large, a drawback of hybrid integration. The serial alignment and integration of photonic devices, which involves one or more devices at a time, can be laborious and therefore have low throughput. This lessens the appeal of this technique for PIC chips in very high volumes (such as might be required for low-cost mass-market consumer electronics) compared to other methods,

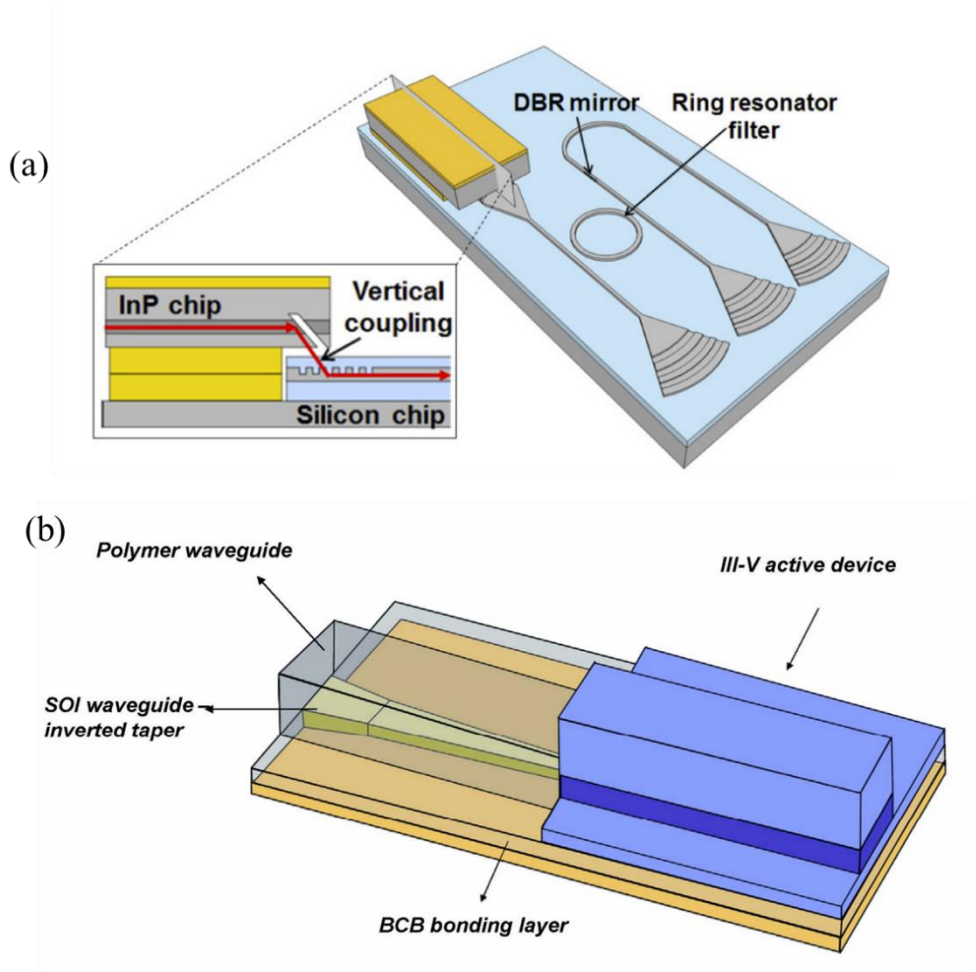

Figure 4.2. Diagram of the concept of hybrid integration, where the die of semiconductor laser is placed on the top of photonic integrated circuits. The coupler can be (a) grating coupler and (b) edge coupler [125].

such as heterogeneous integration. Due to the relatively poor heat conductivity of the buried oxide, this strategy not only consumes a sizable amount of on-chip space but also presents difficulties in cooling the III-V devices through the underlying silicon-on-insulator (SOI) substrate, due to the relatively poor heat conductivity of the buried oxide.

Heterogeneous integration integrates different material technologies into a single chip, usually during the early or middle stages of chip fabrication. This technique has been heavily researched, particularly for integrating III-V material into silicon or silicon nitride photonic

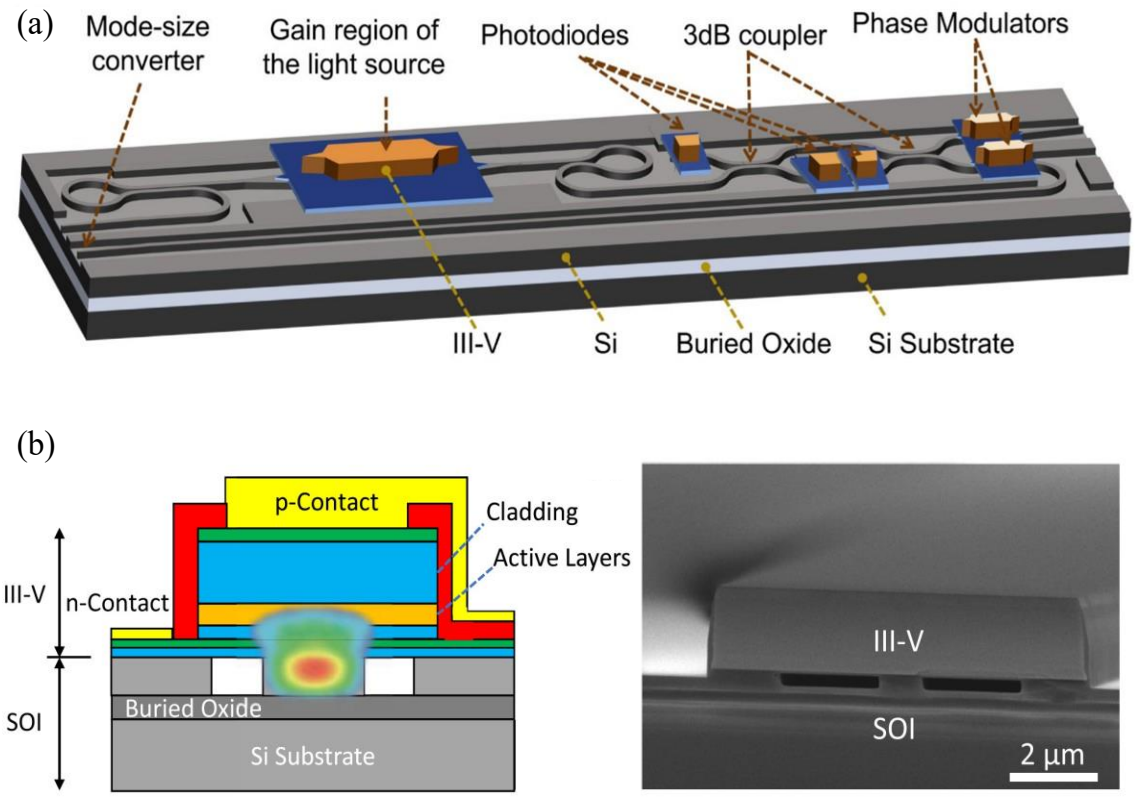

Figure 4.3. (a) Optical system based on photonic integrated circuit with heterogeneously integrated lasers [125]. (b) cross-section view of the heterogeneously integrated lasers [136].

integrated circuits [126–130]. When switching between various waveguide material technologies, heterogeneous integration offers advantages such as functionality similar to monolithic integration, resulting in high alignment accuracy and low losses. The process also ensures the reliable performance of the integrated photonic elements and is cost-effective due to the economy of scale, making it suitable for high-volume applications. However, heterogeneous integration requires ultra-clean and smooth surfaces, which can be challenging in university research facilities, although this is not an issue in semiconductor foundries. In addition, the die-

to-wafer bonding process used in heterogeneous integration does not allow for modular testing of

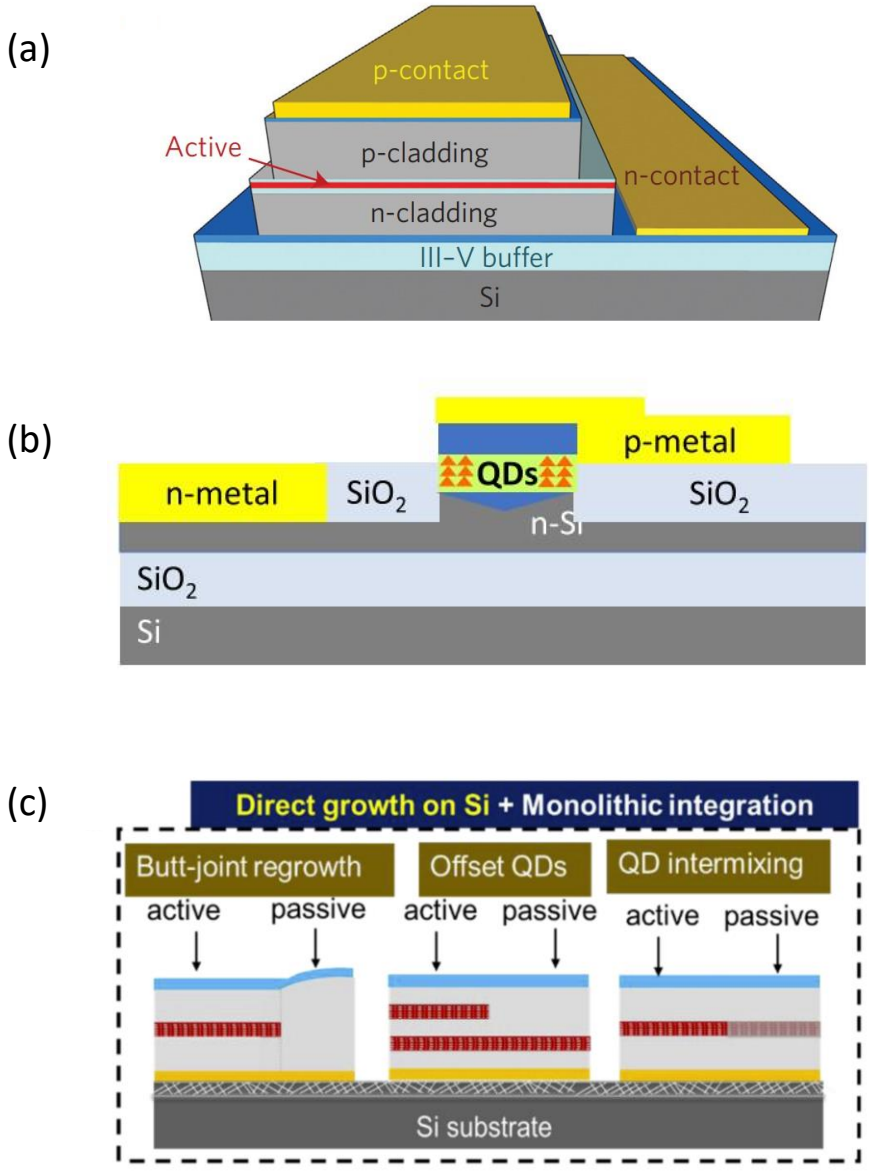

Figure 4.4 (a) diagram for direct epitaxy of III-V semiconductor lasers on Si wafer [137]; (b) the concept of selective grown of QD laser on SOI wafer and evanescent-wave coupling of the light into Si waveguide [131]; (c) the concept of direct epitaxy of III-V material on Si wafer and then achieve active-passive integration on the III-V platform to form comprehensive photonic integrated circuits [33].

individual components before integration into more complex PICs, and the process requires tight control to improve yield. Another challenge for heterogeneous integration is the size mismatch between the III-V material and the Si. For example, the III-V material wafer is regularly four inches or six inches for the current compound semiconductor foundry, while the Si wafer can be as large as twelve inches. This mismatch of wafer size between III-V and Si also decreases the yield of the usage of III-V material and the scalability of Si photonics manufacturing. Besides, the III-V substrate is regularly orders of magnitude more expensive than the Si substrate in the unit area, limiting the appeal of lost cost for heterogeneous integration.

To overcome the substrate size mismatch between Si and III-V, direct hetero-epitaxy of III-V on Si can probably be a promising solution. This method can provide monolithic laser sources on Si for laser integration and also take the benefit of CMOS manufacture for large-scale fabrication. Several technologies have been researched to suppress the generation of defects during the heteroepitaxy and apply defects-defensive active regions (QD), as shown in Fig. 4.4a [62,63,65]. In recent years, significant progress has been made in the performance of QD lasers on Si wafers. To form comprehensive photonic integrated circuits, selective growth can be conducted for the growth of QD laser on the top of SOI. The light can be coupled into the Si waveguide on the SOI platform through the evanescent wave, as shown in Fig. 4.4b [131]. Another way to form comprehensive photonic integrated circuits is to achieve active-passive integration by using the III-V on the Si platform to form every component, such as lasers, modulators, and detectors, as shown in Fig. 4.4c [33].

4.2 GaAs on Si template development

Semiconductor lasers formed by direct epitaxy of III-V on Si have historically underperformed compared to semiconductor lasers grown on their native substrates due to a high

density of defects generation during the epitaxy [131,132]. One of the reasons for this is the significant mismatch in the lattice constant of III-V materials. The lattice constant of silicon is approximately 5.43 Å, while the lattice constants of III-V materials are generally smaller, ranging from 3.26 Å for GaAs to 5.87 Å for InP. The second reason is the mismatch in their coefficients of thermal expansion. The thermal expansion coefficient of GaAs is approximately 5.8E-6 K^{-1}, while that of Si is approximately 2.6E-6 K^{-1}. This means that GaAs would expand two times more than Si when heated. Last, because GaAs are polar compounds while Group IV materials are nonpolar, this can lead to antiphase boundaries (APBs) forming when GaAs and Si material sublattices are misaligned, particularly across single atomic steps. Overcoming each of these mismatches is necessary to achieve good device performance.

4.2.1 V-groove on Si and GaP-on-Si growth to avoid APBs

Decades ago, the problem of antiphase boundaries (APBs) was mainly resolved by using miscut Si substrates that preferentially created double atomic steps on their surface. In the epitaxy of III-V materials on Si, Group V species always preferentially nucleate on the Si surface and terminate at one monolayer, which means that APBs only form at single atomic steps on the Si surface. Therefore, APBs are absent when there are no single steps present. However, miscut Si is incompatible with complementary metal-oxide-semiconductor (CMOS), which is highly desirable for photonic integration. The need for a CMOS-compatible Si substrate without APBs has recently driven research in III-V/Si epitaxy. APBs on CMOS-compatible Si substrate without miscut can be achieved by V-groove structure on Si or GaP-on-Si method because the double-layer atomic step can be formed in the nano trench of the V-groove structure or a high-temperature surface passivation step in the GaP-

on-Si formation process. In this thesis work, we have explored both methods and achieved high-quality (bare APBs) GaAs growth on Si.

The process of forming the V-groove structure was initiated by carving [110]-aligned nano-trenches with a 70 nm aperture and 60-nm-wide SiO_2 stripes on an on-axis Si (001) substrate through the use of patterning and dry-etching techniques. Subsequently, the wafer was dipped in 1% dilute hydrofluoric acid to get rid of the native oxide. After that, v-grooves were established using a 45% dilute potassium hydroxide (KOH) etching solution for 30 s, then plunged into a 10% hydrochloride (HCl) solution for 60 s to wipe out the KOH residuals. An HF dip was then applied to remove the oxide stripes [132]. A sketch depicting the resulting GaAs-on-V-groove patterned Si is shown in Fig. 4.5.

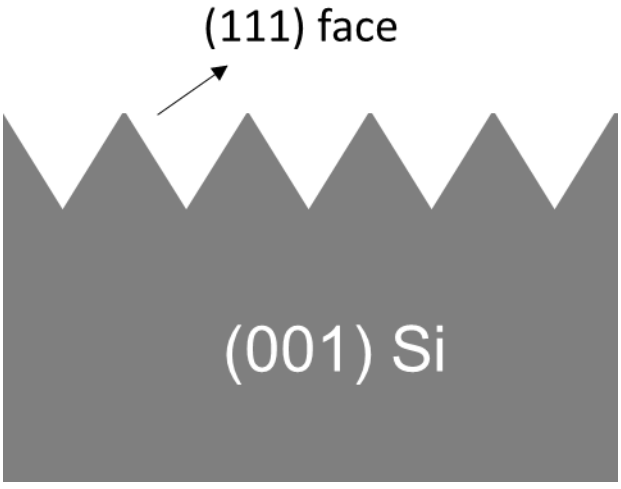

Figure 4.5. Structure of V-groove on Si

A simple one-step growth method was adopted to prevent the occurrence of planar

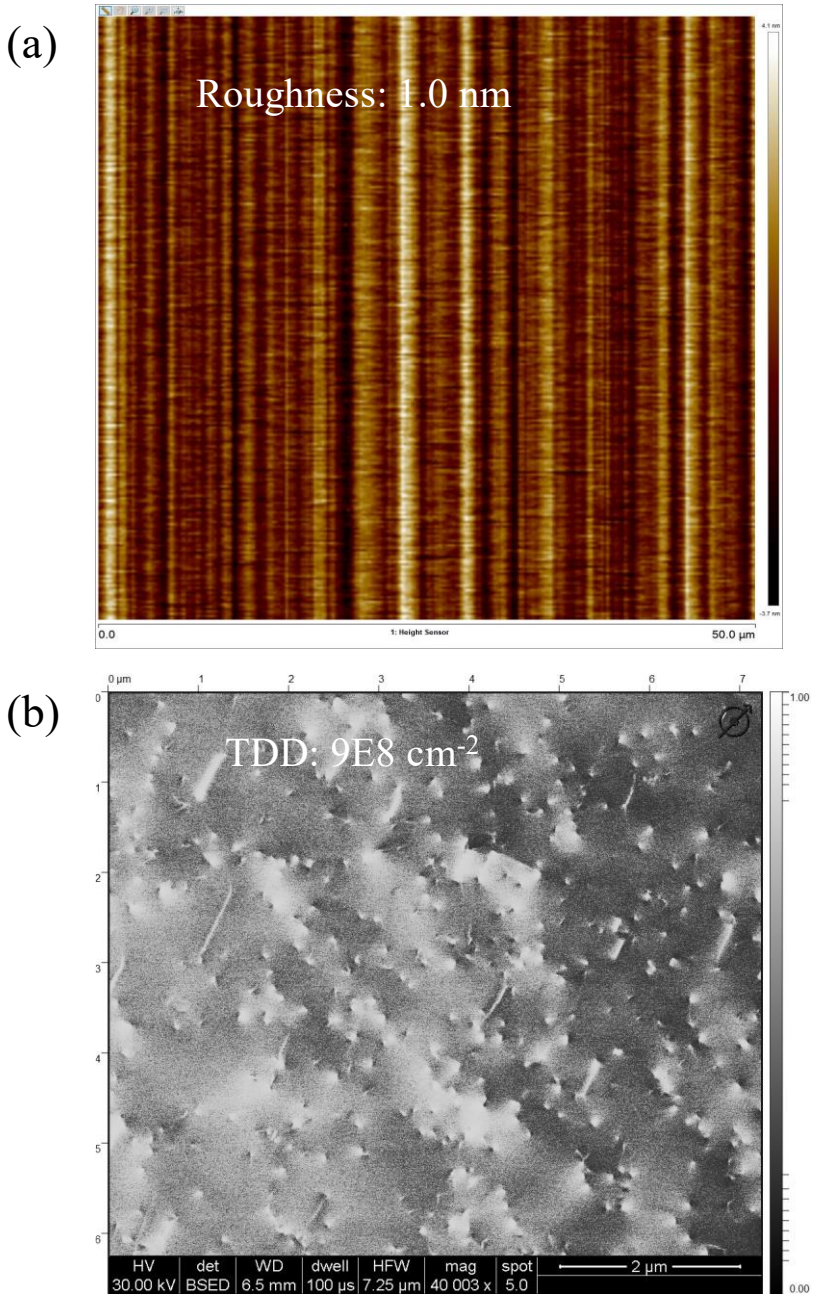

Figure 4.6. (a) A 50 x 50 µm² AFM scanning of the GoVS structure with 800 nm GaAs grown on Si, revealing a roughness of 1 nm. (b) a 7.25 x 7.25 µm² ECCI scanning of the surface of 800 nm GaAs GoVS sample and the TDD is about 4.7E8 cm^{-2}.

defects resulting from SiO2/GaAs interfaces, referring to the growth of GaAs layers at various temperatures in one run on the V-grooved Si. The material growth was performed under a pressure of 50 Torr, starting with annealing the V-grooved Si at 815 °C in an H_2 environment to desorb the native oxide. The reactor was subsequently cooled under arsenic overpressure for Si surface passivation. Next, a thin low-temperature (LT) GaAs wetting layer was grown at 400 °C, followed by a middle-temperature (MT) GaAs layer at 550 °C, and then a thick high-temperature (HT) GaAs buffer was grown at 630 °C. The surface morphology of the GaAs-on-V-groove-Si (GoVs) was evaluated using a 50 x 50 μm^2 atomic force microscopy (AFM) scan, as illustrated in Fig. 4.6(a). The surface roughness was significantly reduced using the one-step method, and most pinholes and pits were eliminated, resulting in a root-mean-square (RMS) value as low as 1 nm, as shown in Fig. 4.6(a). An electron channeling contrast imaging (ECCI) shows a threading dislocation density of about 9E8 cm^{-2}, as shown in Fig. 4.6(b). APBs generation has been well suppressed, indicated by the AFM and ECCI characterizations.

4.2.2 TDD reduction by thermal annealing cycle and strain layer superlattice

The lattice-constant mismatch between III-V semiconductors and Si substrates results in a buildup of stress in the first few pseudomorphic layers of material growth, leading to relaxation above a certain thickness. Misfit dislocations, which are lines of abnormal bonding at the interface, are formed, and they either terminate at the wafer's edge or turn up towards the growth interface to create threading dislocations (TDs). In areas where the distance to the sample edge is much greater than the distance to the epi surface, misfits tend to produce TDs. TDs contain trap states that act as nonradiative recombination centers, resulting in reduced device performance and lifetime due to recombination-enhanced dislocation climb. As a

result, III-V photonic devices grown on Si substrates generally have lower internal efficiencies and shorter lifetimes. Addressing TDs has been the primary focus of III-V/Si growth research.

Thermal cycle annealing (TCA) is a technique that can be used to reduce threading dislocations [33,131,132], involving heating and cooling the sample several times in a specific temperature range to promote the annihilation of threading dislocations. When the sample is heated, the atoms in the crystal lattice become more mobile, and dislocations can move and coalesce. When the sample is rapidly cooled, the dislocations are "frozen" in their new positions, and the defects are reduced. In this work, ten TCAs were conducted from 750 °C and 350 °C, which reduced TDD two-fold.

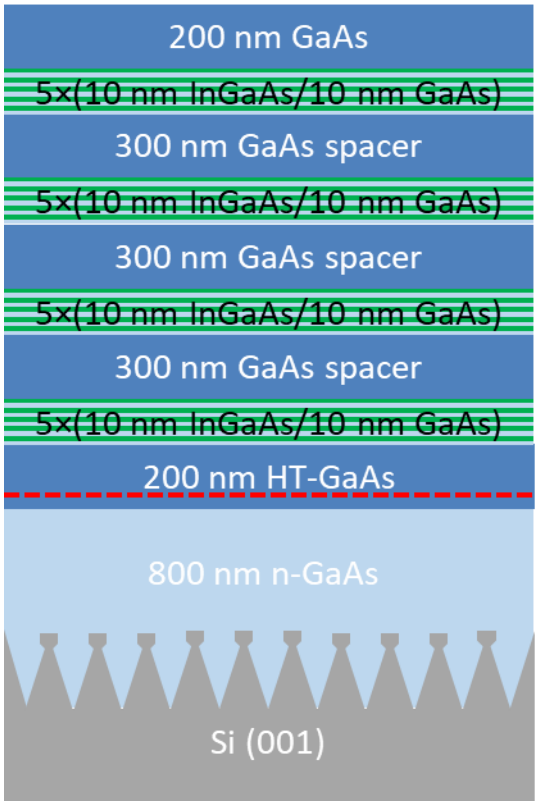

Figure 4.7. Schematic illustration of the whole layer stack of the GoVS.

Strain layer superlattice (SLS) is an effective dislocation filter in the hetero-epitaxy of GaAs on silicon (Si) [131,132]. SLS structures consist of alternating layers of strained and unstrained materials, resulting in a superlattice structure. InGaAs/GaAs are the typical alternating layers for the SLS dislocation filter for the hetero-epitaxy of GaAs on Si. The use

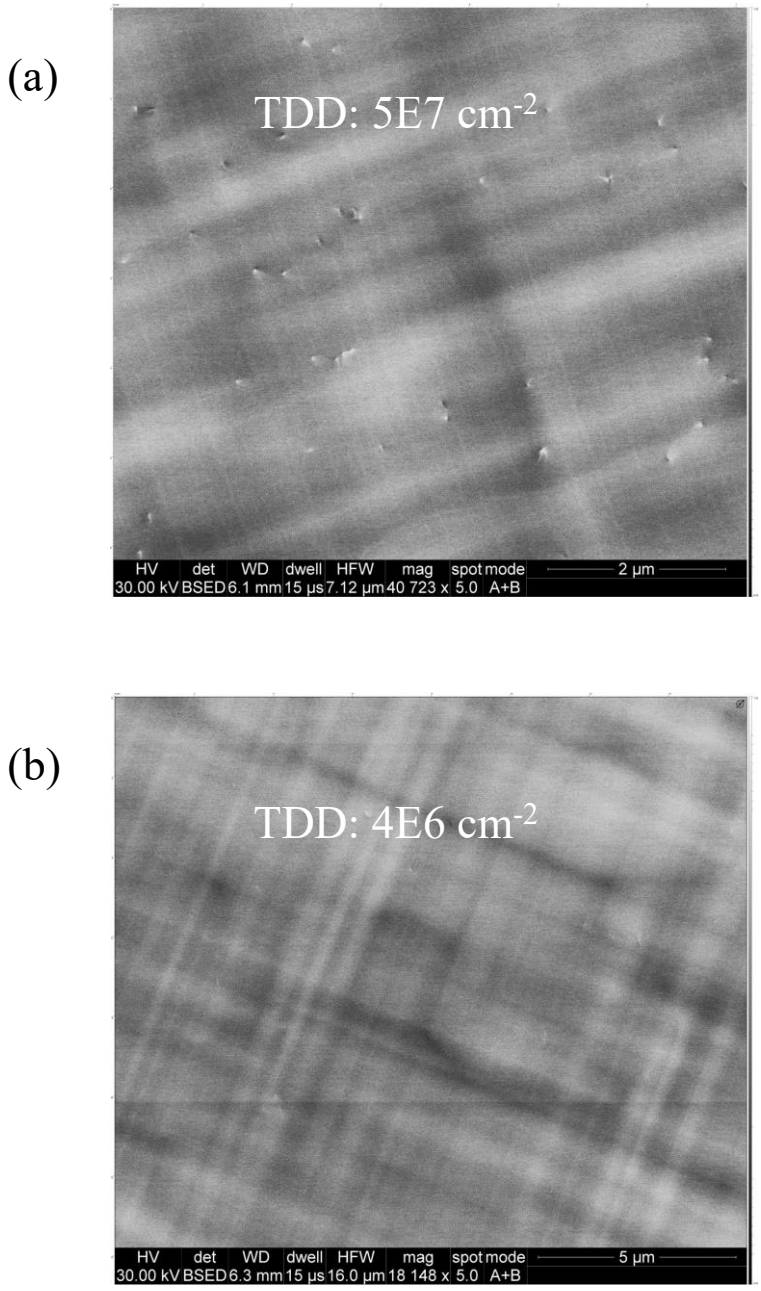

Figure 4.8. ECCI of the GoVS after the first two SLSs (a) and after the last two SLSs (b).

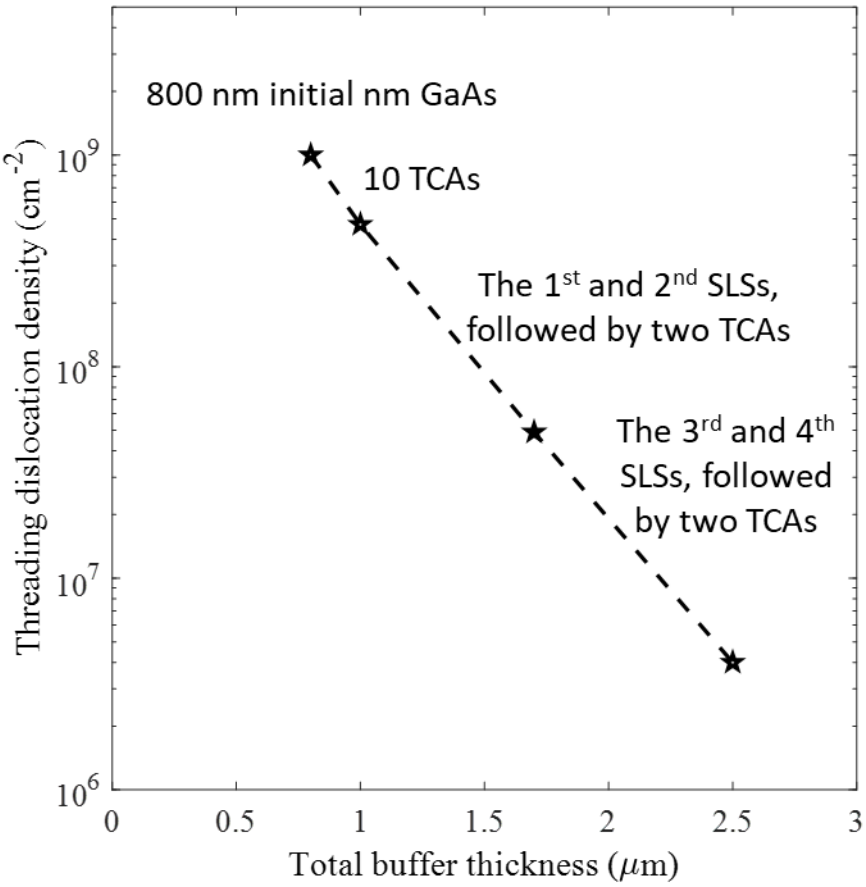

Figure 4.9. The trend of TDD reduction by the TCA and SLSs technology.

of SLS structures as dislocation filters in GaAs grown on Si is based on the principle of dislocation blocking. Dislocations propagate from the substrate into the GaAs film until they encounter an interface that is a barrier to their motion. The SLS structures act as barriers to dislocation motion and effectively block the propagation of dislocations into the GaAs film. As a result, the density of dislocations in the GaAs film is reduced. Each SLS comprises ten pairs of InGaAs/GaAs thin layer structures in this work. Four SLSs were applied, and adjacent SLSs were separated by 300 nm GaAs spacers. After every two SLSs, two cycles of TCAs decrease the TDD further. The whole layer stack structure is shown in Fig. 4.7. ECCI characterization was conducted to show the effect of SLS on TDD reduction in Fig. 4.8. The

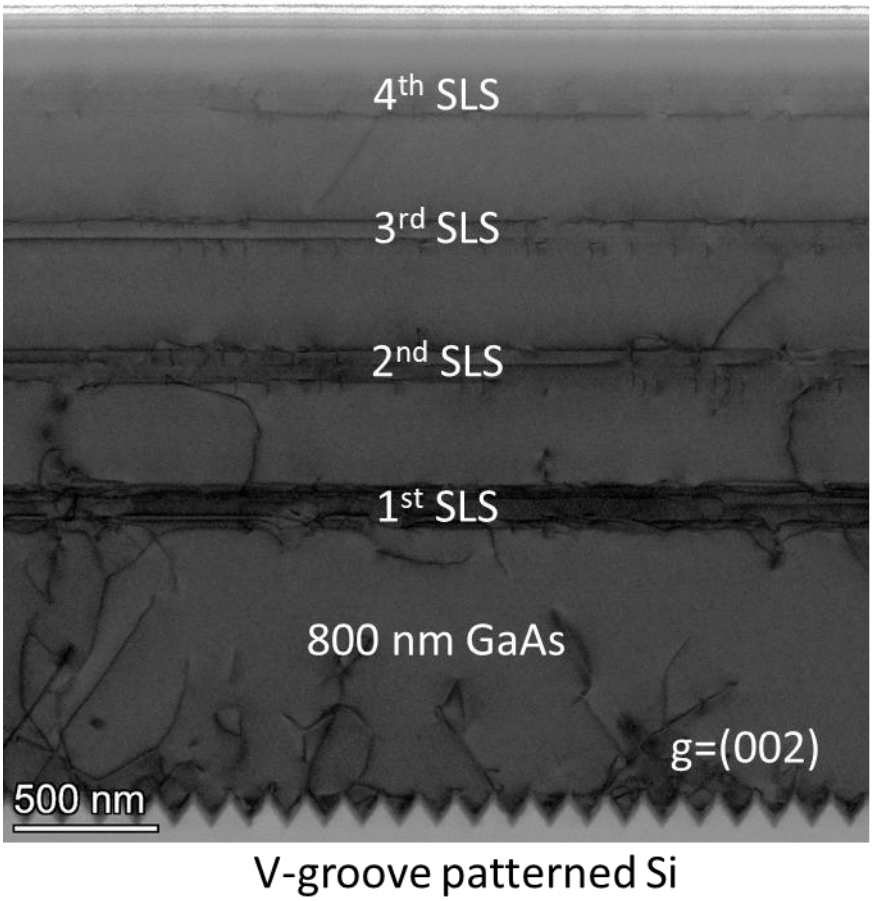

Figure 4.10. Cross-section TEM view to show the evolution of threading dislocation reduction through the TCA and SLS technology.

TDD is decreased to 5E7 cm^{-2} after the first two SLSs and then further decreased to 4E6 cm^{-2} after the final two SLSs. The trend of TDD reduction by TCA and SLS has been summarized in the plot of Fig. 4.9. Cross-section of the TEM view also shows the effect of TCA and SLS on threading dislocation in Fig. 4.10. We can learn that the threading dislocations can be first partly trapped within the nano trench structure due to the aspect ratio trapping effect. After that, TCA and SLS effectively decrease the threading dislocation density. The surface roughness of the surface of GoVS after the growth of all SLSs is about 2.7 nm, revealed by a 50 × 50 μm^2 AFM scanning in Fig. 4.11.

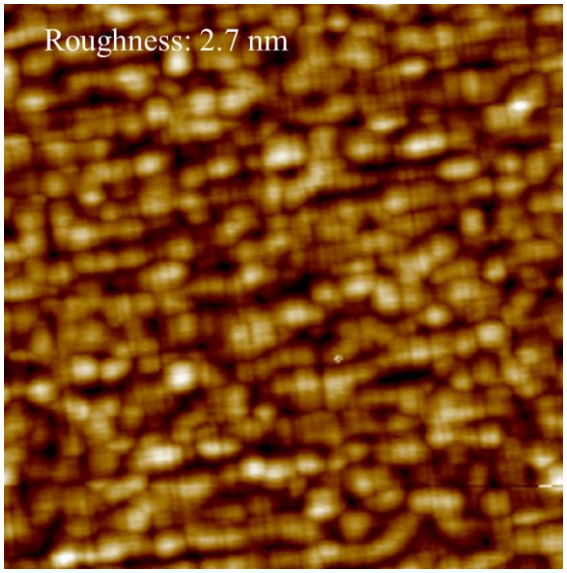

Figure 4.11. A 50 × 50 μm^2 AFM scanning of the surface of GoVS after all SLSs growth, revealing a roughness of about 2.7 nm.

The coefficient of thermal expansion mismatch between GaAs and the Si substrate causes problems during the cooling process after growth. After growing a film a few microns thick,

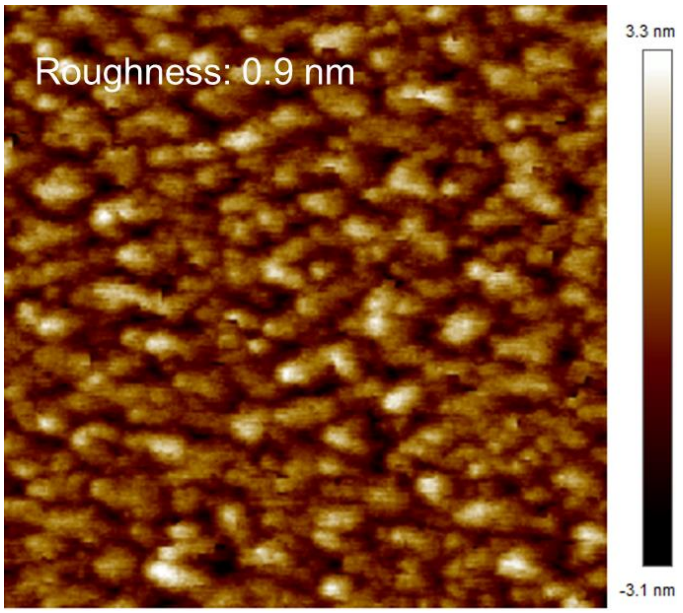

Figure 4.12. A 20 μm × 20 μm AFM scanning of surface after 800 nm GaAs grown on GaP-on-Si sample, followed by 10 period of TCAs.

residual strain is expected when cooling to room temperature. This strain has two primary effects. First, it leads to cracking in the III-V film if there are nucleation centers. Second, the residual stress generates additional dislocations during the epitaxy process, which will finally degenerate the device performance. Experimental values indicate that the cracking threshold

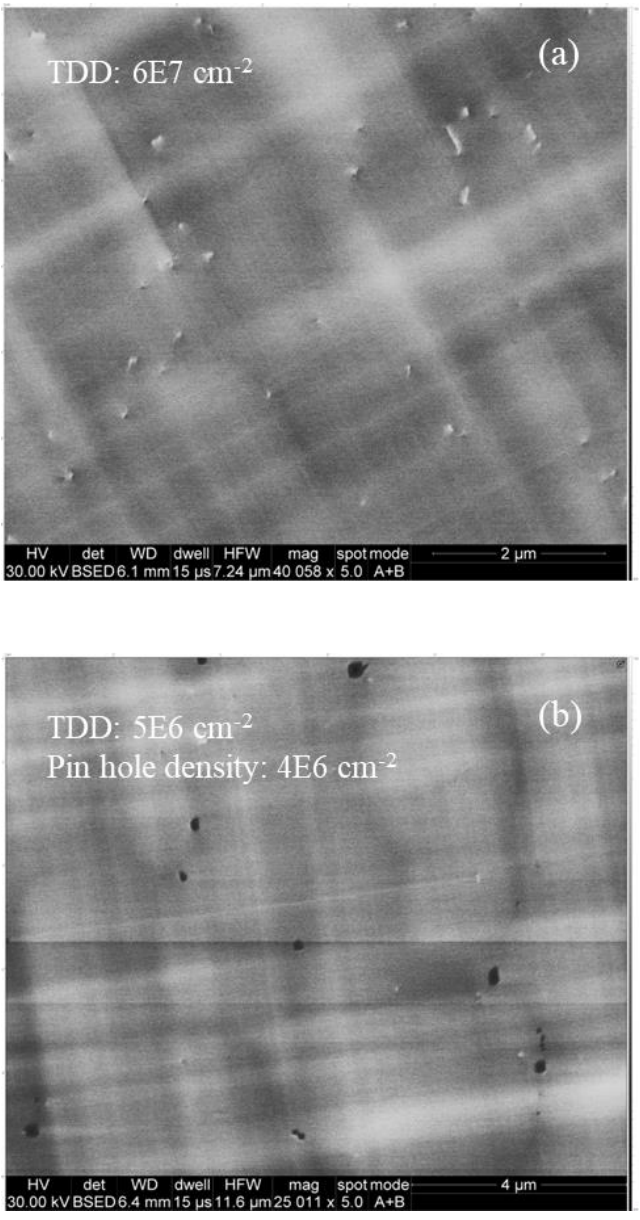

Figure 4.13. ECCI characterization for the surface of GaAs on GaP-on-Si sample (a) after the first two SLSs growth and (b) after the last two SLSs growth.

is closer to 6-7 μm. Since the total thickness of the GoVS is below 2.5 μm and still achieves a low TDD and surface roughness, the crack problem caused by the CTE should not be serious.

The same technology of TCA and SLS was also applied to the GaP-on-Si sample (from manufacturer $NAsP_{III/V}$), where the antiphase boundary was effectively suppressed through Si homoepitaxy and high-temperature annealing processes. The exact recipe of the initial 800 nm GaAs was conducted on the GaP-on-Si sample, followed by ten periods of TCAs. The surface shows a roughness of 0.9 nm, revealed by a 20 μm × 20 μm AFM scanning as shown in Fig. 4.12. After that, four periods of SLSs were applied to decrease the threading

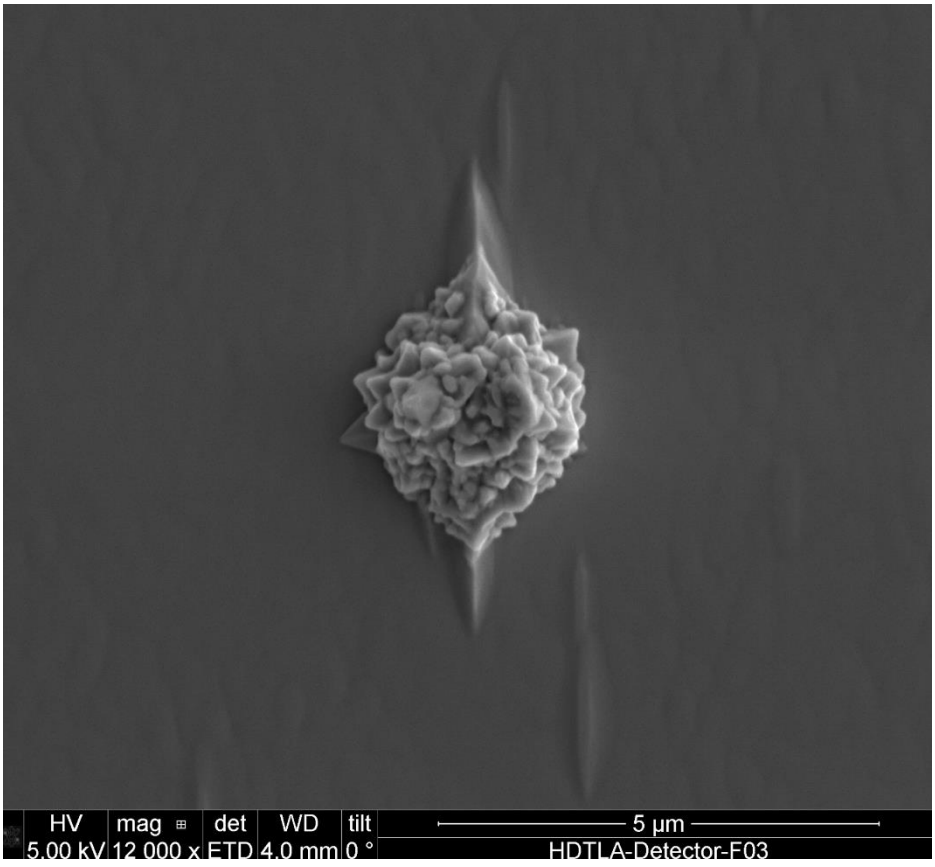

Figure 4.14. Surface defects of InGaP grown on GoVS at a growth temperature of 550 °C.

dislocation density. The layer stack structure and the growth recipe of the SLS are the same as the GoVS sample. After the first two SLSs, the surface shows a threading dislocation density of about 6E7 cm^{-2}, as shown by the ECCI image in Fig. 4.13a, similar to the GoVS sample. After the last two SLSs deposition, the threading dislocation density becomes 5E6 cm^{-2}, shown in the ECCI in Fig. 4.13b. However, Fig. 4.13b shows that the pinhole generated after finishing the four SLSs with a density of about 4E6 cm^{-2}. No pinhole was observed for the GoVS sample. The possible reason is that the pinhole was generated due to the stress accumulation induced by the SLSs and thermal mismatch. As for the GoVS sample, part of the stress was released within the V-groove structure. Given the existence of pinholes, the GoVS sample was finally chosen as the template for whole laser structure growth.

4.3 Full laser structure growth on Si and material characterization

A high-quality cladding layer is critical to forming a complete laser structure on Si. As mentioned in the second section, phase separation is the major problem for InGaP, and growth temperature is the critical parameter for suppressing phase separation. For InGaP growth on GoVS, we observed that the built-in stress could induce phase separation. The phase separation is severe by the recipe, which could form a thick InGaP layer on GaAs with bare phase separation. Fig. 4.14 shows that the surface morphology of the defects for InGaP grown on GoVS differs from that of the GaAs wafer shown in the second section. Besides the new surface

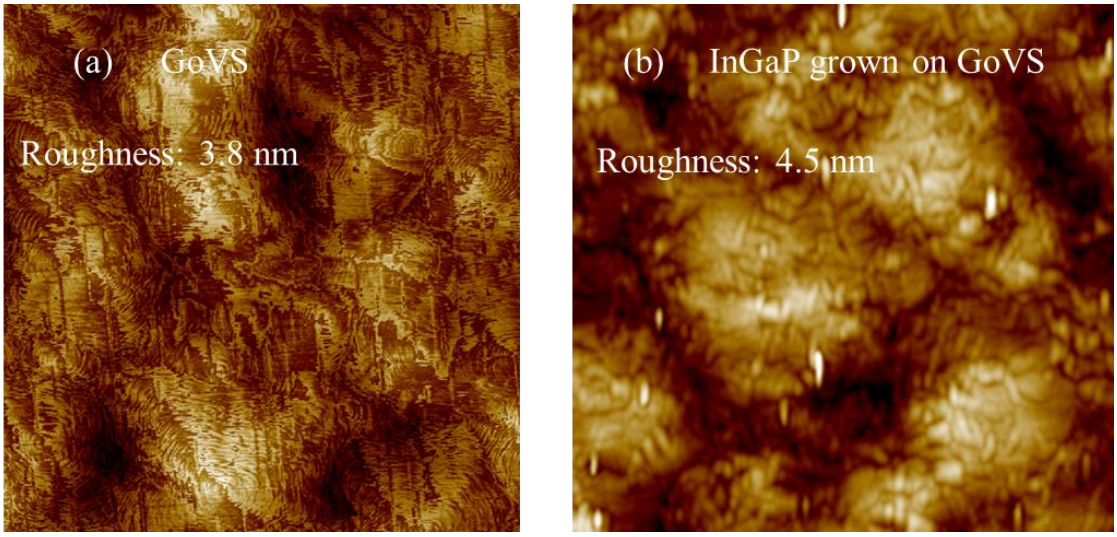

Figure 4.15. AFM scanning for (a) GoVS and (b)1.3 μm thick InGaP grown on GoVS.

defects, the surface roughness also increased significantly. The GoVS sample used for InGaP growth calibration growth has a roughness of 3.5 nm. After 1.3 μm of InGaP growth under 550 °C, the surface roughness increased to 10 nm. By growth calibration, we observed that a lower growth temperature than 550 °C is essential. By decreasing the growth temperature to 525 °C,

Figure 4.16. Optical microscope of the surface of 1.3 μm of InGaP grown on GoVS.

the surface roughness becomes just 4.5 nm, shown in the AFM image of the surface morphology before and after InGaP growth in Fig. 4.15.

Even though InGaP grown on GoVS has shown reduced surface roughness, defects induced by phase separation still exist, as shown in the optical microscope in Fig. 4.16. These surface defects should not influence the fabrication and ohmic contact formation for the upper cladding layer. However, the lower cladding layer has a high requirement on the surface condition. As for the lower cladding layer, such surface defects can negatively influence the material quality of the active region by decreasing the quantum efficiency and increasing the internal optical loss. Therefore, we explore using AlGaAs as the lower cladding layer. AlGaAs is intrinsically lattice-matched with GaAs material. Even if the composition of AlGaAs varied during the growth, it would not break the lattice-matched conditions. The aluminum composition is 40%, so the bandgap is similar to lattice-matched InGaP on GaAs. 1.3 μm thick AlGaAs grown on GaAs at

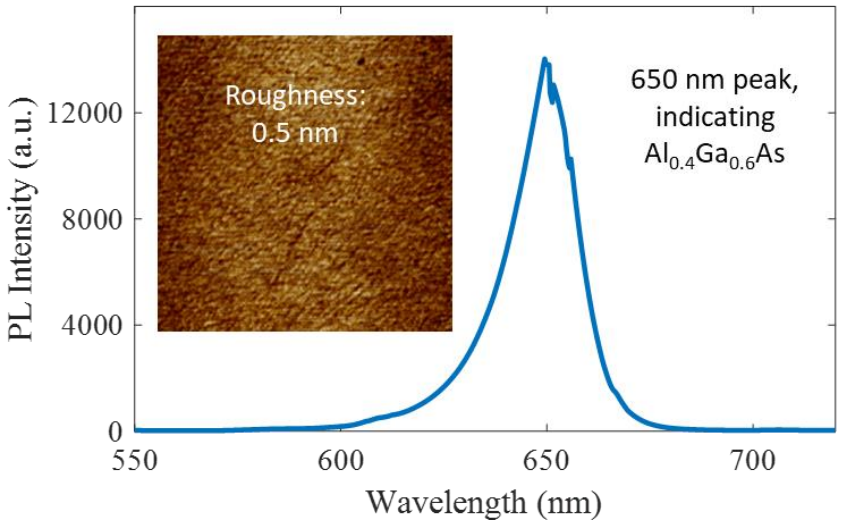

Figure 4.17. AFM and PL characterization of the 1.3 μm thick AlGaAs on GaAs.

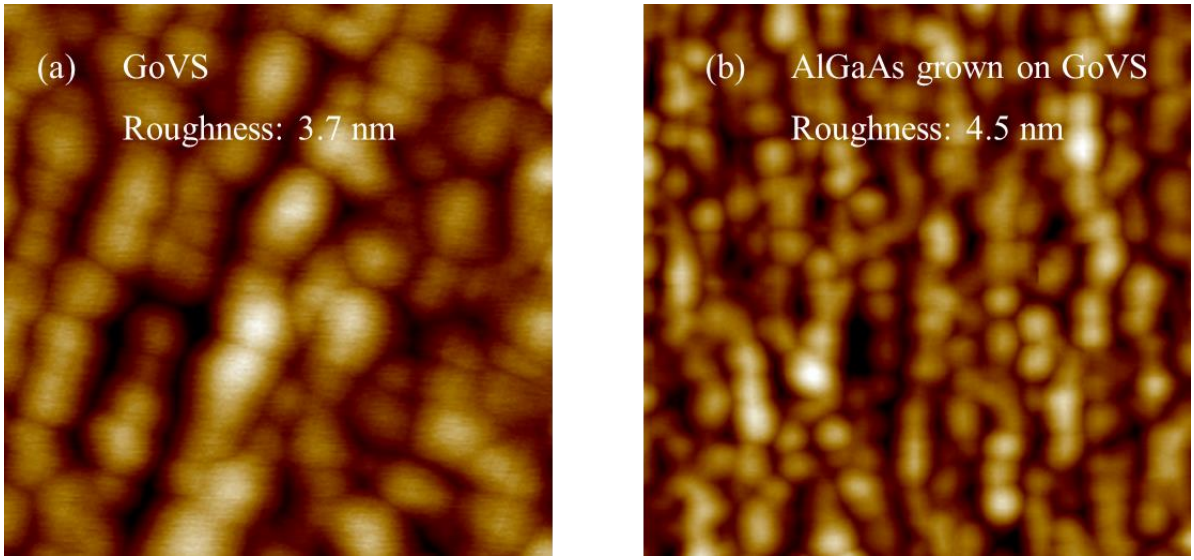

Figure 4.18. AFM scanning for (a) GoVS and (b) AlGaAs grown on GoVS.

630 °C show a surface roughness of 0.5 nm, and the PL characterization revealed that aluminum

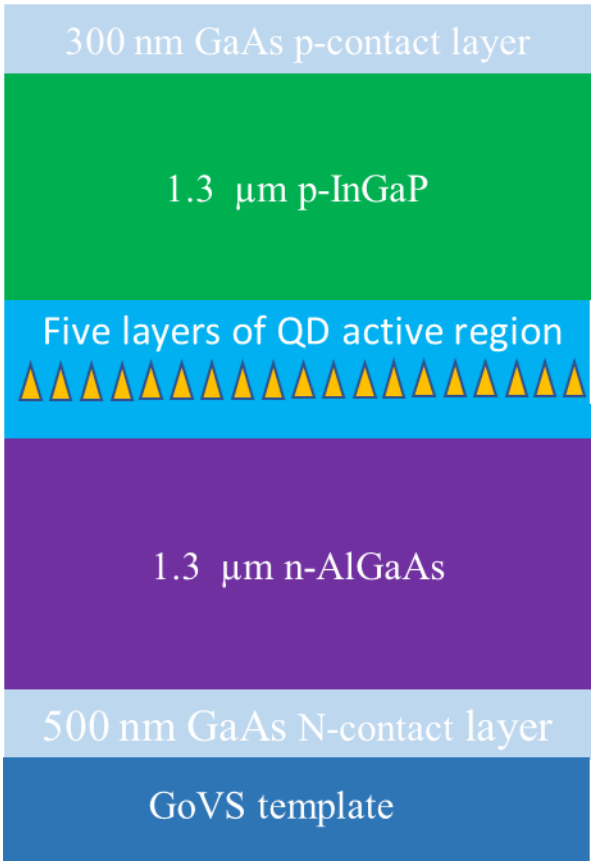

Figure 4.19. Layer stacks of the whole laser structure grown on GoVStempalte.

composition is about 40%, shown in Fig. 4.17. The calibration shows that growing 1.3-μm-thick AlGaAs will not increase the surface roughness of GoVS, shown in the AFM characterization in Fig. 4.18.

The layer stack of the complete laser structure on Si is shown in Fig. 4.19. The whole laser structure was grown on the GoVS platform, whose layer stack is described in Fig. 4.7. AlGaAs was chosen as the lower cladding layer because of the better surface quality after grown on GoVS; InGaP was chosen as the upper cladding layer because of its lower growth temperature (525 °C), which can protect the QD active region. The active region contains five layers of QDs, and high-doped n- and p- GaAs as the contact layers. The sample has a shiny surface after the whole laser structure growth, as shown in the picture in Fig. 4.20.

XRD and PL were performed to Characterize the laser on the GoVS material in Fig. 4. 21. Compared to the laser structure grown on native GaAs substrate, the PL peak wavelength of the laser structure grown on GoVS has a blue shift (from 1260 nm to 1240 nm), and the peak

Figure 4.20. Picture of the full laser structure grown on GoVS sample.

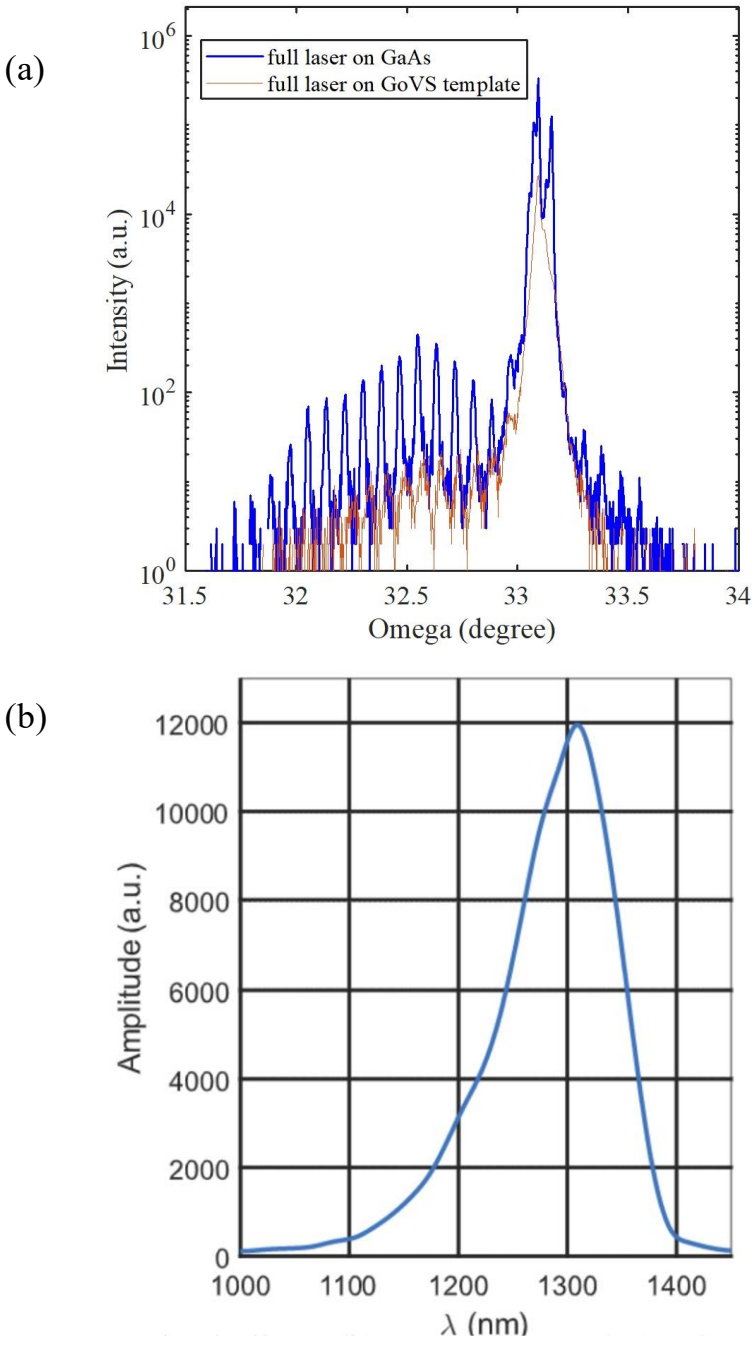

Figure 2.21. XRD (a) and PL (b) characterization of the laser structure grown on GoVS and native GaAs wafer.

intensity is also slightly weaker. The blue shift is due to the different surface temperatures during growth due to the difference in thermal conductivity between the GoVS sample and GaAs and

the residual strain for the GoVS sample. From the XRD characterization, it can be found that the laser on the GaAs sample has sharper peaks generating the multi-layer structure at the QD active region than those for the laser on the GoVS sample. The intensity of those peaks reflects the layer interface quality. The GoVS sample has a higher surface roughness and, thus, has a worse layer interface quality.

4.4 Fabrication and device performance

The fabrication process flow of the laser on the Si sample is nearly similar to the fabrication on GaAs, described detailedly in Section 3. One difference is that the laser on the Si sample contains AlGaAs for the lower cladding layer and InGaP for the upper cladding layer, while the laser on the GaAs sample utilizes InGaP for both the upper and lower cladding layers. As a result, the etching temperature cannot be as high as 200 °C because such a high temperature can cause severe undercut etching of the AlGaAs layers. By optimizing the etching recipe, a smooth and vertical sidewall of the deep etch ridge was achieved by an ICP-etching at 60 °C. After that, a dielectric layer was deposited to passivate the etched ridge, and the etching window for the n-contact area was opened by an additional lithograph and hard mask etching process. Another dry etching step was applied to expose the high-doped n-GaAs contact layer. Another critical difference is that the n-contact probe metal for the laser on the Si sample should have a cross-ridge configuration to minimize the electrical resistance. The reason is that the electrical resistivity of the n-GaAs on GoVS is much higher than that on the GaAs wafer due to the defects in the material. Fig. 4. 22a the cross-section SEM of the laser ridge with a smooth and vertical

(a)

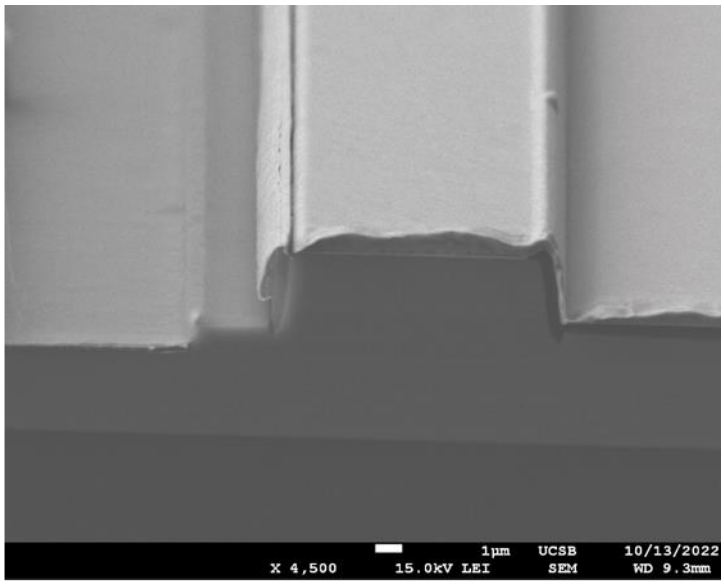

(b)

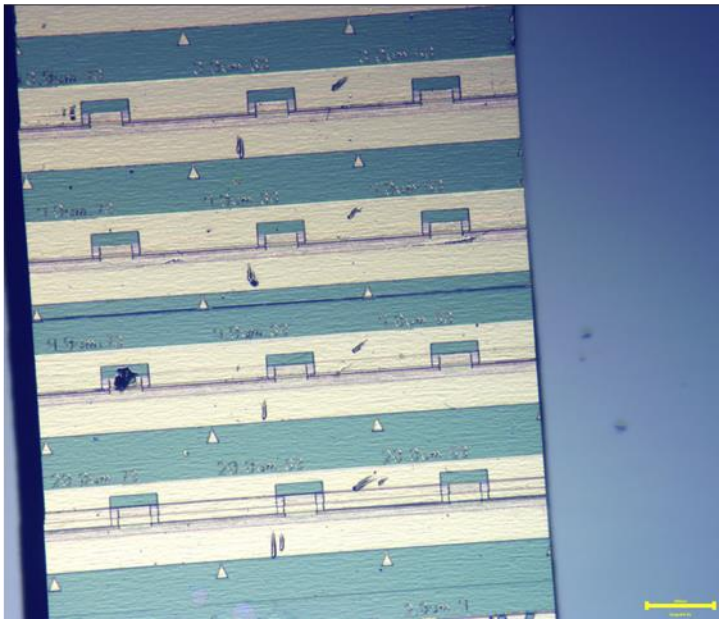

Figure 4. 22. (a) Cross-section SEM of the deep-etched ridge and (b) optical microscope of the sample surface after formation of the probe metal pad.

sidewall. The ridge has a two-step etching process to expose the n-GaAs contact layer. Fig. 4. 22b is the optical microscope image of the sample surface after the formation of the probe pad metal, illustrating the cross-ridge n probe pad configuration.

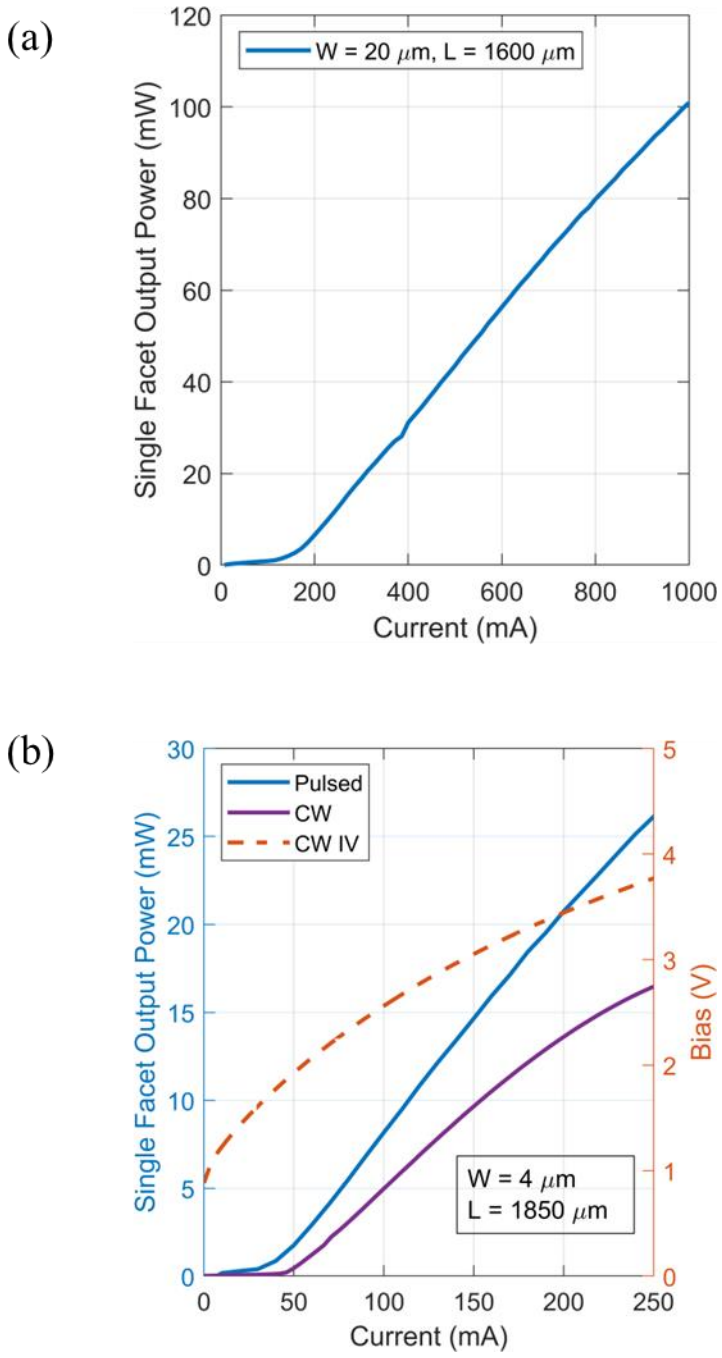

Figure 4. 23. LIV curve for one broad area laser (20 µm × 1600 µm), and one narrow ridge laser (4 µm × 1850 µm).

After device fabrication, the sample was cleaved into laser bars and mounted on a temperature-controlled stage for measurement. In Fig. 4. 23a, up to 100 mW output power from

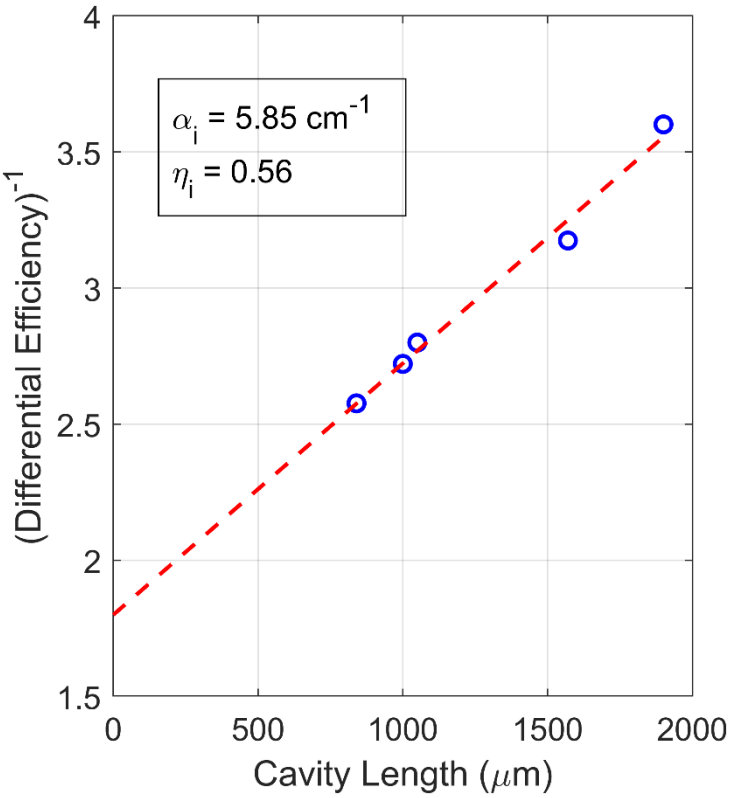

Figure 4.24. Inverse differential efficiency versus cavity length to extract internal loss and injection efficiency for 4 µm wide lasers.

a single facet was demonstrated for a broad area laser with a dimension of 20 µm width and 1600-µm long. Fig. 4. 23b shows the LIV curve for a 4-µm-wide and 1850-µm-long laser at room temperature under both pulsed and continuous wave (CW) current operation. This laser demonstrates a CW threshold current of 46.8 mA (354 A/cm2 threshold current density), and up to 16 mW CW power from a single facet. Under pulsed current operation, the single facet output power is greater than 25 mW, and the threshold current is 38 mA (289 A/cm2 threshold current density). Additional pulsed measurements were performed for 4-µm wide lasers of varying lengths to extract internal loss and injection efficiency. The results are shown in Fig 4. 24, which plots inverse differential efficiency versus cavity length to extract the internal loss of 5.85 cm^{-1} and injection efficiency of 0.56. The diode series resistance for these devices was higher than

expected, which degrades the CW performance due to self-heating and explains the significant difference in threshold current for pulsed versus CW operation. However, we have attributed this to a fabrication issue in forming the n-contacts, not the epitaxial growth issue.

The QD laser on Si performance has a big gap to the MOCVD grown QD laser on GaAs in this thesis or state-of-the-art QD laser on Si [33], in the metrics such as efficiency and threshold current density. The threading dislocation density is still not low enough, which works as non-radiation center in the active region. The mixed AlGaAs and InGaP cladding material, making the deep-etching sidewall quality lower than laser with single material (InGaP or AlGaAs) for the cladding layer. The doping in the AlGaAs is not optimized for the lower cladding layer because of the high background p-doing that makes a low n-type doing level, and therefore increase the total serial resistance.

Chapter 5

Conclusion and Outlooks

Throughout the thesis, the overall target is to develop high-performance MOCVD-grown QD lasers to facilitate the application of QD lasers in communication or sensing. The MOCVD growth mechanism of InAs QD was first explored. By optimizing the InAs QD growth parameters, including growth temperature, V/III, growth rate, and capping process, highly uniform QDs have been achieved with a dot density of about 5.5E10cm^{-2}. Room temperature PL characterization on the QDs shows a 50 nm FWHM for the ground state. A high-quality InGaP thick layer under low temperatures was also developed as the cladding layer for the laser structure. High-performance FP cavity QD laser on GaAs substrate was first demonstrated with state-of-the-art performance. The broad-area laser without facet coating shows a single facet power of 200 mW; the short narrow-ridge laser without facet coating shows a high wall-plug efficiency of about 30%. To enable a QD laser on Si, the GoVS template was developed. Combining the technology of aspect ratio trap, thermal cycle annealing, and strain layer superlattice, the GoVS sample has achieved a low threading dislocation density (4E6cm^{-2}) and a surface roughness of 2.7 nm. The full laser structure was grown on the GoVS sample with AlGaAs as the lower cladding layer and low-temperature InGaP as the upper cladding layer. The laser on Si has shown a decent device performance at room temperature and continuous-wave operation.

The following technology can be developed based on the QD laser platform developed in this thesis work to make the QD laser more functional and meaningful for real applications. First, since the QD laser has a narrow linewidth enhancement, the DFB QD laser can be a promising solution for a single-wavelength narrow linewidth laser source, which can be applied in coherent

communication, microwave photonics, or sensing applications. Besides, since GaAs is a mature platform with a larger wafer than InP, active-passive integration on the QD laser platform can be explored for QD photonic integrated circuits on the GaAs platform. Last, the QD laser on the Si platform has been achieved with decent performance. The next step should be to couple the light from the laser to the waveguide on the Si photonics chip. The whole laser structure can be selectively grown in the trench on the Si photonics chip to align the optical axis of the laser and passive waveguide. Therefore, either butt-coupling or evanescent-wave coupling mechanics can be utilized, which can be a promising solution for laser integration for si photonics.

Reference

1. V. M. Hietala, S. H. Kravitz, M. G. Armendariz, G. A. Vawter, R. F. Carson, and R. E. Leibenguth, "<title>High-performance GaAs/AlGaAs optical phase modulators for microwave/photonic integrated circuits</title>," in B. M. Hendrickson, ed. (1994), pp. 29–36.
2. K. Luke, P. Kharel, C. Reimer, L. He, M. Loncar, and M. Zhang, "Wafer-scale low-loss lithium niobate photonic integrated circuits," Opt Express **28**(17), 24452 (2020).
3. L. He, M. Zhang, A. Shams-Ansari, R. Zhu, C. Wang, and L. Marko, "Low-loss fiber-to-chip interface for lithium niobate photonic integrated circuits," Opt Lett **44**(9), 2314 (2019).
4. S. Arafin and L. A. Coldren, "Advanced InP Photonic Integrated Circuits for Communication and Sensing," IEEE Journal of Selected Topics in Quantum Electronics **24**(1), (2018).
5. F. A. Kish, D. Welch, R. Nagarajan, J. L. Pleumeekers, V. Lal, M. Ziari, A. Nilsson, M. Kato, S. Murthy, P. Evans, S. W. Corzine, M. Mitchell, P. Samra, M. Missey, S. DeMars, R. P. Schneider, M. S. Reffle, T. Butrie, J. T. Rahn, M. Van Leeuwen, J. W. Stewart, D. J. H. Lambert, R. C. Muthiah, H. S. Tsai, J. S. Bostak, A. Dentai, K. T. Wu, H. Sun, D. J. Pavinski, J. Zhang, J. Tang, J. McNicol, M. Kuntz, V. Dominic, B. D. Taylor, R. A. Salvatore, M. Fisher, A. Spannagel, E. Strzelecka, P. Studenkov, M. Raburn, W. Williams, D. Christini, K. J. Thomson, S. S. Agashe, R. Malendevich, G. Goldfarb, S. Melle, C. Joyner, M. Kaufman, and S. G. Grubb, "Current status of large-scale InP

photonic integrated circuits," IEEE Journal on Selected Topics in Quantum Electronics **17**(6), 1470–1489 (2011).

6. A. Boes, B. Corcoran, L. Chang, J. Bowers, and A. Mitchell, "Status and Potential of Lithium Niobate on Insulator (LNOI) for Photonic Integrated Circuits," Laser Photon Rev **12**(4), (2018).
7. C. P. Dietrich, A. Fiore, M. G. Thompson, M. Kamp, and S. Höfling, "GaAs integrated quantum photonics: Towards compact and multi-functional quantum photonic integrated circuits," Laser Photon Rev **10**(6), 870–894 (2016).
8. B. R. Koch, E. J. Norberg, B. Kim, J. Hutchinson, J.-H. Shin, G. Fish, and A. Fang, "Integrated Silicon Photonic Laser Sources for Telecom and Datacom," in *Optical Fiber Communication Conference/National Fiber Optic Engineers Conference 2013* (Optica Publishing Group, 2013), p. PDP5C.8.
9. K. Nishi, K. Takemasa, M. Sugawara, and Y. Arakawa, "Development of Quantum Dot Lasers for Data-Com and Silicon Photonics Applications," IEEE Journal of Selected Topics in Quantum Electronics **23**(6), 1–7 (2017).
10. M. Asghari, "Silicon Photonics: A Low Cost Integration Platform for Datacom and Telecom Applications," in *Optical Fiber Communication Conference/National Fiber Optic Engineers Conference* (Optica Publishing Group, 2008), p. NThA4.
11. Y. Shi, Y. Zhang, Y. Wan, Y. Yu, Y. Zhang, X. Hu, X. Xiao, H. Xu, L. Zhang, and B. Pan, "Silicon photonics for high-capacity data communications," Photon. Res. **10**(9), A106–A134 (2022).
12. Y. A. Vlasov, "Silicon CMOS-integrated nano-photonics for computer and data communications beyond 100G," IEEE Communications Magazine **50**(2), s67–s72 (2012).

13. H. Hashemi, "A Review of Silicon Photonics LiDAR," in *2022 IEEE Custom Integrated Circuits Conference (CICC)* (2022), pp. 1–8.

14. C. v Poulton, A. Yaacobi, D. B. Cole, M. J. Byrd, M. Raval, D. Vermeulen, and M. R. Watts, "Coherent solid-state LIDAR with silicon photonic optical phased arrays," Opt. Lett. **42**(20), 4091–4094 (2017).

15. X. Zhang, K. Kwon, J. Henriksson, J. Luo, and M. C. Wu, "A large-scale microelectromechanical-systems-based silicon photonics LiDAR," Nature **603**(7900), 253–258 (2022).

16. P. Bhargava, T. Kim, C. v Poulton, J. Notaros, A. Yaacobi, E. Timurdogan, C. Baiocco, N. Fahrenkopf, S. Kruger, T. Ngai, Y. Timalsina, M. R. Watts, and V. Stojanović, "Fully Integrated Coherent LiDAR in 3D-Integrated Silicon Photonics/65nm CMOS," in *2019 Symposium on VLSI Circuits* (2019), pp. C262–C263.

17. T. Baba, T. Tamanuki, H. Ito, M. Kamata, R. Tetsuya, S. Suyama, H. Abe, and R. Kurahashi, "Silicon Photonics FMCW LiDAR Chip With a Slow-Light Grating Beam Scanner," IEEE Journal of Selected Topics in Quantum Electronics **28**(5: Lidars and Photonic Radars), 1–8 (2022).

18. C. G. H. Roeloffzen, L. Zhuang, C. Taddei, A. Leinse, R. G. Heideman, P. W. L. van Dijk, R. M. Oldenbeuving, D. A. I. Marpaung, M. Burla, and K.-J. Boller, "Silicon nitride microwave photonic circuits," Opt. Express **21**(19), 22937–22961 (2013).

19. W. Zhang and J. Yao, "Silicon-Based Integrated Microwave Photonics," IEEE J Quantum Electron **52**(1), 1–12 (2016).

20. R. Maram, S. Kaushal, J. Azaña, and L. R. Chen, "Recent Trends and Advances of Silicon-Based Integrated Microwave Photonics," Photonics **6**(1), (2019).

21. R. Dingle, W. Wiegmann, and C. H. Henry, "Quantum States of Confined Carriers in Very Thin AlGaAs/GaAs/AlGaAs Heterostructures," Phys Rev Lett **33**(14), 827–830 (1974).

22. B. Sumpf, M. Zorn, R. Staske, J. Fricke, P. Ressel, G. Erbert, M. Weyers, and G. Tränkle, "High-efficient 650 nm laser bars with an output power of about 10 W and a wall-plug efficiency of 30%," in *Novel In-Plane Semiconductor Lasers V*, C. Mermelstein and D. P. Bour, eds. (SPIE, 2006), **6133**, p. 61330D.

23. A. Müller, C. Zink, J. Fricke, F. Bugge, G. Erbert, B. Sumpf, and G. Tränkle, "Efficient, High Brightness 1030 nm DBR Tapered Diode Lasers With Optimized Lateral Layout," IEEE Journal of Selected Topics in Quantum Electronics **23**(6), 1–7 (2017).

24. S. R. Selmic, G. A. Evans, T. M. Chou, J. B. Kirk, J. N. Walpole, J. P. Donnelly, C. T. Harris, and L. J. Missaggia, "Single frequency 1550-nm AlGaInAs-InP tapered high-power laser with a distributed Bragg reflector," IEEE Photonics Technology Letters **14**(7), 890–892 (2002).

25. Y.-C. Chi, D.-H. Hsieh, C.-T. Tsai, H.-Y. Chen, H.-C. Kuo, and G.-R. Lin, "450-nm GaN laser diode enables high-speed visible light communication with 9-Gbps QAM-OFDM," Opt. Express **23**(10), 13051–13059 (2015).

26. Y. Arakawa and H. Sakaki, "Multidimensional quantum well laser and temperature dependence of its threshold current," Appl Phys Lett **40**(11), 939–941 (1982).

27. L. Wang, H. Zhao, B. Shi, S. Pinna, S. S. Brunelli, F. Sang, B. Song, and J. Klamkin, "High Performance 1.3 μm Aluminum-Free Quantum Dot Lasers Grown by MOCVD," in *Optical Fiber Communication Conference (OFC) 2020* (OSA, 2020), p. T4H.2.

28. H. Y. Liu, D. T. Childs, T. J. Badcock, K. M. Groom, I. R. Sellers, M. Hopkinson, R. A. Hogg, D. J. Robbins, D. J. Mowbray, and M. S. Skolnick, "High-performance three-layer 1.3-μm InAs-GaAs quantum-dot lasers with very low continuous-wave room-temperature threshold currents," IEEE Photonics Technology Letters **17**(6), 1139–1141 (2005).

29. O. B. Shchekin and D. G. Deppe, "Low-threshold high-T0 1.3-μm InAs quantum-dot lasers due to p-type modulation doping of the active region," IEEE Photonics Technology Letters **14**(9), 1231–1233 (2002).

30. O. B. Shchekin, J. Ahn, and D. G. Deppe, "High temperature performance of self-organised quantum dot laser with stacked p-doped active region," Electron Lett **38**(14), 712–713 (2002).

31. O. B. Shchekin and D. G. Deppe, "1.3 μm InAs quantum dot laser with To=161K from 0 to 80°C," Appl Phys Lett **80**(18), 3277–3279 (2002).

32. S. S. Mikhrin, A. R. Kovsh, I. L. Krestnikov, A. v. Kozhukhov, D. A. Livshits, N. N. Ledentsov, Y. M. Shernyakov, I. I. Novikov, M. v. Maximov, V. M. Ustinov, and Z. I. Alferov, "High power temperature-insensitive 1.3 μm InAs/InGaAs/GaAs quantum dot lasers," Semicond Sci Technol **20**(5), 340–342 (2005).

33. C. Shang, Y. Wan, J. Selvidge, E. Hughes, R. Herrick, K. Mukherjee, J. Duan, F. Grillot, W. W. Chow, and J. E. Bowers, "Perspectives on Advances in Quantum Dot Lasers and Integration with Si Photonic Integrated Circuits," ACS Photonics **8**(9), 2555–2566 (2021).

34. K. Sears, M. Buda, H. H. Tan, and C. Jagadish, "Modeling and characterization of InAsGaAs quantum dot lasers grown using metal organic chemical vapor deposition," J Appl Phys **101**(1), (2007).

35. J. J. Coleman, J. D. Young, and A. Garg, "Semiconductor quantum dot lasers: A tutorial," Journal of Lightwave Technology **29**(4), 499–510 (2011).

36. T. Kaizu and K. Yamaguchi, "Uniform formation of two-dimensional and three-dimensional InAs Islands on GaAs by molecular beam epitaxy," Japanese Journal of Applied Physics, Part 1: Regular Papers and Short Notes and Review Papers **42**(4 A), 1705–1708 (2003).

37. X. Lu, M. Koyama, Y. Izumi, Y. Nakata, S. Adachi, and S. Muto, "Size distribution and scaling behavior of InAlAs/AlGaAs quantum dots grown on gaas by molecular beam epitaxy," Jpn J Appl Phys **52**(2), (2013).

38. K. Yamaguchi, K. Yujobo, and T. Kaizu, *Self Size-Limiting Process of InAs Quantum Dots Grown by Molecular Beam Epitaxy Related Content Stranski-Krastanov Growth of InAs Quantum Dots with Narrow Size Distribution Self Size-Limiting Process of InAs Quantum Dots Grown by Molecular Beam Epitaxy* (2001), **40**(3B).

39. R. P. Mirin, J. P. Ibbetson, K. Nishi, A. C. Gossard, and J. E. Bowers, "1.3 μm photoluminescence from InGaAs quantum dots on GaAs," Appl Phys Lett **67**(25), 3795–3797 (1995).

40. A. Salhi, L. Fortunato, L. Martiradonna, M. T. Todaro, R. Cingolani, A. Passaseo, and M. De Vittorio, "High efficiency and high modal gain InAs/InGaAs/GaAs quantum dot lasers emitting at 1300 nm," Semicond Sci Technol **22**(4), 396 (2007).

41. M. V Maximov, V. M. Ustinov, A. E. Zhukov, N. V Kryzhanovskaya, A. S. Payusov, I. I. Novikov, N. Y. Gordeev, Y. M. Shernyakov, I. Krestnikov, D. Livshits, S. Mikhrin, and A. Kovsh, "A 1.33 μm InAs/GaAs quantum dot laser with a 46 cm−1 modal gain," Semicond Sci Technol **23**(10), 105004 (2008).

42. T. Amano, T. Sugaya, and K. Komori, "1.3-μm InAs quantum-dot laser with high dot density and high uniformity," IEEE Photonics Technology Letters **18**(4), 619–621 (2006).

43. N. Kirstaedter, O. G. Schmidt, N. N. Ledentsov, D. Bimberg, V. M. Ustinov, A. Yu. Egorov, A. E. Zhukov, M. V Maximov, P. S. Kop'ev, and Zh. I. Alferov, "Gain and differential gain of single layer InAs/GaAs quantum dot injection lasers," Appl Phys Lett **69**(9), 1226–1228 (1996).

44. G. T. Liu, A. Stintz, H. Li, T. C. Newell, A. L. Gray, P. M. Varangis, K. J. Malloy, and L. F. Lester, "The influence of quantum-well composition on the performance of quantum dot lasers using InAs-InGaAs dots-in-a-well (DWELL) structures," IEEE J Quantum Electron **36**(11), 1272–1279 (2000).

45. T. Kageyama, K. Nishi, M. Yamaguchi, R. Mochida, Y. Maeda, K. Takemasa, Y. Tanaka, T. Yamamoto, M. Sugawara, and Y. Arakawa, "Extremely high temperature (220°C) continuous-wave operation of 1300-nm-range quantum-dot lasers," in *2011 Conference on Lasers and Electro-Optics Europe and 12th European Quantum Electronics Conference (CLEO EUROPE/EQEC)* (2011), p. 1.

46. T. C. Newell, D. J. Bossert, A. Stintz, B. Fuchs, K. J. Malloy, and L. F. Lester, "Gain and linewidth enhancement factor in InAs quantum-dot laser diodes," IEEE Photonics Technology Letters **11**(12), 1527–1529 (1999).

47. Z. Zhang, D. Jung, J. C. Norman, W. W. Chow, and J. E. Bowers, "Linewidth Enhancement Factor in InAs/GaAs Quantum Dot Lasers and Its Implication in Isolator-Free and Narrow Linewidth Applications," IEEE Journal of Selected Topics in Quantum Electronics **25**(6), 1–9 (2019).

48. F. Grillot, Bé. Dagens, J.-G. Provost, H. Su, and L. F. Lester, "Gain Compression and Above-Threshold Linewidth Enhancement Factor in 1.3-μm InAs–GaAs Quantum-Dot Lasers," IEEE J Quantum Electron **44**(10), 946–951 (2008).

49. J. Kim and S. L. Chuang, "Theoretical and experimental study of optical gain, refractive index change, and linewidth enhancement factor of p-doped quantum-dot lasers," IEEE J Quantum Electron **42**(9), 942–952 (2006).

50. W. W. Chow, Z. Zhang, J. C. Norman, S. Liu, and J. E. Bowers, "On quantum-dot lasing at gain peak with linewidth enhancement factor αH = 0," APL Photonics **5**(2), 26101 (2020).

51. T. C. Newell, D. J. Bossert, A. Stintz, B. Fuchs, K. J. Malloy, and L. F. Lester, *Gain and Linewidth Enhancement Factor in InAs Quantum-Dot Laser Diodes* (1999), **11**(12).

52. W. W. Chow, Z. Zhang, J. C. Norman, S. Liu, and J. E. Bowers, "On quantum-dot lasing at gain peak with linewidth enhancement factor α H = 0," APL Photonics **5**(2), (2020).

53. J. Duan, H. Huang, B. Dong, D. Jung, J. C. Norman, J. E. Bowers, and F. Grillot, "1.3- μ m Reflection Insensitive InAs/GaAs Quantum Dot Lasers Directly Grown on Silicon," IEEE Photonics Technology Letters **31**(5), 345–348 (2019).

54. J. Duan, H. Huang, B. Dong, J. C. Norman, Z. Zhang, J. E. Bowers, and F. Grillot, "Dynamic and nonlinear properties of epitaxial quantum dot lasers on silicon for isolator-free integration," Photon. Res. **7**(11), 1222–1228 (2019).

55. Y. Ben-Ezra, B. I. Lembrikov, and M. Haridim, "Acceleration of gain recovery and dynamics of electrons in QD-SOA," IEEE J Quantum Electron **41**(10), 1268–1273 (2005).

56. T. W. Berg, S. Bischoff, I. Magnusdottir, and J. Mork, "Ultrafast gain recovery and modulation limitations in self-assembled quantum-dot devices," IEEE Photonics Technology Letters **13**(6), 541–543 (2001).

57. J. Gomis-Bresco, S. Dommers, V. V Temnov, U. Woggon, M. Laemmlin, D. Bimberg, E. Malic, M. Richter, E. Schöll, and A. Knorr, "Impact of Coulomb Scattering on the Ultrafast Gain Recovery in InGaAs Quantum Dots," Phys Rev Lett **101**(25), 256803 (2008).

58. M. Sugawara, K. Mukai, and H. Shoji, "Effect of phonon bottleneck on quantum-dot laser performance," Appl Phys Lett **71**(19), 2791–2793 (1997).

59. K. Kim, J. Urayama, T. B. Norris, J. Singh, J. Phillips, and P. Bhattacharya, "Gain dynamics and ultrafast spectral hole burning in In(Ga)As self-organized quantum dots," Appl Phys Lett **81**(4), 670–672 (2002).

60. Z. G. Lu, J. R. Liu, S. Raymond, P. J. Poole, P. J. Barrios, and D. Poitras, "312-fs pulse generation from a passive C-band InAs/InP quantum dot mode-locked laser," Opt. Express **16**(14), 10835–10840 (2008).

61. Q. Cheng, M. Bahadori, M. Glick, S. Rumley, and K. Bergman, "Recent advances in optical technologies for data centers: a review," Optica **5**(11), 1354 (2018).

62. C. Shang, Y. Wan, J. Selvidge, E. Hughes, R. Herrick, K. Mukherjee, J. Duan, F. Grillot, W. W. Chow, and J. E. Bowers, "Perspectives on Advances in Quantum Dot Lasers and Integration with Si Photonic Integrated Circuits," ACS Photonics **8**(9), 2555–2566 (2021).

63. S. Chen, W. Li, J. Wu, Q. Jiang, M. Tang, S. Shutts, S. N. Elliott, A. Sobiesierski, A. J. Seeds, I. Ross, P. M. Smowton, and H. Liu, "Electrically pumped continuous-wave III-V quantum dot lasers on silicon," Nat Photonics **10**(5), 307–311 (2016).

64. A. Y. Liu, C. Zhang, J. Norman, A. Snyder, D. Lubyshev, J. M. Fastenau, A. W. K. Liu, A. C. Gossard, and J. E. Bowers, "High performance continuous wave 1.3 μ m quantum dot lasers on silicon," Appl Phys Lett **104**(4), (2014).

65. D. Jung, Z. Zhang, J. Norman, R. Herrick, M. J. Kennedy, P. Patel, K. Turnlund, C. Jan, Y. Wan, A. C. Gossard, and J. E. Bowers, "Highly Reliable Low-Threshold InAs Quantum Dot Lasers on On-Axis (001) Si with 87% Injection Efficiency," ACS Photonics **5**(3), 1094–1100 (2018).

66. K. Nishi, K. Takemasa, M. Sugawara, and Y. Arakawa, "Development of Quantum Dot Lasers for Data-Com and Silicon Photonics Applications," IEEE Journal of Selected Topics in Quantum Electronics **23**(6), 1–7 (2017).

67. M. Stubenrauch, G. Stracke, D. Arsenijević, A. Strittmatter, and D. Bimberg, "15 Gb/s index-coupled distributed-feedback lasers based on 1.3 μ m InGaAs quantum dots," Appl Phys Lett **105**(1), (2014).

68. T. D. Germann, A. Strittmatter, T. Kettler, K. Posilovic, U. W. Pohl, and D. Bimberg, "MOCVD of InGaAs/GaAs quantum dots for lasers emitting close to 1.3 μm," J Cryst Growth **298**(SPEC. ISS), 591–594 (2007).

69. J. X. Chen, A. Markus, A. Fiore, U. Oesterle, R. P. Stanley, J. F. Carlin, R. Houdré, M. Ilegems, L. Lazzarini, L. Nasi, M. T. Todaro, E. Piscopiello, R. Cingolani, M. Catalano, J. Katcki, and J. Ratajczak, "Tuning InAs/GaAs quantum dot properties under Stranski-Krastanov growth mode for 1.3 μm applications," J Appl Phys **91**(10), 6710–6716 (2002).

70. D. Leonard, M. Krishnamurthy, C. M. Reaves, S. P. Denbaars, and P. M. Petroff, "Direct formation of quantum-sized dots from uniform coherent islands of InGaAs on GaAs surfaces," Appl Phys Lett **63**(23), 3203–3205 (1993).

71. R. P. Mirin, J. P. Ibbetson, K. Nishi, A. C. Gossard, and J. E. Bowers, "1.3 μm photoluminescence from InGaAs quantum dots on GaAs," Appl Phys Lett **67**(25), 3795–3797 (1995).

72. D. ~L. Huffaker, G. Park, Z. Zou, O. ~B. Shchekin, and D. ~G. Deppe, "Continuous-wave low-threshold performance of 1.3-/spl mu/m InGaAs-GaAs quantum-dot lasers," IEEE Journal of Selected Topics in Quantum Electronics **6**(3), 452–461 (2000).

73. T. M. Quist, R. H. Rediker, R. J. Keyes, W. E. Krag, B. Lax, A. L. McWhorter, and H. J. Zeigler, "SEMICONDUCTOR MASER OF GaAs," Appl Phys Lett **1**(4), 91–92 (1962).

74. M. I. Nathan, W. P. Dumke, G. Burns, F. H. Dill, and G. Lasher, "STIMULATED EMISSION OF RADIATION FROM GaAs p-n JUNCTIONS," Appl Phys Lett **1**(3), 62–64 (1962).

75. N. Holonyak and S. F. Bevacqua, "COHERENT (VISIBLE) LIGHT EMISSION FROM Ga(As1−xPx) JUNCTIONS," Appl Phys Lett **1**(4), 82–83 (1962).

76. J. C. Dyment, "HERMITE-GAUSSIAN MODE PATTERNS IN GaAs JUNCTION LASERS," Appl Phys Lett **10**(3), 84–86 (1967).

77. H. Rupprecht, J. M. Woodall, and G. D. Pettit, "EFFICIENT VISIBLE ELECTROLUMINESCENCE AT 300°K FROM Ga1-xAlxAs p-n JUNCTIONS GROWN BY LIQUID-PHASE EPITAXY," Appl Phys Lett **11**(3), 81–83 (1967).

78. H. Nishi, M. Yano, Y. Nishitani, Y. Akita, and M. Takusagawa, "Self-aligned structure InGaAsP/InP DH lasers," Appl Phys Lett **35**(3), 232–234 (1979).

79. W. T. Tsang, "A graded-index waveguide separate-confinement laser with very low threshold and a narrow Gaussian beam," Appl Phys Lett **39**(2), 134–137 (1981).

80. R. D. Dupuis, P. D. Dapkus, R. Chin, N. Holonyak, and S. W. Kirchoefer, "Continuous 300 °K laser operation of single-quantum-well AlxGa1−xAs-GaAs heterostructure diodes grown by metalorganic chemical vapor deposition," Appl Phys Lett **34**(4), 265–267 (1979).

81. J. P. Duchemin, "Very low threshold GRIN-SCH GaAs/GaAlAs laser structure grown by OM-VPE," Electron Lett **18**(20), 870-871(1) (1982).

82. K. Aiki, M. Nakamura, T. Kuroda, and J. Umeda, "Channeled-substrate planar structure (AlGa)As injection lasers," Appl Phys Lett **30**(12), 649–651 (1977).

83. H. Namizaki, H. Kan, M. Ishii, and A. Ito, "Transverse-junction-stripe-geometry double-heterostructure lasers with very low threshold current," J Appl Phys **45**(6), 2785–2786 (1974).

84. M. B. Panish, H. C. Casey, S. Sumski, and P. W. Foy, "Reduction of threshold current density in GaAs–Alx Ga1−x As heterostructure lasers by separate optical and carrier confinement," Appl Phys Lett **22**(11), 590–591 (1973).

85. Y. Arakawa and H. Sakaki, "Multidimensional quantum well laser and temperature dependence of its threshold current," Appl Phys Lett **40**(11), 939–941 (1982).

86. Z. G. Lu, J. R. Liu, S. Raymond, P. J. Poole, P. J. Barrios, and D. Poitras, "312-fs pulse generation from a passive C-band InAs/InP quantum dot mode-locked laser," Opt. Express **16**(14), 10835–10840 (2008).

87. L. W. Shi, Y. H. Chen, B. Xu, Z. C. Wang, Y. H. Jiao, and Z. G. Wang, "Status and trends of short pulse generation using mode-locked lasers based on advanced quantum-dot active media," J Phys D Appl Phys **40**(18), R307 (2007).

88. E. U. Rafailov, M. A. Cataluna, and W. Sibbett, "Mode-locked quantum-dot lasers," Nat Photonics **1**(7), 395–401 (2007).

89. M. Zander, W. Rehbein, M. Moehrle, S. Breuer, D. Franke, M. Schell, K. Kolpatzeck, and J. C. Balzer, "High performance BH InAs/InP QD and InGaAsP/InP QW mode-locked lasers as comb and pulse sources," in *Optical Fiber Communication Conference (OFC) 2020*, OSA Technical Digest (Optica Publishing Group, 2020), p. T3C.4.

90. H. Schmeckebier, G. Fiol, C. Meuer, D. Arsenijević, and D. Bimberg, "Complete pulse characterization of quantum-dot mode-locked lasers suitable for optical communication up to 160 Gbit/s," Opt Express **18**(4), 3415–3425 (2010).

91. L. Coldren, S. Corzine, and M. Mašanović, "A Phenomenological Approach to Diode Lasers," in *Diode Lasers and Photonic Integrated Circuits* (2012), pp. 45–90.

92. R. Hunsperger and J. Ballantyne, "MEASUREMENT OF PHOTON ABSORPTION LOSS IN THE ACTIVE AND PASSIVE REGIONS OF A SEMICONDUCTOR LASER," Appl Phys Lett **10**(4), 130–132 (1967).

93. L. V Asryan and S. Luryi, "Effect of internal optical loss on threshold characteristics of semiconductor lasers with a quantum-confined active region," IEEE J Quantum Electron **40**(7), 833–843 (2004).

94. S. Lathi and Y. Yamamoto, "Influence of nonlinear gain and loss on the intensity noise of a multimode semiconductor laser," Phys Rev A (Coll Park) **59**(1), 819–825 (1999).

95. N. A. Pikhtin, S. O. Slipchenko, Z. N. Sokolova, and I. S. Tarasov, "Internal optical loss in semiconductor lasers," Semiconductors **38**(3), 360–367 (2004).

96. F. Toor, D. L. Sivco, H. E. Liu, and C. F. Gmachl, "Effect of waveguide sidewall roughness on the threshold current density and slope efficiency of quantum cascade lasers," Appl Phys Lett **93**(3), 31104 (2008).

97. B. S. Ryvkin and E. A. Avrutin, "Free-carrier absorption and active layer heating in large optical cavity high-power diode lasers," J Appl Phys **100**(2), 023104 (2006).

98. C.-Y. Tsai, C.-Y. Tsai, C.-H. Chen, T.-L. Sung, T.-Y. Wu, and F.-P. Shih, "Theoretical model for intravalley and intervalley free-carrier absorption in semiconductor lasers: beyond the classical Drude model," IEEE J Quantum Electron **34**(3), 552–559 (1998).

99. T. Soga, Y. Takahashi, S. Sakai, and M. Umeno, "High temperature growth rate in MOCVD growth of AlGaAs," J Cryst Growth **68**(1), 169–175 (1984).

100. M. A. Ladugin, I. v Yarotskaya, T. A. Bagaev, K. Yu. Telegin, A. Yu. Andreev, I. I. Zasavitskii, A. A. Padalitsa, and A. A. Marmalyuk, "Advanced AlGaAs/GaAs Heterostructures Grown by MOVPE," Crystals (Basel) **9**(6), (2019).

101. V. Ya. Aleshkin, N. v Baidus, A. A. Dubinov, A. G. Fefelov, Z. F. Krasilnik, K. E. Kudryavtsev, S. M. Nekorkin, A. v Novikov, D. A. Pavlov, I. v Samartsev, E. v Skorokhodov, M. v Shaleev, A. A. Sushkov, A. N. Yablonskiy, P. A. Yunin, and D. v Yurasov, "Monolithically integrated InGaAs/GaAs/AlGaAs quantum well laser grown by MOCVD on exact Ge/Si(001) substrate," Appl Phys Lett **109**(6), 61111 (2016).

102. J. Wang, H. Hu, H. Yin, Y. Bai, J. Li, X. Wei, Y. Liu, Y. Huang, X. Ren, and H. Liu, "1.3 um InAs/GaAs quantum dot lasers on silicon with GaInP upper cladding layers," Photon. Res. **6**(4), 321–325 (2018).

103. L. Wang, H. Zhao, B. Shi, S. Pinna, S. S. Brunelli, F. Sang, B. Song, and J. Klamkin, "High Performance 1.3 μm Aluminum-Free Quantum Dot Lasers Grown by MOCVD," in

Optical Fiber Communication Conference (OFC) 2020 (Optica Publishing Group, 2020), p. T4H.2.

104. J. Novák, S. Hasenöhrl, I. Vávra, and M. Kučera, "Influence of surface strain on the MOVPE growth of InGaP epitaxial layers," Applied Physics A **87**(3), 511–516 (2007).

105. M. J. Mori and E. A. Fitzgerald, "Microstructure and luminescent properties of novel InGaP alloys on relaxed GaAsP substrates," J Appl Phys **105**(1), 013107 (2009).

106. N. J. Quitoriano and E. A. Fitzgerald, "Relaxed, high-quality InP on GaAs by using InGaAs and InGaP graded buffers to avoid phase separation," J Appl Phys **102**(3), 33511 (2007).

107. C. H. Roh, Y. J. Park, K. M. Kim, Y. M. Park, E. K. Kim, and K. B. Shim, "Defect generation in multi-stacked InAs quantum dot/GaAs structures," J Cryst Growth **226**(1), 1–7 (2001).

108. K. Nishi, K. Takemasa, M. Sugawara, and Y. Arakawa, "Development of Quantum Dot Lasers for Data-Com and Silicon Photonics Applications," IEEE Journal of Selected Topics in Quantum Electronics **23**(6), (2017).

109. J. C. Norman, R. P. Mirin, and J. E. Bowers, "Quantum dot lasers—History and future prospects," Journal of Vacuum Science & Technology A **39**(2), 020802 (2021).

110. D. Liang and J. E. Bowers, "Recent progress in lasers on silicon," Nat Photonics **4**(8), 511–517 (2010).

111. Z. Fang, Q. Y. Chen, and C. Z. Zhao, "A review of recent progress in lasers on silicon," Opt Laser Technol **46**, 103–110 (2013).

112. Y. Shi, Y. Zhang, Y. Wan, Y. Yu, Y. Zhang, X. Hu, X. Xiao, H. Xu, L. Zhang, and B. Pan, "Silicon photonics for high-capacity data communications," Photonics Res **10**(9), A106–A134 (2022).

113. D. Thomson, A. Zilkie, J. E. Bowers, T. Komljenovic, G. T. Reed, L. Vivien, D. Marris-Morini, E. Cassan, L. Virot, J.-M. Fédéli, J.-M. Hartmann, J. H. Schmid, D.-X. Xu, F. Boeuf, P. O'Brien, G. Z. Mashanovich, and M. Nedeljkovic, "Roadmap on silicon photonics," Journal of Optics **18**(7), 073003 (2016).

114. Y. Liu, S. Wang, J. Wang, X. Li, M. Yu, and Y. Cai, "Silicon photonic transceivers in the field of optical communication," Nano Commun Netw **31**, 100379 (2022).

115. C. v Poulton, A. Yaacobi, D. B. Cole, M. J. Byrd, M. Raval, D. Vermeulen, and M. R. Watts, "Coherent solid-state LIDAR with silicon photonic optical phased arrays," Opt Lett **42**(20), 4091–4094 (2017).

116. T. Hu, B. Dong, X. Luo, T.-Y. Liow, J. Song, C. Lee, and G.-Q. Lo, "Silicon photonic platforms for mid-infrared applications [Invited]," Photonics Res **5**(5), 417–430 (2017).

117. S. A. Miller, Y.-C. Chang, C. T. Phare, M. C. Shin, M. Zadka, S. P. Roberts, B. Stern, X. Ji, A. Mohanty, O. A. Jimenez Gordillo, U. D. Dave, and M. Lipson, "Large-scale optical phased array using a low-power multi-pass silicon photonic platform," Optica **7**(1), 3–6 (2020).

118. H. Hashemi, "A Review of Silicon Photonics LiDAR," in *2022 IEEE Custom Integrated Circuits Conference (CICC)* (2022), pp. 1–8.

119. J. Wang and Y. Long, "On-chip silicon photonic signaling and processing: a review," Sci Bull (Beijing) **63**(19), 1267–1310 (2018).

120. A. J. Zilkie, P. Seddighian, B. J. Bijlani, W. Qian, D. C. Lee, S. Fathololoumi, J. Fong, R. Shafiiha, D. Feng, B. J. Luff, X. Zheng, J. E. Cunningham, A. v. Krishnamoorthy, and M. Asghari, "Power-efficient III-V/Silicon external cavity DBR lasers," Opt Express **20**(21), 23456 (2012).

121. R. Marchetti, C. Lacava, L. Carroll, K. Gradkowski, and P. Minzioni, "Coupling strategies for silicon photonics integrated chips [Invited]," Photonics Res **7**(2), 201 (2019).

122. B. Song, C. Stagarescu, S. Ristic, A. Behfar, and J. Klamkin, "3D integrated hybrid silicon laser," Opt Express **24**(10), 10435–10444 (2016).

123. A. Moscoso-Mártir, F. Merget, J. Mueller, J. Hauck, S. Romero-García, B. Shen, F. Lelarge, R. Brenot, A. Garreau, E. Mentovich, A. Sandomirsky, A. Badihi, D. E. Rasmussen, R. Setter, and J. Witzens, "Hybrid Silicon Photonics Flip-Chip Laser Integration with Vertical Self-Alignment," in *2017 Conference on Lasers and Electro-Optics Pacific Rim* (Optica Publishing Group, 2017), p. s2069.

124. G.-H. Duan, C. Jany, A. L. Liepvre, A. Accard, M. Lamponi, D. Make, P. Kaspar, G. Levaufre, N. Girard, F. Lelarge, J.-M. Fedeli, A. Descos, B. ben Bakir, S. Messaoudene, D. Bordel, S. Menezo, G. de Valicourt, S. Keyvaninia, G. Roelkens, D. van Thourhout, D. J. Thomson, F. Y. Gardes, and G. T. Reed, "Hybrid III--V on Silicon Lasers for Photonic Integrated Circuits on Silicon," IEEE Journal of Selected Topics in Quantum Electronics **20**(4), 158–170 (2014).

125. P. Kaur, A. Boes, G. Ren, T. G. Nguyen, G. Roelkens, and A. Mitchell, "Hybrid and heterogeneous photonic integration," APL Photonics **6**(6), 61102 (2021).

126. J. E. Bowers, "Heterogeneous Photonic Integration on Silicon," in *2018 European Conference on Optical Communication (ECOC)* (2018), pp. 1–3.

127. C. Xiang, W. Jin, D. Huang, M. A. Tran, J. Guo, Y. Wan, W. Xie, G. Kurczveil, A. M. Netherton, D. Liang, H. Rong, and J. E. Bowers, "High-Performance Silicon Photonics Using Heterogeneous Integration," IEEE Journal of Selected Topics in Quantum Electronics **28**(3: Hybrid Integration for Silicon Photonics), 1–15 (2022).

128. T. Komljenovic, D. Huang, P. Pintus, M. A. Tran, M. L. Davenport, and J. E. Bowers, "Photonic Integrated Circuits Using Heterogeneous Integration on Silicon," Proceedings of the IEEE **106**(12), 2246–2257 (2018).

129. M. A. Tran, D. Huang, and J. E. Bowers, "Tutorial on narrow linewidth tunable semiconductor lasers using Si/III-V heterogeneous integration," APL Photonics **4**(11), 111101 (2019).

130. M. L. Davenport, S. Liu, and J. E. Bowers, "Integrated heterogeneous silicon/III-V mode-locked lasers," Photonics Res **6**(5), 468–478 (2018).

131. J. C. Norman, J. E. Bowers, and A. C. Gossard, "Quantum Dot Lasers for Silicon Photonics," (2018).

132. B. Shi, L. Wang, A. A. Taylor, S. Suran Brunelli, H. Zhao, B. Song, and J. Klamkin, "MOCVD grown low dislocation density GaAs-on-V-groove patterned (001) Si for 1.3 μm quantum dot laser applications," Appl Phys Lett **114**(17), 172102 (2019).

133. D. Bimberg and U. W. Pohl, "Quantum dots: promises and accomplishments," Materials Today **14**(9), 388–397 (2011).

134. O. B. Shchekin and D. G. Deppe, "1.3 μm InAs quantum dot laser with To=161K from 0 to 80°C," Appl Phys Lett **80**(18), 3277–3279 (2002).

135. A. Y. Liu, "Quantum Dot Lasers Epitaxially Grown on Silicon," (2016).

136. J. C. Norman, D. Jung, Y. Wan, and J. E. Bowers, "Perspective: The future of quantum dot photonic integrated circuits," APL Photonics **3**(3), 030901 (2018).

137. S. Chen, W. Li, J. Wu, Q. Jiang, M. Tang, S. Shutts, S. N. Elliott, A. Sobiesierski, A. J. Seeds, I. Ross, P. M. Smowton, and H. Liu, "Electrically pumped continuous-wave III-V quantum dot lasers on silicon," Nat Photonics **10**(5), 307–311 (2016).